UNIVERSITÀ DEGLI STUDI DI PALERMO
Dottorato di Ricerca in Medicina Molecolare e Biotecnologie
Dipartimento di Fisica e Chimica
SSD FIS/07

Molecular mechanisms underlying proteins-membrane interaction

IL DOTTORE
Estella Rao

IL COORDINATORE
Prof. Calogero Caruso

IL TUTOR
Prof. Maurizio Leone

CO TUTOR
Prof.ssa Valeria Vetri

CICLO XXX
2018

Contents

Introduction

Aim of this work is to design an experimental approach, by using biophysical techniques, able to investigate in details the molecular mechanisms involved in the interaction between cellular membranes and proteins, also in dependence of their aggregation states. To this purpose, artificial membranes and the model protein alpha-lactalbumin (α-La) have been chosen. α-La is frequently used as a model in numerous studies on the biophysical properties of proteins. As an example, α-La is a simple model of Ca^{2+}-binding protein (*Hiraoka et al., 1980*) and it is also a suitable model for protein folding and molten globule studies (*Kuwajima, 1996*). It was found that α-La can induce apoptosis in tumor cells as result of physical interaction between the protein and the membrane of targeted cells *(Svensson et al., 2000*). In general, it has been suggested that α-La behavior in the interaction with membranes can be relevant to the other amphitropic proteins (*Chenal et al., 2005; Rødland et al., 2005*) that interact with cell membranes (*Burn, 1988; Johnson and Cornell, 1999*). Therefore, this system is a suitable model to highlight peculiar properties of complex and interconnected mechanisms involved in the interaction between proteins and membranes and in the amyloid related toxicity.

The thesis contains five Chapters. Chapter 1 reports a general introduction on the interaction between proteins and membranes as well as on the process of amyloid fibrillation. Moreover, a description of the model protein used, α-La, is provided, followed by a discussion on the literature related to α-La interaction with membranes and its fibrillation process.

Chapter 2 describes the experimental approach used to study both the interaction of α-La with model membranes and the α-La amyloid fibril formation process. Both spectroscopy and microscopy techniques have been used. Aim of this chapter is to give an overview of the different techniques and the achievable information. In the last part, materials, sample preparation and experimental settings are also described.

Chapter 3 reports an analysis of the interaction between α-La and giant vesicles. A study at two lipid:protein ratios is presented, showing that the destabilization of the lipid bilayer upon protein addition depends on protein concentration. The process is found to be ruled by a combination of electrostatic and hydrophobic interactions, resulting in the formation of structures made of both protein and lipids.

Chapter 4 reports experimental data on the aggregation process of α-La. The stochastic nature of the process is highlighted, indicating that α-La fibrillation is a nucleated process, taking place through a balance of primary and secondary nucleation pathways, ruled by the temperature.

Chapter 5 presents some details on the Image Mean Square Displacement (iMSD) analysis. This technique, recently developed at the Laboratory for fluorescence Dynamics (LFD, University of California, Irvine, USA) and further improved during my stage at LFD in 2016 under the supervision of Proff. Enrico Gratton and Michelle Digman, is based on Fluorescence Correlation Spectroscopy and allows monitoring molecular dynamics in live cells obtaining the diffusion laws of the proteins under investigation. In particular, the algorithms used for iMSD analysis are described and the visualization of the obtained data is presented under the form of spatial maps, providing the protein diffusion law in each region of the cell membrane.

Finally, main results are discussed in the Conclusions paragraph.

Chapter 1

State of the art

1.1 Interaction between proteins and membranes

The interaction of proteins with cellular membranes is a key topic in recent research. It is nowadays accepted that the interaction between pathogenic proteins and cell membranes, or between protein aggregates and membranes, is involved in the onset and progression of several human diseases (*Butterfield and Lashuel, 2010; Stefani, 2010; Bucciantini et al., 2014*). In particular, it was recently shown that the mechanisms underlying toxicity are related to the formation of intermediate aggregate structures, during the supramolecular association process, and their interaction with the cell membrane (*Bucciantini et al., 2014*). Such species, highly reactive, may interact with the lipid bilayer creating intra-membrane pores or change membrane fluidity inducing membrane destabilization, thinning or breakage. Amyloidogenic proteins may disintegrate membranes by extracting lipids and incorporating them into fibrils. On the other hand, membrane presence may cause variations in inter and intra-protein interactions, promoting protein destabilization and aggregation (*Hebda and Miranker, 2009; Milanesi et al., 2012*). Therefore, emphasis has been recently placed on the importance of understanding the mechanisms ruling the interaction between proteins and membranes in order to realize both the amyloid formation in vivo and toxicity (*Straub and Thirumalai, 2014*). Several studies have also shown that, in different conditions, membrane damages are induced by the aggregation of proteins both related and unrelated to amyloid diseases (*Stefani, 2004; Butterfield and Lashuel, 2010; Vetri et al., 2011*). The interaction between proteins and cell membranes is also crucial for several biological processes. Besides cytoplasmic, peripheral or integral membrane proteins,

the so-called amphitropic proteins interact with lipids and membranes during their biological activity (*Burn, 1988; Johnson and Cornell, 1999*). These proteins are found both in the water-soluble form and in association with membranes, in a membrane-bound form. The interaction between an amphitropic protein and cell membranes has several functional consequences, such as the catalytic function of the protein, the assembly of signaling complexes on the membrane as well as the attachment between membrane and cytoskeleton. Membrane association is reversible and is regulated by different factors such as membrane lipid composition or ligand binding to the protein (*Johnson and Cornell, 1999*).

1.2 Protein folding and aggregation processes

The different conformational states adopted by proteins in living system are determined by their intrinsic amino acid sequences as well as by the multiple interactions with the environment (*Dobson, 2003*). In particular conditions, such as mutations, post-transduction modifications or partial destabilization, the native state can convert into non functional and potentially damaging protein aggregates (*Dobson, 2003; Uversky and Fink, 2004*). The highly ordered and insoluble aggregates resulting from aggregation of innocuous proteins are known as amyloid fibrils. The human disorders associated with amyloid formation are due to the deposition of aggregates in multiple organs and range from Parkinson's and Alzheimer's disease (in which such aggregates are located in the brain) to type II diabetes (in which deposits form in the pancreas) (*Stefani, 2004; Uversky and Fink, 2004; Ross and Poirier, 2005; Chiti and Dobson, 2006, 2017; Merlini et al., 2011; Knowles et al., 2014; Hartl, 2017; Ke et al., 2017*). Protein aggregation related to diseases has been found to involve both intrinsically disordered proteins, such as α-synuclein (*Giehm and Otzen, 2010; Buell et al., 2014*) and Aβ-peptide (*Petkova et al., 2005; Kodali et al., 2010*), ad globular proteins, such as β_2-microglobulin (*Heegaard et al., 2005; Gosal et al., 2005*). It is accepted that the ability to form amyloid fibrils is not a characteristic of pathogenic proteins, but is an inherent property of all polypeptide chains (*Fändrich and Dobson, 2002; Dobson, 2003; Chiti and Dobson, 2006*). It is known that peptides and proteins with no connection with diseases can convert into amyloid fibrils with the same characteristics of those associated with human diseases (*Stefani, 2004*) and that even highly stable globular proteins, under destabilizing conditions, may form amyloid fibrils (*Fändrich et al., 2001; Goers et al.,*

2002). The fibrillary state represents the most stable state accessible to a protein (*Baldwin et al., 2011*). Amyloid fibrils have a high degree of organization, an elongated morphology with a diameter less than 20 nm and can reach lengths of several microns (*Fändrich et al., 2009*). They are characterized by a highly stable structure, hold together by hydrogen bonds and by a predominance of beta structures organized to form linked structures called "cross beta". The formation of amyloid fibrils is considered as an alternative path, competing with the folding process (*Dobson, 2003; Jahn and Radford, 2005; Chiti and Dobson, 2009; Eichner and Radford, 2011*). The description of protein folding in terms of energy landscape and the representation of ”funnel” folding surface can be therefore extended to a multi-protein system, which takes into account the interaction between different molecules as well as the interaction with the solvent (*Jahn and Radford, 2005; Eichner and Radford, 2011*).

Multiple pathways in aggregation processes. The complexity of protein aggregation process is related to a complex energy landscape involving multiple and competing paths. Several model for the mechanisms of amyloid formation have been proposed (*Gillam and MacPhee, 2013*). Amyloid formation mainly occurs through primary or secondary nucleation (*Ferrone, 1999*). Aggregates assemble through primary pathways, with a dependence on protein concentration (homogeneous nucleation), as well as secondary pathways, by mechanisms depending only on existing aggregates or both on protein concentration and existing aggregates (heterogeneous nucleation) (*Ferrone, 1999; Cohen et al., 2012*). In addition to nucleation-growth mechanisms including primary and secondary nucleation (*Ferrone, 1999; Librizzi and Rischel, 2005; Foderà et al., 2008, 2009; Cohen et al., 2012*), primary micelle formation (*Lomakin et al., 1997*), conformational conversion (*Serio et al., 2000*) and filament-filament association (*Pallitto and Murphy, 2001*) have been proposed as mechanisms of amyloid formation. Protein assembly through non-nucleated processes has been also observed (*Hurshman et al., 2004; Gosal et al., 2005*). The existence of different competitive pathways determines the occurrence of fibril polymorphism (*Tycko, 2015*). Moreover, depending on both protein structure and solution conditions, a competitive mechanism of amyloid fibrillation and amorphous aggregation has been pointed out (*Lee, 2009; Hall et al., 2015*) for several proteins, such as β2-microglobulin (*Yoshimura et al., 2012; Adachi et al., 2015*), lysozyme (*Hill et al., 2011*) and alpha-lactalbumin (*Stranks et al., 2009*).

1.3 Alpha-lactalbumin (α-La)

Bovine alpha-lactalbumin (α-La) is a small (14.2 kDa), acidic (isoelectric point of 4.8), Ca^{2+} binding milk protein, composed of 123 aminoacids (*Brew, 2003*). It is one of the two components of lactose synthase enzyme, which catalyzes and regulates the lactose biosynthesis in the lactating mammary gland. Its function is to enhance the binding of glucose to galactosyltransferase so that lactose synthesis is catalyzed efficiently at physiological concentrations of glucose (*Brew, 2003*).

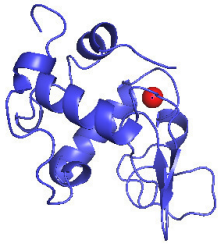

Figure 1.1 The structure of bovine α-La. The arrangement of secondary structural elements in the two subdomains of α-LA, protein databank file 1hfz (*Pike et al., 1996*), are displayed using PyMOL (The PyMOL Molecular Graphics System, Version 2.0.4 Schrödinger, LLC).

Native α-La consists of two domains, a large α-helical domain and a small β-sheet domain, connected by a calcium binding loop (Figure 1.1). The structure is typical of several α-La variants, such as human, recombinant and natural bovine, goat, guinea pig and buffalo. The α-helical domain (residues 1-34, 86-123), includes both N- and C-terminal sections of the polypeptide chain and is composed of three major α-helices (residues 5-11, 23-24, 86-98) and two short 3_{10}-helices (residues 18-20, 115-118). The small β-sheet domain (residues 35-85), formed by the central part of the sequence, is composed by a series of loops, a small three-stranded antiparallel β-pleated sheet (residues 41-44, 47-50, 55-56) and a short 3_{10}-helix (residues 77-80). The two domains are spatially divided by a deep "cleft". At the same time, the two domains are held together by a cysteine bridge between residues Cys 73 (in the β-sheet domain) and Cys 91 (in the α-helical domain), forming the Ca^{2+} binding loop, and by the disulfide bridge 61-77. Overall, native α-La structure is stabilized by four disulfide bridges:

Cys73-Cys91, Cys61-Cys77, Cys6-Cys120 and Cys28-Cys111 (*Permyakov and Berliner, 2000; Brew, 2003*).

Due to the presence of a single strong Ca^{2+} binding site (*Hiraoka et al., 1980*), α-La is often used as a simple model of protein binding Ca^{2+} ion. The binding site is located between the two domains and has been descripted as an elbow that is flanked by a 3_{10}-helix of the β-domain (residues 76-82) and a α-helix of the α-domain (residues 85-93) (*Brew, 2003*). Ca^{2+} ion is coordinated by five oxygen atoms of the α-La molecule (the oxygen of Asp_{82}, Asp_{87} and Asp_{88} carboxyl groups and of the Lys_{79} and Asp_{84} carbonyl groups) and the oxygen atoms of two water molecules. Overall, the oxygen ligands form a distorted pentagonal bipyramidal structure (*Chrysina et al., 2000; Permyakov and Berliner, 2000; Brew, 2003*). In addition, α-La has a secondary binding site for Ca^{2+} ion, several binding sites for Zn^{2+} ion, and is able to bind ions such as Mg^{2+}, Mn^{2+}, Na^{+} and K^{+}, which compete with calcium for the same binding site (*Kronman et al., 1981; Permyakov et al., 1985; Brew, 2003*).

1.3.1 α-La molten globule state

α-La has been widely used as a model in folding studies. Understanding the mechanisms of protein folding implies the knowledge of properties and detailed structures of intermediate species that populate protein folding pathways. Molten globules are partly folded forms of proteins, suggested to be general folding intermediates. A close similarity between molten globule states observed during the early stage of refolding and those observed at equilibrium under mildly denaturing conditions has been highlighted for a number of proteins, such as apomyoglobin (*Hughson et al., 1990*) and α-La (*Kuwajima, 1996*). The conformational state of α-La exposed to acid pH, the so-called A-state, is considered to be the best studied molten globule, defined as a compact denatured state retaining the native secondary structure but showing the lack of a well-defined tertiary structure (*Fink, 1995; Kuwajima, 1996*). Other α-La molten globule conformations can be generated under mildly denaturing conditions or at neutral pH and low salt concentration by removing the protein bound Ca^{2+} (*Kuwajima, 1996*). Spectroscopic analysis carried out on α-La molten globule state highlights that the A-state lacks the fixed packing interactions typical of the native state, but maintains a similar secondary structure content, being characterized by the typical compactness of the native state (*Kuwajima, 1996; Gast et al., 1998; Brew, 2003*). The thermodynamic properties of α-La molten globule

have been largely studied. Scanning calorimetric measurements performed on the acid form of α-La have shown no cooperative heat absorption peak when the heating is started from the acidic molten globule state (*Pfeil et al., 1986*). Moreover, native-like secondary structure and protein compactness have been shown to be properties typical of both molten globule and α-La thermal unfolded state. Therefore, molten globule and thermally unfolded states have been supposed to be thermodynamically indistinguishable, indicating no thermal unfolding takes place when α-La molten globule is heated (*Kuwajima, 1996*).

1.3.2 α-La in interaction with model membranes

The interaction of α-La with lipids plays an essential role in many biological processes such as the biosynthesis of lactose and the secretion of the protein in the milk *(Barbana and Pérez, 2011*). After the lactose synthesis, both lactose and α-La are secreted into milk through a process of exocytosis from the membrane of the Golgi apparatus (*Brew, 2003*). Since it is a soluble protein which interacts with membranes to achieve some of its physiological functions, α-La has been classified among amphitrophic proteins and it has been suggested that its behavior can be relevant to the other amphitropic proteins (*Chenal et al., 2005; Rødland et al., 2005*). Moreover, it has been shown that human and bovine α-La can alter their biological function and gain an anti-tumoral property if partially unfolded and bound to oleic acid (*Svensson et al., 2000, 2003*). The two complex are named HAMLET (human α-La made lethal to tumor cells) and BAMLET (bovine α-La made lethal to tumor cells). This functional state of α-La kills tumor cells by an apoptosis-like mechanism but leaves healthy cells unaffected (*Svensson et al., 2000, 2003*). After binding to the tumor cell surface, HAMLET enters the cytoplasm and accumulates in the cell nuclei, causing DNA fragmentation (*Svensson et al., 1999*). In the process, the complex interacts with mitochondria, inducing cytochrome c release, activation of caspase cascade and apoptotic cell death (*Köhler et al., 2001*). Therefore, α-La, and in particular its pH 2 molten globule state, may provide a good model for some of the properties of α-La in vivo. It may be used as a model when considering functions involving membrane transport (*Barbana and Pérez, 2011*) as well as the formation of BAMLET, which is formed via exposure of protein to lower pH at the membrane surface or in the stomach (*Svensson et al., 2000, 2003*).

α-La interaction with lipid bilayers has been widely investigated, using both small unilamellar vesicles (SUVs) and large unilamellar vesicles (LUVs) as model membranes (*Dangreau et al.,*

1982; Berliner and Koga, 1987; Bañuelos and Muga, 1995; Lala et al., 1995; Bañuelos and Muga, 1996a, 1996b; Cawthern et al., 1996; Chenal et al., 2005; Rødland et al., 2005; Barbana and Pérez, 2011). The interaction depends on the combination of hydrophobic and electrostatic interactions, which determine the properties of the membrane-bound states, ranging from native-like to molten globule conformations (*Bañuelos and Muga, 1995; Banuelos and Muga, 1996; Chenal et al., 2005*). Protein is found to have a great sensitivity to subtle changes in physicochemical conditions such as proton concentration, temperature as well as curvature and charge of the lipid membrane (*Chenal et al., 2005; Barbana and Pérez, 2011*). In particular, at pH 2, α-La rapidly inserts into the lipid membrane (*Lala et al., 1995; Cawthern et al., 1996*).

1.3.3 Aggregation process of α-La

It was shown that, under destabilizing conditions, α-La forms amyloid fibrils *(Goers et al., 2002*). Amyloid fibril formation was observed at 37°C and in presence of mechanical agitation (stirring). Several experimental conditions such as acidic pHs, high temperatures, Zn^{2+} binding to holoprotein and reduction of three disulfide bridges, were analyzed. It was shown that amyloid formation occurs at both pH 2, when α-La is in the molten globule state and, upon destabilization, by disulfide bridges reduction. It was also shown that native α-La at pH 7.4 does not fibrillate and that in presence of Zn^{2+} ions the aggregation process ends with the formation of amorphous aggregates (*Goers et al., 2002*). It was highlighted that α-La aggregation process depends on the ionic strength of the solution, on pH values and on protein concentration. In addition, protein partial denaturation and structure flexibility have been confirmed to be fundamental prerequisites for α-La fibril formation *(Goers et al., 2002; Uversky and Fink, 2004*). Recently, α-La aggregation process upon enzymatic hydrolysis has been studied with interest, due to the potential application of protein aggregates in nanotechnology field. It was shown that, upon hydrolysis by specific enzymes, the aggregation process ends with the formation of nanostructures, such as disk-shaped nanoparticles (*Balandrán-Quintana et al., 2013*) and nanotubes (*Graveland-Bikker et al., 2006a; Ipsen and Otte, 2007*). In particular, it was shown that partial hydrolysis of α-La by a protease from Bacillus licheniformis (BLP), specific for Glu-X and Asp-X bonds, leads to the formation of amyloid fibrils at low protein concentration (<20 g/L) (*Otte et al., 2005*) whereas nanotubular structures are formed at high concentration (>20 g/L) (*Graveland-Bikker et al., 2006a*). α-La nanotubes have been found

having an outer diameter of ~20 nm, an inner diameter of ~8 nm, and a length varying from hundreds of nanometers up to a few micrometers (*Graveland-Bikker et al., 2006b*). The formation of nanotube is dependent on Ca^{2+} ion concentration, as well as on the presence of other divalent or trivalent cations such as manganese, zinc and aluminium, indicating that the role of calcium in the nanotube formation is not a specific one (*Graveland-Bikker et al., 2004*). According to the proposed model, hydrolysis products form dimeric building blocks, which are self-assembled via assisted β-sheet stacking perpendicular to the longitudinal axis (*Graveland-Bikker et al., 2009)*.

Stirring effects on amyloid fibril formation. In order to induce α-La aggregation, sample has been incubated at different temperatures in presence of stirring. The characterization of the aggregation process as a function of the stirring speed allows to better investigate α-La assembly, highlighting the mechanisms at the basis of amyloid formation. The effect of shear on both protein stability and aggregation process has been largely investigated in the last decades. Due to the pulsatile nature of blood flow, intravascular fluids are continuously subjected to mechanical shear forces in the body. Moreover, shear flow is an important factor in biopharmaceutical industry during processing of protein-based therapeutics. Several studies suggest that mechanical stress resulting from agitation (shaking, stirring or vortexing), sonication or from a flow regime can affect amyloid fibril formation. Upon sample agitation, a lag phase reduction and an increase in fibrillation rate have been observed (*Serio et al., 2000; Nielsen et al., 2001; Petkova et al., 2005; Hill et al., 2006; Xue et al., 2008; Dunstan et al., 2009; Ow and Dunstan, 2013; Forsyth et al., 2016*). Shear exposure can cause a change in protein secondary structure (*Teoh et al., 2011*), and lead to the destabilization of the native state and protein unfolding (*Ashton et al., 2009*). Agitation can in general cause local fluctuations of protein concentration, enhancing the rate of mutual interactions between the molecules present in solution, i.e. monomers, oligomers, already formed fibrils, and promoting secondary nucleation mechanisms (*Serio et al., 2000; Lee et al., 2007*). In addition, aggregate fragmentation can be induced by sample agitation, providing larger available surface for heterogeneous nucleation processes (*Cohen et al., 2013*). Hence, the use of agitation to both induce and accelerate protein aggregation and amyloid fibril formation is common practice throughout the literature. A lot of studies focused on shear flow effects on amyloid fibril formation have been conducted using poorly controlled shear conditions, with heterogeneous

velocity gradients in both space and time, such that shear exposure could not be accurately specified (*Serio et al., 2000; Dunstan et al., 2009; Ow and Dunstan, 2013*). Well defined shear fields have been, instead, generated using a Couette flow cell, exposing protein solutions to uniform and well-defined shear rates for controlled periods (*Hill et al., 2006; Bekard and Dunstan, 2009; Forsyth et al., 2016*). Shear forces have been found to influence not only the fibrillation rate but also the molecular structure and final morphology of amyloid fibrils, as reported for several proteins such as insulin (*Bekard and Dunstan, 2009; Loksztejn and Dzwolak, 2010; Foderà et al., 2012;Cannon and Donald, 2013; Bäcklund et al., 2016*), Aβ-peptide (*Petkova et al., 2005; Kodali et al., 2010*), and β_2-Microglobulin (*Gosal et al., 2005*). Differences in fibrils morphologies increase under quiescent compared to agitated conditions, as observed for amyloid-β fibrils. Fibrils grown under quiescent conditions tend to have a twisted structure, while aggregates grown under agitated conditions appear to be composed of laterally associated filaments and lack discernable twist (*Petkova et al., 2005; Kodali et al., 2010*). Analogously, insulin fibrillation under quiescent conditions ends with the formation amyloid spherulites (*Foderà et al., 2012; Cannon and Donald, 2013*), while agitation promotes the formation of laterally associated fibrils (*Bekard and Dunstan, 2009*).

Chapter 2

Experimental Methods

Aim of this chapter is to describe the experimental approach used to investigate the mechanisms at the basis of the interaction between proteins and membrane. Artificial membranes and molten globule alpha-lactalbumin (α-La) have been used as model system, and the aggregation process of molten globule α-La has been also characterized. The system has been analyzed by means of spectroscopy methods and advanced microscopy techniques. Moreover, the principles at the basis of the Image Mean Square Displacement (iMSD) analysis are described. The technique has been recently developed at the Laboratory for Fluorescence Dynamics (LFD, University of California, Irvine, USA), and allows investigating molecular dynamics in live cells, obtaining the diffusion laws of the proteins under investigation directly from imaging, in the form of an iMSD vs time plot. In the final section of the chapter, an overview of materials, samples preparation and treatments procedure is also provided.

2.1 Lipid model membranes

Biological membranes are complicated systems to work with, due to their complex composition and their huge diversity. In order to understand the mechanisms underlying protein lipid interaction as well as other processes taking place in natural membranes, model systems mimicking the actual membranes have been developed, to simplify their complexity and allow their study. Among the different model systems that retain the essential lipid bilayer structure, liposomes or artificial vesicles are characterized by a spherical shape and can be created by natural phospholipids. Liposome properties, such as surface charge or membrane fluidity, are dependent on the choice of the components of the bilayer. In this work, giant vesicles (GVs)

made of a mixture of 2-Oleoyl-1-palmitoyl-sn-glycero-3-phosphocholine (POPC) and 2-Oleoyl-1-palmitoyl-sn-glycero-3-phospho-rac-(1-glycerol) sodium salt (POPG), in the ratio 2:1, have been used as model membranes.

2.2 Experimental techniques

In order to investigate the interaction between α-La and giant vesicles as well as α-La aggregation process, an experimental approach made of spectroscopy and microscopy techniques has been used. Confocal fluorescence microscopy has been used to characterize structures resulting from the interaction between α-La and vesicles. Protein local environment has been investigated by means of Fluorescence Lifetime Image Microscopy (FLIM) measurements performed on Atto 647 labeled α-La, in order to analyze the differences in final structures. Changes in protein secondary and tertiary structure upon interaction with lipid bilayers have been examined by means of Circular Dichroism (CD) spectroscopy and intrinsic fluorescence measurements, respectively. Laurdan dye and 2-photon microscopy have been used to investigate variations in phospholipid phase state. Raster Image Correlation Spectroscopy (RICS) analysis of fluorescence confocal images has been also performed. The supramolecular assembly of α-La has been investigated by means of Rayleigh scattering and *in situ* Thioflavin T (ThT) fluorescence measurements, both acquired as function of time, performing FTIR absorption spectroscopy and confocal fluorescence microscopy measurements to characterize the structure and morphology of the supramolecular structures.

2.2.1 Spectroscopy techniques

Fluorescence and Rayleigh Scattering measurements

In this work, fluorescence spectroscopy measurements have been performed to investigate both the interaction between α-La and model membranes and the aggregation process of α-La. Since fluorescence signal are extremely sensitive to the microenvironment of the fluorophores, the technique is useful to investigate sample properties. Intrinsic fluorescence measurements allow analyzing protein conformational changes occurring upon interaction with vesicles or during supramolecular assembly. Extrinsic dyes, such as Laurdan and Thioflavin T (ThT), have been

used to analyze variations in membrane fluidity occurring after α-La addition as well as the nature of the supramolecular structures formed during α-La aggregation. In this work, Rayleigh scattering intensity and ThT fluorescence emission have been simultaneously acquired, as a function of time, to monitor protein aggregation. If ThT dye is specific for amyloid structures, Rayleigh scattering gives qualitative information about the average size of aggregates in solution, independently of the nature of supramolecular aggregates. The simultaneous acquisition of both ThT fluorescence emission and Rayleigh scattering intensity is useful to highlight the presence of different interconnected aggregation pathways.

Intrinsic Fluorescence. Intrinsic protein fluorescence originates from the aromatic amino acids that are naturally present in proteins and represents a useful tool to detect protein conformation and investigate the changes in protein structures occurring during several processes such as protein unfolding, aggregation and interaction with membranes. The intrinsic fluorescence of proteins is mainly due to tryptophan (Trp) and tyrosine (Tyr) residues. Their fluorescence properties are highly sensitive to the local environment, providing a method to identify the different protein conformations. In particular, Trp has the highest quantum yield and its emission maximum is sensitive to the polarity of its environment (*Lakowicz, 2006; Munishkina and Fink, 2007*). Therefore, protein emission maximum reflects the average exposure of the Trp residues to the aqueous solvent and gives information on the structural changes occurring during the investigated process. Upon protein folding, Trp residue is often buried in the protein hydrophobic cores, with a low exposure to aqueous solvent. As the protein undergoes conformational changes from the native state to an unfolded one, Trp emission spectrum shows a red shift that indicates an increased solvent exposure. Therefore, Trp is a commonly used intrinsic fluorescent probe in studying protein folding and dynamics. Changes in Trp emission spectrum have been observed for different proteins, upon protein aggregation and amyloid formation (*Souillac et al., 2003; Heegaard et al., 2005; Pedersen et al., 2006; Vetri et al., 2007a, 2013*).

Laurdan fluorescence emission. One of the most popular polarity-sensitive dyes for the investigation of membrane organization is Laurdan (6-lauryl-2-dimethylamino-naphthalene), which is a derivative of Prodan created by Weber and Farris in 1979 (*Weber and Farris, 1979*).

Laurdan is a fluorescent dye that detects changes in membrane phase properties through its sensitivity to the polarity of its environment in the bilayer. The dye, due to its spectral properties, allows determining the phospholipid phase state. As shown in Figure 2.1, Laurdan spectrum emission, within a single phospholipid bilayer, is centered at 490 nm when the lipids are in a disordered phase (liquid crystalline phase) (Figure 2.1A) and is shifted to the blue, around 440 nm, when the lipids are in a more packed phase (gel phase) (Figure 2.1B) (*Parasassi et al., 1998; Sanchez et al., 2007*).

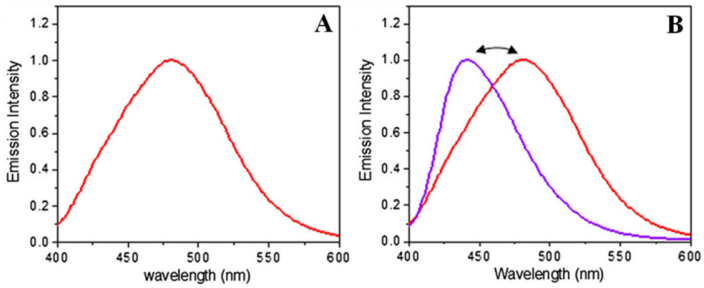

Figure 2.1 Laurdan emission spectrum in DPPC small unilamellar vesicles ($T_{melting}$ equals 41°C) **(A)** Emission spectrum of Laurdan at 50°C (DPPC in liquid crystalline phase). **(B)** Emission spectra of Laurdan at 50°C (DPPC in liquid crystalline phase, red line) and at 35°C (DPPC in gel phase, blue line). Spectra are obtained using excitation light at 340 nm. Figure adapted from Sanchez et al., 2012 (*Sanchez et al., 2012*).

Variations in membrane water content, related to lipid packing and membrane fluidity, are detected by shifts in the Laurdan emission spectrum, and the Laurdan Generalized Polarization (GP) was defined as a way of measuring wavelength displacements (*Parasassi et al., 1990*). According to Parasassi et al. (*Parasassi et al., 1990*), the Laurdan GP function is:

$$GP = \frac{(I_{440} - I_{490})}{(I_{440} + I_{490})}$$

where I_{440} and I_{490} are the emission intensities at 440 nm and 490 nm respectively. Changes in GP value usually account for variations in membrane organization due to modifications in dipolar relaxation of Laurdan in lipid environment. Laurdan dye has been largely used in several studies on model membranes to monitor phase transitions and other alterations in membrane

fluidity. It has been used to stain artificial membranes, live and fixed cells, as well as whole organisms (*Owen et al., 2010*), without any adverse effects on the membranes under investigation (*Owen et al., 2012*)

Thioflavin T. Thioflavin T is one of the most widely used tools both in vivo and in vitro for selective staining and identifying amyloid formation, distinguishing between amyloid structures and amorphous aggregates (*Naiki et al., 1989; LeVine III, 1999; Biancalana and Koide, 2010*). The dye is characterized by an absorption spectrum in the range 330 – 470 nm, which in aqueous solvent is centered at ~412 nm. The position and the intensity of the absorption peak depend on the solvent in which the dye is dissolved. (*Voropai et al., 2003*). ThT has a weak fluorescence emission band in absence of amyloid aggregates as well as in aqueous solution (*Maskevich et al., 2007; Stsiapura et al., 2008*). Upon binding to amyloid fibrils, ThT gives a strong fluorescence signal in the range 475 - 600 nm, with a maximum at ~480 nm, being its fluorescence emission dependent on the concentration of amyloid structures in the sample (*Naiki et al., 1989; LeVine III, 1993*). ThT fluorescence enhancement upon binding to amyloid fibrils has been largely studied. It has been suggested that ThT behaves as a molecular rotor (*Voropai et al., 2003; Stsiapura et al., 2008*). The structure of ThT dye is showed in Figure 2.2. The spectroscopic properties of the dye are determined by the planes of the benzylamine and benzathiole rings and by their mutual rotation (*Maskevich et al., 2007*).

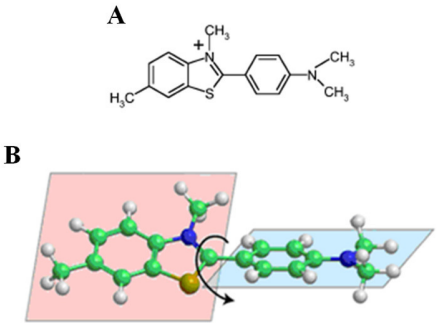

Figure 2.2 (A) Structure of fluorescent dye ThT. **(B)** The two ThT planes whose mutual rotation defines the spectroscopic properties of the dye.

When the dye is free in solution, the benzylamine and benzathiole rings are free to rotate about the central C-C bond, quenching the excited states and causing the low fluorescence emission. In contrast, when the dye is located in viscous solvents or in a rigid microenvironment, the rotational immobilization preserves the excited states, resulting in an high quantum yield of fluorescence (*Voropai et al., 2003; Stsiapura et al., 2008*). Therefore, upon binding to amyloid fibrils β-sheet structures, ThT stabilizes the planar form and shows the increased fluorescence signal. Fluorescence enhancement is related to an increase of β-sheet structures occurring during amyloid fibril assembly and growth (*Krebs et al., 2005; Munishkina and Fink, 2007; Stsiapura et al., 2008*). The structural basis for binding specificity and for the photophysical properties of ThT have been largely studied. Several binding modes of ThT to amyloid fibrils have been proposed, thus being a controversial topic. It has been suggested that the dye can bind to fibrils in its micelle form (*Khurana et al., 2005*) and that the formation of a ThT dymer in the cavity structures of fibrils is a plausible mechanism for the occurrence of the characteristic fluorescence enhancement (*Groenning et al., 2007*). It has been also proposed that the dye binds to fibrils with its long axis parallel to that of the fibrils, inserting into the "channels" formed by the side chain residues in the amyloid cross-β structure (*Krebs et al., 2005*). However, all the divergent binding mechanisms are compatible with the existence of ThT binding regions at the amyloid fibril surface.

Circular Dichroism

Circular Dichroism (CD) spectroscopy refers to the differential absorption of left- and right-handed circularly polarized radiation by chromophores that possess intrinsic chirality or are placed in chiral environments. CD spectroscopy is a valuable technique for examining the structure of proteins in solution and monitoring protein conformational changes resulting from changes in experimental parameters such us pH, temperature and binding of ligands (*Kelly and Price, 2000; Kelly et al., 2005*). In addition, the technique is useful to investigate protein structural changes following both supramolecular assembly and interaction with lipids in membranes. Measuring the dichroism as a function of wavelength, the CD spectrum is obtained. In proteins, the peptide bond is the principal absorbing group in the far-UV region (typically 240 nm to 190 nm) while CD signal in the near-UV region (260 nm to 320 nm) is mainly due to aromatic amino acid side chains (phenylalanine, tyrosine and tryptophan). From CD

measurements in the far-UV region, therefore, protein secondary structure composition can be inferred, because of the characteristic CD spectrum corresponding to the different types of regular secondary structure found in proteins. Measurements in the near-UV region are useful to obtain information on protein tertiary structure, being CD signal depending on the environment of the aromatic residues and on tertiary folding of protein (*Kelly and Price, 2000; Kelly et al., 2005*).

FTIR absorption measurements

FTIR spectroscopy has been used to investigate the secondary structure of α-La aggregates obtained at different experimental conditions. FTIR spectrum of a protein is due to both backbone vibrational modes and side chain vibrations. Amide I and Amide II are the most commonly used for determining the secondary and tertiary structure of proteins (*Barth, 2007*). Amide I (~ 1650 cm^{-1} in H_2O, ~ 1650 cm^{-1} in D_2O) arises mainly from the CO stretching and the CN stretching vibrations of the peptide group, while Amide II (~ 1550 cm^{-1} in H_2O, ~ 1550 cm^{-1} to ~ 1450 cm^{-1} in D_2O) is the out-of-phase combination of the NH in plane bending and the CN stretching vibrations. In particular, Amide I band is largely used to investigate protein secondary structure, because of the different absorption peaks arising from different structures. Assignment of Amide I band position to secondary structure are known (*Pelton and McLean, 2000; Barth, 2007*). A deconvolution of Amide I band, therefore, gives indication on protein α-helix, β-sheet and random coil contents (*Pelton and McLean, 2000; Piccirilli et al., 2015*), and allows evaluating changes in protein structure induced by aggregation at different experimental conditions.

2.2.2 Microscopy techniques

Two-photon and Confocal fluorescence microscopy

Fluorescence microscopy has nowadays a central role in several fields, such as biology and biophysics. It allows investigating the sample in a selective way, exploiting the large variety of fluorescent dyes that specifically bind to different regions of the sample and have fluorescence emissions in different spectral regions. The sample can be excited by means of radiation in both the visible and the infrared region of the electromagnetic spectrum, resulting in one photon and

two photon excitation, respectively. Confocal fluorescence microscopy provides high-resolution images of thick samples, which are optically sliced. The sample is scanned by a laser beam and fluorescence emission is collected rejecting out-of-focus contributions by means of a pinhole. Two-photon excitation provides optical sectioning for three-dimensional imaging, but in contrast to confocal microscopy there is no absorption and fluorescence above and below the plane of focus. Therefore, two-photon microscopy results in reduced photobleaching and photodamage of samples. Fluorescence microscopy allows to investigate different properties of the sample, such as fluorescence intensity and lifetime.

Total Internal Reflection Fluorescence (TIRF) microscopy

Total Internal Reflection Fluorescence (TIRF) microscopy is an excellent tool to investigate key events occurring at the cell membrane. It is a powerful technique for selectively imaging fluorescent molecules, in aqueous or cellular environment, that are very near a solid surface (within ≤ 100 nm), without exiting regions farther from the surface (*Axelrod, 1981*). Fluorescent molecules in the thin region of the sample are excited by an evanescent wave, produced by an excitation light beam incident at a high angle ϑ upon the solid/liquid interface at which the sample adhere (e.g. glass coverslip/aqueous sample). The concept of evanescent wave is illustrated in Figure 2.3. The incident beam is totally internally reflected when the angle ϑ is above the "critical angle" ϑ_c, otherwise the beam will be refracted trough the interface (Figure 2.3A). The evanescent field has the same frequency as the incident light and exponentially decays in intensity with increasing distance normal to the surface (Figure 2.3B).

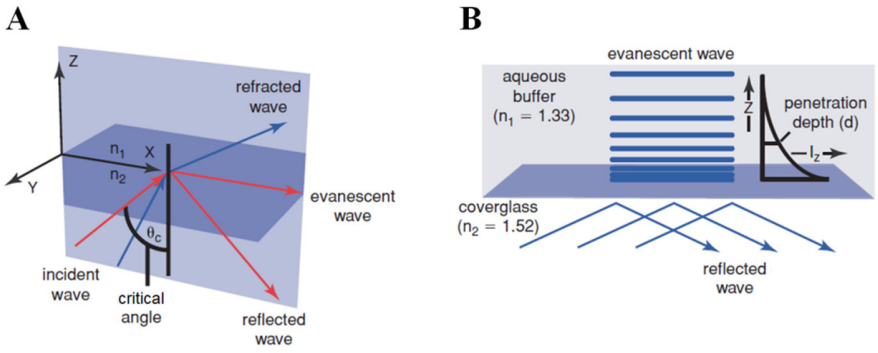

Figure 2.3 The evanescent wave. **(A)** The evanescent wave is produced by an excitation light beam incident at a high angle upon the solid/liquid interface at which the sample adhere (e.g. glass coverslip/aqueous sample). When the angle ϑ is above the "critical angle ϑ_c", the incident beam is totally internally reflected; if the angle ϑ is less than ϑ_c the beam will be refracted trough the interface. **(B)** The intensity of evanescent field decays exponentially with increasing distance from the interface. The penetration depth decreases as the reflection angle grows and depends on both the refractive index at the interface and the illumination wavelength. Figure is adapted from Fish (*Fish, 2009*).

The difference between the refractive indices n_2 and n_1 regulates how light is refracted or reflected at the interface as a function of incident light. The critical angle ϑ_c is given by:

$$\vartheta_{critical} = sin^{-1}(n_1/n_2)$$

Where n_1 and n_2 are the refractive indices of the liquid and the solid, respectively. The ratio n_1/n_2 must be less than unity for total internal reflection to occur. For incidence angle lower than ϑ_c most of the light is refracted with a refraction angle given by Snell's law. For angles above the critical one, all the light is reflected back into the solid. The reflection generates an electromagnetic field (the evanescent field) that propagates parallel to the surface with an intensity I that decays exponentially with perpendicular distance z from the surface (Figure 2.3):

$$I_z = I_0 e^{-z/d}$$

The depth d is given by:

$$d = \frac{\lambda_0}{4\pi}(n_2{}^2 sin^2\vartheta - n_1{}^2)^{-1/2}$$

Where λ_0 is the wavelength of incident light in vacuum, ϑ is the angle of incidence, n_1 and n_2 the refractive indices of the liquid and the solid, respectively. The excitation of a thin region of the sample results in the minimal exposure of cells to light, virtual absence of out of focus collected fluorescence and images with very low background signal (*Axelrod, 2001*).

Fluorescence Lifetime Imaging Microscopy (FLIM)

Fluorescence is not only characterized by the fluorescence spectrum and the spatial distribution of fluorescence intensity. A deeper characterization of the sample can be obtained by analyzing the fluorescence decay function. The fluorescence lifetime of a fluorophore is defined as the average time that the fluorophore spends in its excitation state before returning to the ground state (*Lakowicz, 2006*). It is sensitive to the fluorophore's microenvironment, including factors such as temperature, solution pH, polarity, ion concentration and fluorescence quenching and is independent on concentration. For a homogenous population of fluorophores, the resulting fluorescence decay is a single exponential function. Multiple lifetime components arise from different molecular species or different conformations of the same molecule. Different lifetimes also account for different interactions between the fluorophore and its environment. Therefore, the fluorescence lifetime is a molecular property that gives a clearer fluorophore signature than intensity spectra and contains information on the local molecular environment of the fluorescent molecule. By means of Fluorescence lifetime imaging microscopy (FLIM) it is possible to obtain spatially resolved images of fluorophore lifetime and to investigate its local environment, interpreting the changes in lifetime values in terms of variations in molecular interactions between the fluorophore and its microenvironment. A method for analyzing FLIM data has been recently introduced by Digman et al. (*Digman et al., 2008*). The Phasor approach allows performing FLIM data analysis in the phasor space, avoiding the exponential fitting of fluorescence decay. According to the phasor approach, each fluorescence decay component or molecular species is identified by a unique vector in the "phasor plot". The vector is called phasor and has a unique location in the phasor plot, independently of the number of exponentials needed to describe the fluorescence decay.

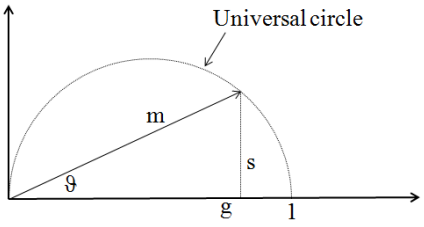

Figure 2.4 Phasor plot. The Universal circle and a phasor are represented. The phasor is identified by the module "m" and the phase "ϑ". The x-coordinate and y-coordinate of the phasor are g and s, respectively.

The phasor plot is represented in Figure 2.4. Each phasor is described by a module m and a phase ϑ, and has coordinates g=m·cos(ϑ) and s=m·sin(ϑ). When fluorescence lifetime data are acquired in the time domain, the equations that transform the intensity decay I(t) in the coordinates g and s are (*Digman et al., 2008; Stringari et al., 2011*):

$$g_{i,j}(\omega) = \frac{\int_0^\infty I_{i,j}(t)\cos(\omega t)\,dt}{\int_0^\infty I_{i,j}(t)}$$

$$s_{i,j}(\omega) = \frac{\int_0^\infty I_{i,j}(t)\sin(\omega t)\,dt}{\int_0^\infty I_{i,j}(t)}$$

where the indices i and j identify a pixel of the image and ω the frequency. All monoexponential decays lie on the "universal circle", defined as the semicircle of radius ½, going from the point (0,0), corresponding to a lifetime τ = ∞, to the point (1,0), corresponding to a lifetime τ = 0. The combinations of two single exponential components lie inside the semicircle, being along the line joining the phasors of the two monoexponential states (*Digman et al., 2008; Stringari et al., 2011*). Since its introduction, the phasor analysis has been widely used both with extrinsic and intrinsic fluorophores (*Stringari et al., 2011, 2012; Battisti et al., 2012; Golfetto et al., 2013; Plotegher et al., 2015; Ma et al., 2016; Sameni et al., 2016*). The phasor analysis of label-free FLIM images allowed the interpretation of intrinsic fluorescence signal arising from living tissues, assigning a phasor fingerprint to several physiological relevant fluorophores and avoiding the multiexponential fitting of fluorescence intensity decays coming from multiple

fluorescent species present in the focal volume (*Stringari et al., 2011*). Moreover, the phasor analysis of Laurdan lifetime has been proposed as a new method for the analysis of Laurdan fluorescence in biological membranes in order to investigate membrane heterogeneity (*Golfetto et al., 2013*).

Raster Image Correlation Spectroscopy (RICS)

Raster image correlation spectroscopy (RICS) is a non invasive technique for measuring the diffusion coefficient and the concentration of labeled proteins from fluorescence confocal images (*Digman et al., 2005a, 2005b*). The technique allows measuring dynamic processes such as molecular diffusion in the microseconds to milliseconds timescale, distinguishing between quickly moving and slower proteins. RICS approach is based on the idea that the movement of molecules causes fluctuations in the fluorescence intensity at a given pixel in the image. Images are acquired using a "raster" scan: the top left pixel is measured first and then the top row is collected from left to right; thereafter, the laser travels back to the left of the image without collecting any pixels and begins a second row. Rows are collected in this manner from top to bottom until an entire image is obtained. Because each pixel is collected at a different time, each image has an hidden time structure that can be used to extract temporal information (*Digman et al., 2005a, 2005b*). The mathematical approach to RICS analysis has been described in several papers (*Digman et al., 2005a, 2005b; Brown et al., 2008; Digman and Gratton, 2009*). RICS analysis consists of calculating the 2D autocorrelation function:

$$G_{RICS}(\xi,\psi) = \frac{< I(x,y)I(x+\xi,y+\psi) >}{< I(x,y) >< I(x,y) >} - 1$$

where I(x,y) is a matrix representing one image of the stack, ξ and ψ are increments in the x and y direction, respectively, and the brackets <…> are the spatial average of the image. Figure 2.5 shows the schematic representation of the shifting operation used in the 2D correlation function calculation and the representative images of simulated point sources moving in solution, with two different diffusion coefficient (*Brown et al., 2008*). In Figure 2.5F and 2.5G, the vertical and horizontal components of autocorrelation function are also showed. Both the image and the autocorrelation function clearly depend on the scan time compared to the point sources diffusion

coefficient. When the point sources are moving rapidly compared to the line scan time, the spatial autocorrelation function appears elongated along the horizontal axis with little height along the vertical axis (Figure 2.5D). As the diffusion rate decreases, the spatial autocorrelation function broadens along the vertical axes because of a higher probability of finding the point source in the same or similar pixel location after the line scan time (Figure 2.5E). This is evident from Figure 2.5F and 2.5G, showing respectively the horizontal and vertical component of the autocorrelation function for different diffusion coefficients.

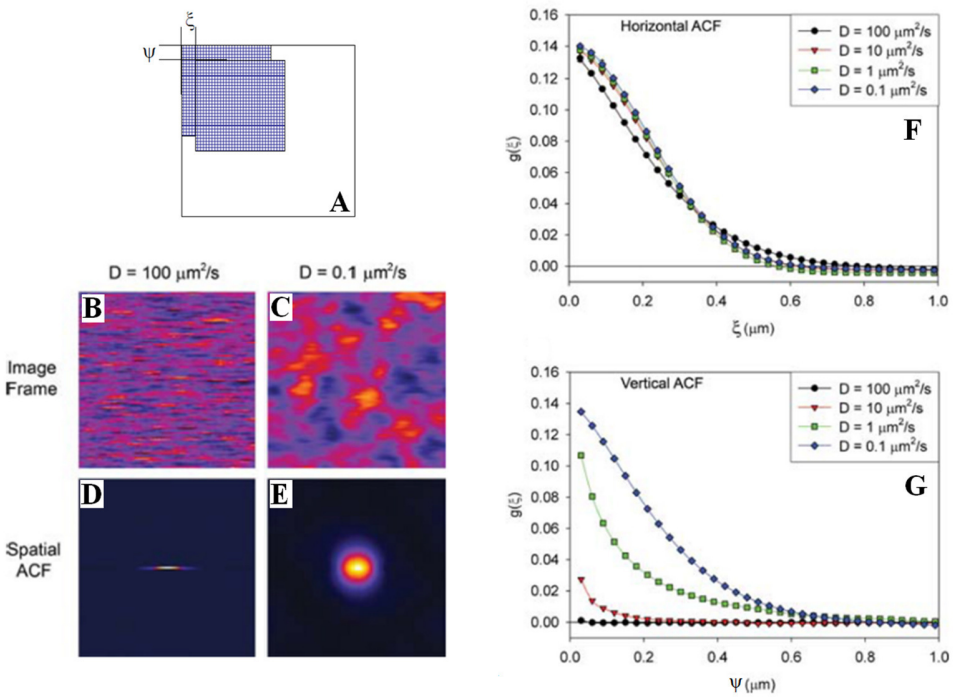

Figure 2.5 (A) Schematic representation of the shifting operation used in the 2D autocorrelation function calculation. **(B, C)** Images and **(D, E)** spatial ACFs from simulations of point sources diffusing in solution with D=100 and D=0.1μm^2/s. The imaging conditions are 8 μs pixel dwell time, 7 ms between lines, 0.86 s between frames. Spatial ACF have been calculated from 300 image frames. **(F)** Horizontal and **(G)** vertical components of the autocorrelation function for simulations of point source diffusion with variable diffusion coefficients. **(A)** is adapted from Digman and Gratton, 2009 (*Digman and Gratton, 2009*). **(B-G)** are adapted from Brown et al., 2008 (*Brown et al., 2008*).

RICS analysis requires a stack of several images (50 to 100) acquired in rapid succession. The technique can be used to measure diffusion dynamics of molecules both in solution and inside live cells, and spatial fluctuation can be analyzed to recover the diffusion coefficient and the

number of molecules in the excitation volume. Moreover, the spatial correlations due to immobile or slowly moving structures within the image can be removed by averaging all of the images of the stack and subtracting the average image from each frame (*Digman et al., 2005a, 2005b*).

Image Mean Square Displacement (iMSD)

The purpose of the iMSD analysis is to determine the diffusion law in heterogeneous media. The analysis is based on the measurement of the variance of a Gaussian describing the broadening of the spatial probability of finding a molecule in a given volume if it was at the center of the volume at time zero (*Di Rienzo et al., 2013*). As the molecules diffuse, they can be found at a distance from the origin that depends on the square of time, if the motion is pure Brownian diffusion. This is called the Mean Square Displacement (MSD) which is a graph of the square of the displacement of a molecule as a function of time (*Michalet, 2010*). The slope of this graph is proportional to the diffusion coefficient. The MSD parameter is commonly obtained in real space using single particle tracking methods one particle at a time (*Michalet, 2010*). In heterogeneous media, the distance from the center could be limited by several factors, such as the nature of the medium, barriers to diffusion, cavities and molecular interactions with fixed or mobile structures. Similar information can be obtained using spatial correlation functions in the correlation space rather than in the real space, without the need to track individual particles (*Hebert et al., 2005*). Using image correlation methods, the spatiotemporal correlation function can be calculated, and it shows a broadening as a function of time that can be related to a model of diffusion. Since this broadening is obtained using image correlation methods, the parameter obtained by image correlation is called iMSD (image Mean Square Displacement). The broadening can in principle be different in different directions giving rise to diffusion anisotropy (*Di Rienzo et al., 2016*). The intent of the iMSD analysis is to capture the heterogeneous broadening of the correlation function in different parts of the sample and at different times. The algorithm for the calculation of the iMSD is based on the STICS correlation function (*Hebert et al., 2005*)

$$G(\xi,\chi,\tau) = \frac{< I(x,y,t) \cdot I(x+\xi, y+\chi, t+\tau) >}{< I(x,y,t) >^2}$$

where the brackets indicate average over the *x,y* coordinates and time *t*. ξ and χ are the shift of the *x* and *y* coordinates and *τ* is the time delay. *I(x,y,t)* represents one image of an image stack of the same field of view acquired as a function of time. The equation is valid for any type of images, in particular for fluorescence intensity images. Assuming that the shape of the illumination volume is Gaussian and that the diffusion process can be expressed by the Fick's second law, the resulting correlation function after the integration on the *x*, *y* and *t* coordinates is given by (*Di Rienzo et al., 2013*)

$$G(\xi,\chi,\tau) = g(\tau)\cdot exp\left(-\frac{\xi^2+\chi^2}{{\sigma_r}^2(\tau)}\right) + g_\infty(\tau)$$

The terms $g(\tau)$ and ${\sigma_r}^2(\tau)$ represent respectively the amplitude and the width of the Gaussian correlation function, as a function of time delay. The variance of the Gaussian is assumed to be composed of 3 terms

$$\sigma^2(\tau) = {\sigma_0}^2 + 4D_{macro}\tau + \frac{L^2}{3}(1 - e^{-k_{micro}\tau})$$

The first term, σ_0^2**,** represents the Gaussian variance at time zero, the second term represents the macroscopic diffusion and the third term represents the confined diffusion within a region of average length *L*. k_{micro} is the rate to achieve confinement and it has dimensions of inverse time (s^{-1}).

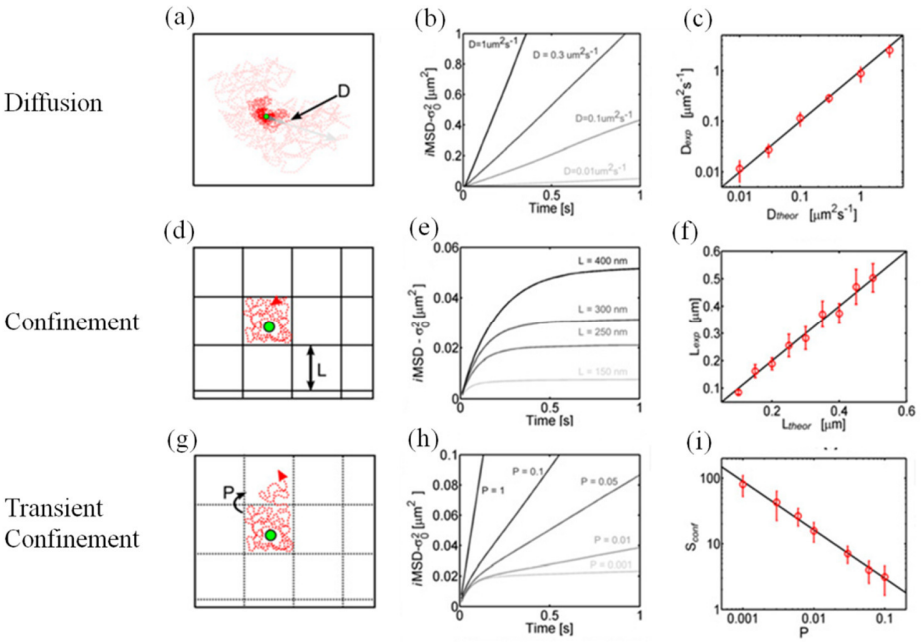

Figure 2.6 iMSD analysis on simulated 2D diffusion. **(a, b, c)** Simulated condition: 2D isotropic diffusion, with diffusivity D. **(b)** iMSD is linear, with a higher slope for increasing D values. **(c)** Accordance between the theoretical D value and that recovered from the analysis. **(d, e, f)** Simulated condition: 2D isotropic diffusion in a meshwork of impenetrable barriers (probability P = 0 to overcome the barrier). **(e)** iMSD plot starts linear and then reaches a plateau that identifies the confinement area and the corresponding linear size L. **(f)** Accordance between the theoretical L value and that recovered from the analysis. **(g, h, i)** Simulated condition: 2D isotropic diffusion in a meshwork of penetrable barriers. Particles have probability P > 0 to overcome the barrier, thus generating a hop diffusion component. **(h)** iMSD plot starts linear (with a slope dependent on D_{micro}) and then deviates toward a lower slope which depends on P. **(i)** Calculated S_{conf} as a function of the imposed P. Figure adapted from Di Rienzo et al. (*Di Rienzo et al., 2013*).

The behavior of $\sigma^2(\tau)$ is illustrated in Figure 2.6, where 3 common diffusion laws are considered (*Di Rienzo et al., 2013*). In the case of pure diffusion, the value of L is zero and the variance changes linearly with the delay time τ. In the case of pure confinement, the rate to reach confinement is described by the k_{micro} term and the average size of the confinement is given by L. The initial slope to reach confinement is given by the following expression

$$D_{micro} = \frac{L^2}{12} * k_{micro}$$

which has the dimension of a diffusion coefficient (μm²/s) and it is generally also called D_{micro}.

The iMSD method works with images acquired with a camera. However, several of the new confocal microscopes can acquire images at a speed comparable with EMCCD cameras in relatively small frames. If the image is acquired very fast in the confocal mode, it could appear as an image acquired with a camera. However, the interpretation of the intercept parameter σ_0^2 must be re-evaluated. Large frame sCMOS cameras could be used although the noise of these cameras must be accounted for using de-noising procedures.

2.3 Materials, sample preparation and experimental settings

2.3.1 α-La in interaction with Giant Vesicles

2-Oleoyl-1-palmitoyl-sn-glycero-3-phosphocholine (POPC), 2-Oleoyl-1-palmitoyl-sn-glycero-3-phospho-rac-(1-glycerol) sodium salt (POPG), 6-Dodecanoyl-2-dimethylaminonaphthalene (Laurdan) and Atto 647 NHS ester were purchased from Sigma Aldrich. Bovine α-lactalbumin (α-La, batch number JE 010-5-410) was kindly provided by Davisco Foods International (USA) and was used without further purification.

Giant vesicles preparation and staining. Phospholipid giant vesicles (GVs) were prepared mixing POPC and POPG (POPC:POPG 2:1) in chloroform:methanol 3:2. Using a rotary evaporator (Buchi, Rotavapor R-215, equipped with the Buchi Vacuum controller V-855), the lipids were dried to form lipid films. After drying overnight, the lipids were hydrated with NaCl 0.1 M, pH 2. POPG: POPC GV are known to be globally negatively charged at neutral pH. At acid pH and in particular at pH 2, based on the different protonation of the head groups (*Cevc, 1990*), it is possible to infer that they are characterized by an heterogeneous charge distribution due to the opposite contribution of POPC and POPG both slightly charged. GVs were diluted to a final lipid concentration of 0.2 mM and used within 24 hours. A final lipid concentration of 0.4 mM was used in circular dichroism measurements.
A stock solution of Laurdan (0.5 mM) was prepared in DMSO and stored protected from light exposure. Laurdan was added to the GVs in a probe-lipid molar ratio of 1:500 and left to equilibrate for 3 hours before doing measurements.

α-La sample preparation and labeling procedure. Bovine α-La was dissolved in NaCl 0.1 M, pH 2. Samples were freshly prepared and filtered through 0.10 μm filters (16553, Sartorius). Protein concentration was determined by means of a Jasco V-760 UV-Vis spectrophotometer, using an extinction coefficient $\varepsilon^{1\%}$=20 at λ=280 nm (Brew, 2003). To label α-La with Atto 647 NHS ester dye, protein was dissolved in 0.1 M potassium phosphate buffer (pH 8.3) and a stock solution of Atto 647 NHS ester in DMSO (2 mg/ml) was prepared. Aliquots of dye solution were added to protein solution in a dye:protein ratio of 3:1. After two hours of incubation at room temperature, the labeled protein was separated from unreacted dye using a Sephadex G-25 column, equilibrated with phosphate buffer pH 7.4. Labeled-α-La was added to α-La sample at molar ratio 1:100. α-La was added to GVs at lipid:protein molar ratios (L/P) 250:1 and 20:1. Final α-La concentrations were 10 μM (L/P 20:1) and 0.8 μM (L/P 250:1). A final protein concentration of 1.6 μM was used in circular dichroism measurements, at L/P 250:1.

Fluorescence measurements. Fluorescence measurements were carried out at 25°C in 1 cm path quartz cuvettes using a Jasco FP-8500 spectrophotometer equipped with a Jasco ETC-815 peltier as temperature controller. At L/P 20:1 protein and lipid concentration were 10 μM and 200 μM, respectively. At L/P 250:1 protein and lipid concentration were 0.8 μM and 200 μM, respectively.

Tryptophans fluorescence emission. Intrinsic fluorescence emission spectra were acquired using an excitation wavelength λ_{exc} =290 nm and detected in the range 285-500 nm, with 0.5 nm wavelength interval and emission and excitation bandwidth of 2.5 nm and 5 nm, respectively.

Laurdan fluorescence emission. Laurdan emission spectra were acquired in the range 360 – 600 nm, using an excitation wavelength λ_{exc} = 350 nm. Spectra were recorded with 0.5 nm wavelength interval, emission and excitation bandwidth of 5 nm and 10 nm, respectively. The Laurdan Generalized Polarization (GP) function was calculated according to the formula (*Parasassi et al., 1990*):

$$GP = \frac{(I_{440} - I_{490})}{(I_{440} + I_{490})}$$

where I_{440} and I_{490} are the emission intensities at 440 nm and 490 nm respectively. Laurdan GP variation as a function of time was calculated after α-La addition to POPC:POPG vesicles at

L/P 20:1 and 250:1. As control measurement, we show that Laurdan GP value doesn't change after adding 0.1 M NaCl, pH2.

CD measurements. CD spectra of α-La and samples at the two different L/P were recorded on a Jasco J-715 spectropolarimeter in the far-UV region (194 nm to 270 nm), using quartz cuvettes. For each spectra 20 accumulation were acquired, with data interval 0.1 nm, bandwidth 1.0 nm, scan speed 50 nm/min. All spectra were acquired at room temperature. At L/P 20:1 spectra were acquired using a path length of 1 mm, with protein and lipid concentration of 10 μM and 200 μM, respectively. At L/P 250:1 spectra were acquired using a 5 mm path cuvette, with protein and lipid concentration of 1.6 μM and 400 μM, respectively. In the latter case, in order to improve S/N ratio, we decided to increase the path length and double the protein concentration, clearly maintaining the ratio between lipid and protein (250:1). As control, we verified that at L/P 20:1 the observed effects were the same also after doubling both protein and lipid concentration.

2-photon and confocal fluorescence microscopy. GVs were imaged before and after α-La addition. 500 μL sample aliquots were deposited in Chambered Coverglass (Nunc Lab-Tek II) and imaged using a Leica TSC SP5 confocal laser scanning microscope, with a 63x oil objective, NA= 1.4, free working distance 0.1 mm, scanning frequency 200 Hz. For all measurements, at L/P 20:1 protein and lipid concentration were 10 μM and 200 μM, respectively; at L/P 250:1 protein and lipid concentration were 0.8 μM and 200 μM, respectively. Control measurements showed that results are the same independently of the sample holder. The same changes in vescicle morphology were observed in both cuvette sample and chambered coverglass sample.
Colocalization experiments. 1024x1024 pixel images were acquired with a sequential acquisition of two channels: Atto 647 emission was acquired in the range 653-750 nm, using λ_{exc} = 633 nm; Laurdan emission was acquired in the range 430-505 nm using 2-photon excitation (Spectra-Physics Mai-Tai Ti:Sa ultra-fast laser), with excitation wavelength 780 nm.
GVs morphology changes. GVs morphology changes after 10 μM Atto 647-labeled α-La addition (L/P 20:1) are shown as the overlap of Atto 647 emission channel and phase contrast channel. Fluorescence confocal images have been acquired in the range 653-750 nm, with λ_{exc} = 633 nm, with a 512x512 pixel resolution.

Laurdan GP imaging. 256x256 pixels images were acquired using 2-photon excitation (Spectra-Physics Mai-Tai Ti:Sa ultra-fast laser) at 780 nm and collecting the emission in the range 430-450 nm and 485-505 nm, simultaneously. In order to obtain 256x256 GP maps, providing GP value in each pixel of the image, data were analyzed using SimFCS software, developed at the Laboratory for Fluorescence Dynamics (University of California, Irvine, CA, USA). Calibration of the GP scale was obtained using a Laurdan GP=0.2 for a standard Laurdan solution in DMSO at 22°C (*Gaus et al., 2006; Owen et al., 2012*).

Raster Image Correlation Spectroscopy (RICS) measurements. Images were acquired with an Olympus FluoView 1200 confocal laser scanning microscope (Olympus), using a 60x 1.35 NA objective lens. Atto 647 NHS ester was excited using a 635 nm laser, using an emission filter for the red emission channel with a bandwidth 655 – 755 nm. Data were collected in the photon-counting mode. 256x256 pixel resolution images were acquired with a pixel size of 0.05 μm, collecting 70 frames for each image stack, with a scan speed of 12.5 μs per pixel (line time 4.325 ms, frame time 1.155 s). System calibration was performed using a solution of Alexa 647 in phosphate buffer at pH 7.4, setting the diffusion coefficient to 300 $\mu m^2/s$ and determining the laser beam waist ω_0, which was $\omega_0 = 0.36$ μm. A scan speed of 4 μs per pixel (line time 2.12 ms, frame time 0.564 s) was used for Alexa 647 dye. RICS analysis was performed using the RICS algorithm of SimFCS software (Laboratory for Fluorescence Dynamics, University of California, Irvine, CA, USA). RICS experiments were performed right after the labeling procedure, as control measurements in order to prove protein labeling and to verify the absence of free dye in the sample. In Figure 2.7 RICS analysis on free Atto 647 dye as well as on Atto 674-labeled α-La is shown. RICS analysis on Atto 647 in solution indicates the fast free diffusion of a small molecule and the fit gives $D = 280\ \mu m^2 s^{-1}$. The analysis on Atto 647-labeled α-La indicates a slower diffusion, with $D = 90\ \mu m^2 s^{-1}$.

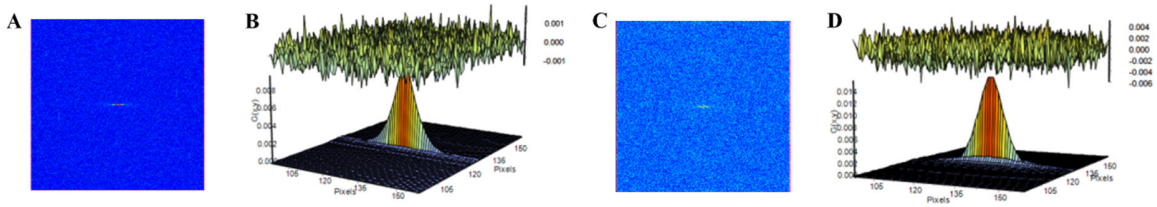

Figure 2.7 RICS analysis on **(A, B)** Atto 647 and **(C, D)** Atto 647-labeled α-La. **(A, C)** spatial autocorrelation functions and **(B, D)** ACF fit. Images have been acquired with 0.050 µm x 0.050 µm pixels, 12.5 µs pixel dwell time, 4.325 ms between lines, 1.155 s between images and a laser beam radius of 0.36 µm. All images have a 256x256 pixels resolution. RICS analysis on Atto 647 in solution gives a diffusion coefficient D = 280 $\mu m^2 s^{-1}$. The analysis on Atto 647-labeled α-La indicates a slower diffusion, with D = 90 $\mu m^2 s^{-1}$.

Fluorescence Lifetime Imaging Microscopy. Fluorescence Lifetime Imaging Microscopy (FLIM) data were acquired in the time domain using a Leica TSC SP5 inverted microscope with a 63x/1.4 oil objective (Leica Microsystems), coupled with a PicoHarp 300 TCSPC Module (PicoQuant). The excitation wavelength for Atto 647 NHS ester was set to 633 nm, with 80 MHz repetition rate. 256x256 pixel resolution images were acquired, until 100 counts were collected in the brightest pixel of the image. Protein and lipid concentration were, respectively, 10 µM and 200 µM (at L/P 20:1), and 0.8 µM and 200 µM (at L/P 250:1). FLIM measurements have been analyzed using the Phasor analysis, introduced by Digman et al. (*Digman et al., 2008*). Data have been analyzed using SimFCS software (Laboratory for Fluorescence Dynamics, University of California, Irvine, CA, USA). FLIM calibration was obtained measuring the lifetime of Atto 647 NHS ester in DMSO, which is known to be 2.4 ns, as reported in Sigma-Aldrich product information data sheet.

2.3.2 Fibril formation in α-La samples

α-La sample preparation. Bovine α-lactalbumin (Davisco, JE 010-5-410) and Thioflavin T (ThT) (Sigma, T3516-25G) were used without further purification. All the measurements were performed in NaCl 0.1 M, pH 2. Samples at different concentrations were freshly prepared and filtered through 0.10 µm filters (16553, Sartorius). Protein concentration was determined by means of a Shimadzu UV-2401PC UV-Vis spectrophotometer, using an extinction coefficient $\varepsilon^{1\%}$=20 at λ=280 nm (*Brew, 2003*). A stock solution of ThT (3 mg/ml) was prepared in pure water and stored protected from light exposure at 4°C. Just before each fluorescence

measurement, aliquots of ThT solution were added to the samples to a final ThT concentration of 124 μM (in situ measurements).

Fluorescence spectroscopy and Rayleigh scattering measurements. Fluorescence spectra were obtained using a Jasco FP-8500 equipped with a Jasco ETC-815 peltier as temperature controller. To investigate α-La aggregation process, samples were positioned in a 1 cm path PMMA UVgrade cuvette (Kartell) containing a PTFE crosswise magnetic stirring bar. All emission spectra were acquired with 0.5 nm wavelength interval, emission and excitation bandwidth of 5 nm, integration time of 1 s, scan speed of 100 nm/min. At the same time, Rayleigh Scattering at 90° was also measured as the maximum of the elastic peak of excitation light. Intrinsic fluorescence emission spectra were obtained at room temperature, with continuous stirring, under excitation at 290 nm, in the range 285-500 nm, for time intervals comparable with those of aggregation kinetics. ThT fluorescence spectra were obtained at different temperatures ranging from 33°C to 70°C, with continuous agitation, at different stirring speed (60 rpm, 180 rpm, 360 rpm, 540 rpm 800 rpm); measurements without stirring were also carried out to compare results. ThT fluorescence emission spectra, after thermal equilibration, were acquired every 134 seconds under excitation at 440 nm, in the range 435-650 nm. In order to describe the aggregation process, we used two parameters: the ThT final fluorescence value (FFV) and the reciprocal of the time required to reach 50% of the final fluorescence value ($1/t_{50\%}$), as previously done for insulin (*Foderà et al., 2008*). ThT FFV is the plateau value of ThT fluorescence emission and indicates the amount of amyloid structures formed in the sample; $1/t_{50\%}$ is the inverse of time at which the ThT fluorescence emission reaches half of the plateau value and can be used as a parameter indicating the rate of the kinetics.

Confocal fluorescence microscopy measurements. At the end of aggregation process, 20 μl aliquots of 1:10 H_2O diluted samples were imaged at 1024 x 1024 pixel resolution using a Leica TSC SP5 confocal laser scanning microscope, with a 63x oil objective, NA= 1.4, free working distance 0.1 mm, scanning frequency 400 Hz. The excitation was set at 458 nm and the emission was detected in the range 478-600 nm.

FTIR absorption measurements. For FTIR analysis, at the end of aggregation process samples were lyophilized and dissolved in D_2O (Deuterium oxide, 99.9%, Sigma Aldrich 151882-10G). FTIR absorption measurements were performed using a Bruker Vertex 70 spectrometer FT-IR spectrometer, after purging the sample compartment with nitrogen to reduce water vapor. Spectra were acquired with a spectral resolution of 2 cm^{-1}, transferring the sample to the sample cell consisting of two CaF_2 windows separated by a 0.05 mm Teflon spacer. Spectra were calculated with respect to the spectrum of the empty cell. Once acquired, spectra were subtracted of D_2O contribution. In order to determine aggregate secondary structure percentage content, a deconvolution of Amide I band was performed, using spectrum second derivative to identify the overlapping peaks under the Amide I' band. The minimums in the second derivative indicate the centers of the overlapping peaks. Once five components were identified, absorption bands were assigned to the different secondary structures, depending on the assignments reported in literature (*Barth, 2007; Pelton and McLean, 2000*). Amide I' components were obtained performing a fit with five Gaussian components, using the residue method with the Peak fit program. The secondary structure percentage content of the different samples was determined with an error range of 4%.

Transmission electron microscopy measurements. An analysis of aggregate morphology at nanometric scale was also performed by means of Transmission electron microscopy (TEM). Imaging was performed on a Philips CM 100 Transmission Electron Microscope using a standard protocol (*Smith et al., 2012; Foderà et al., 2012*). At the end of the aggregation process, samples were diluted 50-fold and 5 µl aliquots were placed on Copper 400 mesh grids (Agar Scientific, Stansted, UK) coated with Formvar and carbon film. The grid was left for 60 seconds after which 10 µl of distilled water was added and the excess water was removed. Then, 10 µl of 2% uranyl acetate (Agar Scientific) was added and the grid left for 30 seconds. Last, two 10 µl drops of distilled water were placed on the grid, the excess water was removed and the grid was left to dry.

Interaction between model membranes and α-La at neutral pH. Giant vesicles were prepared using the protocol described in the previous section, hydrating lipids with 0.1 M phosphate buffer. α-La in both native and aggregate state was added to liposomes at lipid:protein ratio

20:1. Laurdan stained vesicles were imaged before and after protein addition using a Leica TSC SP5 confocal laser scanning microscope, with a 63x oil objective, NA= 1.4. Laurdan emission was acquired in the range 430-505 nm using 2-photon excitation at 780 nm (Spectra-Physics Mai-Tai Ti:Sa ultra-fast laser).

2.3.3 Protein diffusion across cell membrane: the Image Mean Square Displacement (iMSD) analysis

Sample preparation. CHO-K1 cells were cultured in a humidified 5% CO_2 atmosphere at 37°C, in Dulbecco's Modified Eagle Medium/Nutrient Mixture F-12 media supplemented with 10 % Fetal Bovine Serum and 1 % penicillin-streptomycin. Cells were plated on 35 mm glassbottomed dishes, previously coated with fibronectin, and transiently transfected with EGFR-EGFP plasmid using the Lipofectamine 2000, according to the manufacturer's instructions. Generally, 1 μg of plasmid (diluted with PBS) was incubated with 5 μl of Lipofectamine for 30 min and added to the cell dish containing fully supplemented media. The cells were maintained in a humidified, 5% CO_2 atmosphere at 37°C and used within 48 h.

TIRF measurements. Measurements were performed on an Olympus IX81 microscope equipped with a Photometrics Evolve 512 EMCCD Camera. The fluorescence signal was collected using an Olympus TIRF UIS2 PlanApo N 60x (NA = 1.45) oil immersion objective. The excitation wavelength for EGFR-EGFP was set to 488 nm. 256x256 pixel resolution images have been acquired with an exposure time of 20 ms and a pixel size of 0.138 μm.

Chapter 3

Alpha-lactalbumin interaction with model membranes

As previously discussed in Chapter 1, the interaction between proteins and cell membranes is a fundamental topic in recent research, for several reasons. Pathogenic proteins are considered to be involved in human diseases because of their interaction, in the native or aggregate state, with cell membranes (*Butterfield and Lashuel, 2010; Stefani, 2010; Bucciantini et al., 2014*). Moreover, several biological processes are regulated by the interaction between cell membranes and amphitropic proteins, which can be found both in the cytosol and associated to membranes (*Burn, 1988; Johnson and Cornell, 1999*).

In this Chapter, the interaction between molten globule α-La and giant vesicles has been investigated at two different lipid:protein ratios by means of both spectroscopy and microscopy techniques. Upon protein addition, variations in vesicles morphologies have been visualized by means of two-photon microscopy, using Laurdan dye stained vesicles in order to simultaneously quantify membrane fluidity changes. Two color colocalization experiments have been also performed labeling α-La with the red fluorescent dye Atto 647, to better characterize the structures formed upon interaction. Final structures have been further investigated performing Fluorescence Lifetime Imaging Microscopy measurements, in order to obtain information on protein local environment. Changes in protein structure have been investigated with spectroscopy methods, performing intrinsic fluorescence and Circular Dichroism measurements.

3.1 Results and discussion

In Figure 3.1 representative 512x512 images of 200 μM POPC:POPG liposomes at pH 2 (phase contrast channel) acquired as a function of time after addition of 10 μM Atto 647-labeled α-La (blue fluorescence channel) are shown. Molar ratio Atto 647-labeled α-La:α-La is 1:100. As can be seen, fluorescence signal indicating the presence of α-La is found to be localized at the membrane. Fluorescence intensity measured at the liposomes surface increases as a function of time, indicating a progressive increase of protein concentration in these regions. In the first minutes of the interaction process, a quick and dramatic change in liposome morphology also occurs (Figure 3.1A – 3.1F).

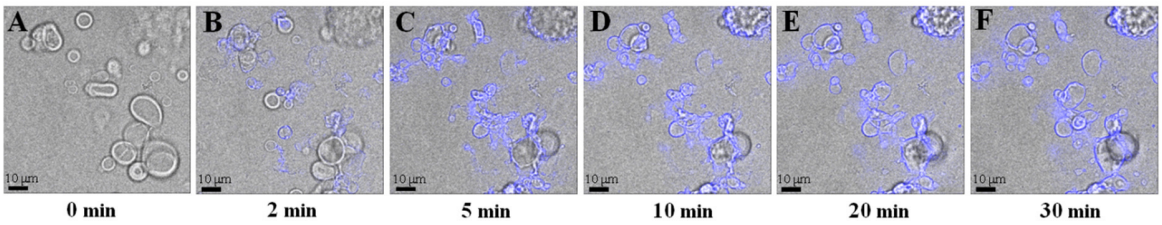

Figure 3.1 POPC:POPG morphology changes as a function of time after the addition of 10 μM Atto 647-labeled α-La (lipid:protein ratio 20:1). **(A-F)** Liposome morphology **(A)** before and after **(B)** 2 min, **(C)** 5 min, **(D)** 10 min, **(E)** 20 min and **(F)** 30 min from protein addition. Panels are the overlap of confocal fluorescence (Atto 647 fluorescence emission) and phase contrast (liposomes) channel. Fluorescence confocal images have been acquired in the range 653-750 nm, with λ_{exc} = 633 nm. Images have a 512x512 pixel resolution. Scale bar is 10 μm.

Within few seconds after protein addition, α-La locates on accessible liposome surfaces and modifies vesicles morphology, possibly inserting into the lipid bilayer. Before protein addition, monolamellar as well as multilayer GVs are observed and the vesicles morphology in the sample appears to be highly heterogeneous in shape and size. Once α-La is added, sudden changes in membrane morphology occur, which lead toward regular roundish structures whose average size is smaller than the one of initial liposomes. In Figure 3.2 a representative image of the sample is reported in stationary conditions, after 24 hours from protein addition.

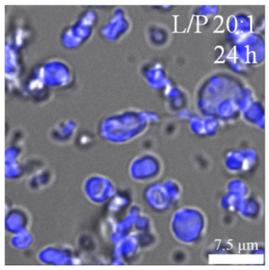

Figure 3.2 POPC:POPG morphology changes after interaction with 10 µM Atto 647-labeled α-La (lipid:protein ratio 20:1). Details of final structures morphology after 24 hours from protein addition. Fluorescence confocal images have been acquired in the range 653-750 nm, with λ_{exc} = 633 nm. Image has been acquired with a 1024x1024 pixel resolution, in the range 653-750 nm using λ_{exc} = 633 nm. Scale bar is 7.5 µm.

Our results suggest that, in the used experimental conditions, a sudden interaction between α-La and GV membrane occurs, which leads to hybrid micrometric protein-lipid structures. Membrane modification and disruption as well as membrane collapse, clustering and budding have been observed in dependence on several factors, such as protein structure, aggregation state, protein concentration, lipid composition and membrane curvature (*Bañuelos and Muga, 1996b; Zhu et al., 2003; Rødland et al., 2005; Butterfield and Lashuel, 2010; Vetri et al., 2011; Al Kayal et al., 2012; Ruggeri et al., 2013; Wen et al., 2013; Van Maarschalkerweerd et al., 2014*). Studies on α-La interaction with small or large unilamellar vesicles indicated that the loss of bilayer integrity is dependent on membrane composition and charge, but also on pH which controls protein and membrane global charge as well as protein conformation (*Agasøster et al., 2003; Bañuelos and Muga, 1996b; Rødland et al., 2005; Borro et al., 2017*). Interaction dependence on lipid bilayer charge was also highlighted in studies focused on the interaction between GUVs and globular proteins (*Ruggeri et al., 2013*). Changes in membrane morphology have been observed upon the addition of bovine α-La complexed with oleic acid (BLAOA) to giant unilamellar vesicles (*Wen et al., 2013*). Upon exposure to BLAOA, a complex resembling BAMLET with respect to physiochemical properties, cytotoxicity and ability to damage membranes (*Brinkmann et al., 2011, 2013*), vesicles are found to develop blebs and eventually collapse (*Wen et al., 2013*). Variations in membrane properties have been also observed after the addition of alpha-synuclein (αSN) to charged vesicles, leading to membrane disruption *(Zhu et al., 2003; Van Maarschalkerweerd et al., 2014*). In particular, αSN addition in both monomeric and intermediate states induces a rapid destabilization of the membrane, resulting

in smaller species, sized below the instrumental resolution, with a more rigid environment (*Van Maarschalkerweerd et al., 2014*). In addition, vesicle clustering and fusion were found to follow the insertion of lysozyme in the GUVs lipid bilayer (*Al Kayal et al., 2012*). The extent of changes in membrane permeability is found to be dependent on protein concentration. It has been suggested that protein adsorption rapidly occurs upon protein addition to vesicles, leading to some degree of lipid reorganization, but that a protein critical surface density threshold is needed to induce membrane leakage (*Ruggeri et al., 2013*). Despite of the interaction occurring between several common water-soluble dyes and model lipid membranes, which could influence the interaction process and cause misleading fluorescent signals (*Hughes et al., 2014*), experiments show that, in the used experimental conditions, the effects of protein addition to liposomes are the same regardless of the use of labeled or unlabeled protein. In Figure 3.3, representative images of Laurdan stained POPC:POPG giant vesicles before protein addition (Figure 3.3A) and after 24 hours in both absence (Figure 3.3B) and presence (Figure 3.3C) of protein are reported. Control measurements clearly show that no variations in morphology occur in protein absence and that interaction leads to the formation of final roundish structures, also when the unlabeled protein is added. Moreover, an increase in Laurdan fluorescence intensity can be observed upon protein addition.

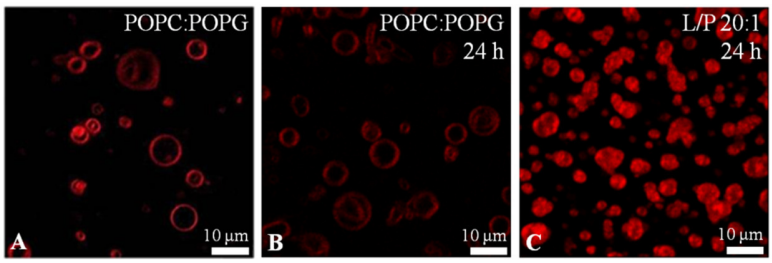

Figure 3.3 Laurdan stained POPC:POPG giant vesicles **(A)** before and **(C)** after 24 hours from α-La addition at lipid:protein ratio 20:1. Protein concentration is 10 µM. **(B)** Vesicles morphology after 24 hours in absence of protein is also showed. Two-photon microscopy images have been acquired in the range 430 – 450 nm, with excitation wavelength 780 nm, with a 256x256 pixel resolution. Scale bar is 10 µm.

The observed interaction between α-La and GVs (Figure 3.1A-3.1F) suggests that the addition of 10 µM α-La causes a quick destabilization of liposome membrane and vesicle compaction in uniform structures. As α-La molten globule is highly flexible and contains a partially

unstructured region where hydrophobic patches are solvent exposed, both adsorption and insertion of the protein in the lipid bilayer may be at the basis of the observed phenomenon. They may separately occur in different time scales or being simultaneously observed. It is likely that the combination of electrostatic interactions with the polar heads of lipids and hydrophobic interactions with the lipid chains results in a quick adsorption of α-La to lipid bilayer, followed by the insertion into the lipid bilayer, that takes place above a critical surface density and is driven mainly by hydrophobic interactions. This is in line with the multistep process describing the membrane association with lysozyme (*Al Kayal et al., 2012*).

The process was investigated at two lipid:protein (L/P) ratios. We will refer to the sample obtained by adding α-La to POPC:POPG giant vesicle at L/P 20:1 and to the one resulting from protein addition to liposome at L/P 250:1 as "20:1 sample" and "250:1 sample", respectively. In order to consider samples in stationary conditions, we show the result of interaction process 24 hours after α-La addition.

For both 20:1 sample and 250:1 sample we show representative fluorescence microscopy measurements acquired in two channels.

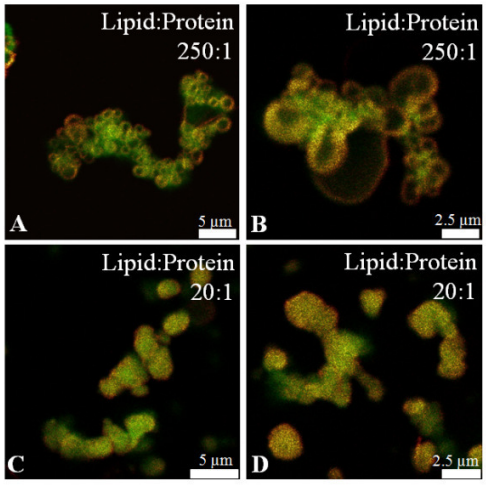

Figure 3.4 Morphology of Laurdan stained giant vesicle after addition of Atto 647-labeled α-La. **(A - D)** Representative images of POPC:POPG giant vesicles after α-La addition at **(A, B)** L/P 250:1 and **(C, D)** L/P 20:1. Images are the overlap of two-photon microscopy measurements (Laurdan fluorescence emission) and confocal microscopy images (Atto 647 fluorescence emission). Two-photon and confocal microscopy images have been acquired in the range 430-505 nm (λ_{exc} = 780 nm) and 653-750 nm (λ_{exc} = 633 nm), respectively. Scale bar is **(A, C)** 5 µm and **(B, D)** 2.5 µm. All images have a 1024x1024 pixel resolution.

In Figure 3.4 the merge of the measurements on Laurdan stained GVs (red channel, 2-photon microscopy images) and Atto 647-labeled α-La (green channel, confocal microscopy images), sequentially acquired, is reported. These colocalization experiments allow to further investigate the sample, giving information on the spatial overlapping of the fluorescence intensity of the two dyes. We report in Figure 3.4A and 3.4B measurements on Laurdan stained giant vesicles after addition of 0.8 μM Atto 647 labeled α-La (250:1 sample) and in Figure 3.4C and 3.4D measurements on Laurdan stained giant vesicles after addition of 10 μM Atto 647 labeled α-La (20:1 sample). In particular, panels B and D show details of the resulting structures. Laurdan dye is used to stain the membrane in order to visualize liposome morphology. In the following, the detailed analysis of its signal will be used to investigate membrane fluidity changes. Results indicate high level of colocalization (visualized as yellow pixels) of fluorescence signal in the two channels, for both samples. At the equilibrium, micrometric structures with different morphologies are observed and these hybrid structures contain both protein and lipids. This further support α-La internalization into membrane leading to changes in liposome morphology. Measurements in Figure 3.4 clearly show that, at the equilibrium, 250:1 and 20:1 sample morphology is completely different from the initial one. The final morphology of 250:1 sample (Figure 3.4A and 3.4B) is highly heterogeneous. POPC:POPG vesicles and protein are wrapped in large mixed structures, where structures resembling liposomes in their initial state are still present. Sample heterogeneity decreases in 20:1 sample (Figure 3.4C and 3.4D). As it is evident and in line with results showed in Figure 3.2 and 3.3C, roundish structures full of protein/lipid material smaller than the initial vesicles are present. Interestingly, measurements reported in Figure 3.4C and 3.4D clearly show that in 20:1 sample α-La is distributed on every round structure within the instrumental resolution. By contrast, in 250:1 sample α-La doesn't allocate on every vesicle. Figure 3.5 shows the red channel (Laurdan fluorescence emission) and the green one (Atto 647 fluorescence emission), sequentially acquired, for a representative area of the 250:1 sample. It is evident the presence of liposomes (see arrows) where the green signal attributable to the presence of protein at the membrane is absent or barely visible. This suggests that protein concentration in 250:1 sample is low enough not to saturate every possible interaction site in membrane.

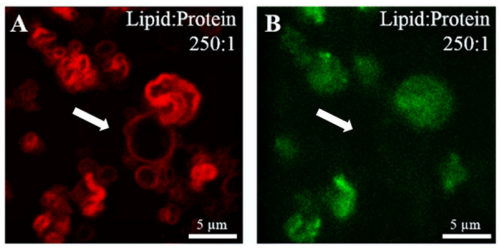

Figure 3.5 Representative images of POPC:POPG giant vesicles after α-La addition L/P 250:1. **(A)** Laurdan fluorescence emission channel, acquired in the range 430-505 nm with λ_{exc} = 780 nm. **(B)** Atto 647 fluorescence emission, acquired in the range 653-750 nm with λ_{exc} = 633 nm. Arrows indicate a group of vesicles where protein is absent or barely visible. Images have a 512x512 pixel resolution. Scale bar is 5 µm.

Moreover, an inhomogeneity in Atto 647 fluorescent intensity is clear, more evident in 250:1 sample, which reflects an inhomogeneity in protein distribution. At pH 2, POPC:POPG liposomes are characterized by an heterogeneous surface charge distribution, being a small fraction of POPC positively charged and a small fraction of POPG negatively charged (see Chapter 2, Section 2.3.1), while α-La is characterized by a positive charge. Since protein adsorption on vesicles is driven by electrostatic and hydrophobic interactions, it is likely that the heterogeneous surface charge distribution is the cause of the inhomogeneity in protein distribution. Over a concentration threshold value, hydrophobic interactions drive the insertion of α-La into the membrane, leading to the observed morphological changes and to an inhomogeneity in α-La distribution due to protein excess. Given the differences occurring at the two L/P, it is evident that L/P is a crucial factor for the interaction process. Final morphology and structure depend on the concentration of interacting protein.

Figure 3.4 clearly shows the differences in morphology obtained depending on protein concentration, at L/P 250:1 and L/P 20:1. In the hypothesis that different molecular interactions are at the basis of evident differences in the microscale morphology of lipid-protein structures, we performed FLIM analysis of the two samples, and in Figure 3.6 we report the phasor analysis of FLIM measurement performed on Atto 647-labeled α-La in aqueous solution, in 20:1 sample and in 250:1 sample. In particular, the analysis of Atto 647 fluorescence signal in terms of lifetimes can give information on the environment of this fluorophore.

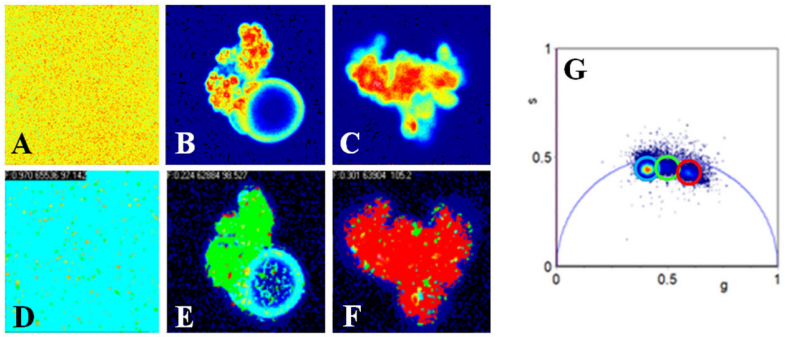

Figure 3.6 Phasor analysis of FLIM measurements on Atto 647-labeled α-La after 24 hours from addition to giant vesicles, at **(B, E)** L/P 250:1 (10 μm α-La) and **(C, F)** L/P 20:1 (0.8 μm α-La). **(A, D)** FLIM measurement of Atto 647-labeled α-La in solution (NaCl 0.1 M, pH 2). **(A, B, C)** Intensity images, showing the different morphology of final structures. Images have a 256x256 pixel resolution. Image size is **(A, B)** 30.75 μm x 30.75 μm and **(C)** 15.08 μm x 15.08 μm. **(D, E, F)** Phasor color maps, in which each pixel is colored depending on the lifetime of the dye. **(G)** Phasor plot of FLIM measurements on Atto 647-labeled α-La. Clusters corresponding to the different samples have been identified in the phasor plot by colored circles: red circle (L/P 20:1), green circle (L/P 250:1), cyan circle (Atto 647-labeled α-La in solution). Pixel colors in phasor color maps correspond to the circles in phasor plot.

The Phasor approach for image analysis was introduced by Digman et al. (*Digman et al., 2008*) and allows to avoid fitting the fluorescence decay using exponentials. FLIM data are analyzed in the phasor space observing clusters of pixels in specific regions of the phasor plot (*Digman et al., 2008*). The phasor analysis represents in a polar plot (the Phasor plot) the cosine and sine Fourier transforms of the emission decay collected in each pixel of the image. Each image pixel is therefore mapped to a point in the phasor plot. All monoexponential decays lie on the "universal circle", defined as the semicircle of radius ½ going from the point (0,0), corresponding to a lifetime $\tau = \infty$, to the point (1,0), corresponding to a lifetime $\tau = 0$. The combinations of two single exponential components lie inside the semicircle, being along the line joining the phasors of the two monoexponential states (*Digman et al., 2008; Stringari et al., 2011*). Since its introduction, the phasor analysis has been widely used both with extrinsic and intrinsic fluorophores (*Stringari et al., 2011; Battisti et al., 2012; Stringari et al., 2012; Golfetto et al., 2013; Plotegher et al., 2015; Ma et al., 2016; Sameni et al., 2016*) and represent a valuable and simple tool to extract information from FLIM measurements.

In Figure 3.6 the phasor analysis of representative images obtained for the different samples is shown. Figure 3.6B and 3.6C show the fluorescence intensity images of Atto 647-labeled α-La in 250:1 sample and 20:1 sample, respectively. In Figure 3.6A the intensity image of Atto 647-

labeled α-La in solution (NaCl 0.1 M, pH 2) is also showed. As previously discussed (Figure 3.4), images show the evident difference in final structures morphology, depending on concentration of added protein. Figure 3.6D – 3.6F show the phasor color maps of the FLIM images, in which each pixel is colored depending on Atto 647 lifetime. FLIM data analysis by means of phasor approach is performed by detecting clusters of pixels in specific regions of the phasor plot showed in Figure 3.6G. In the phasor plot, in which each point corresponds to a pixel of the connected image, three main distribution are evident, which have been selected with three different cursors (cyan, green and red). Corresponding pixels are mapped back with selected color to the image pixels in panels D, E and F relative to solution sample, 250:1 sample and 20:1 sample, respectively. In Figure 3.6D, as expected, the fluorescence signal is uniformly distributed and no structures with size over resolution are present, the phasor color map is evidently uniform and fluorescence signal in every pixel show same lifetime, this being indicated by the fact that only cyan pixels are found in the image. In Figure 3.6E, the majority of pixels is highlighted in green while in Figure 3.6F the majority of pixels is highlighted in red, indicating that the two samples are mainly characterized by different lifetime of Atto dye. This suggests that the observed structures at L/P 20:1 and 250:1 are formed by means of various molecular interactions taking place during protein insertion into the lipid bilayer and leading to different protein local environments. Moreover, the coexistence of pixels colored in both cyan and green in Figure 3.6E (L/P 250:1) highlights the presence of two different environments surrounding the dye. Interestingly, the difference in lifetime reflects the one in morphology: larger changes in morphology correspond to larger modification in lifetime value, with respect to the one measured on protein in solution. In particular, in the 20:1 sample, where protein is located on the previously observed regular, roundish and full structures, the Atto 647 signal is manly characterized by the shorter fluorescence lifetime (red). In the 250:1, structures having a wrapped morphology represent the dominant population (green), while structures with a liposome morphology have the same lifetime measured for Atto-labeled protein in aqueous solution (cyan).

Due to the properties of the used dye, the different lifetime can be ascribed to a different polarity of protein local environment in the two samples. A study focused on several red-absorbing fluorescent dyes highlighted the dependence of fluorescence lifetime on viscosity and polarity. In particular, it was shown that the lifetime of two red-absorbing Atto dyes weakly depends on

viscosity, being largely influenced by solvent polarity (*Buschmann et al., 2003*). Recently, changes in the fluorescence quantum yield of both hydrophobic and hydrophilic molecules embedded inside a lipid bilayer have been reported in comparison with the same type of molecules dissolved in an aqueous solution (*Schneider et al., 2017*). Differences in quantum yields have been attributed to the strong difference of polarity existing between an aqueous buffer and a lipid bilayer, which strongly impacts on fluorescence properties (*Schneider et al., 2017*). Therefore, differences in lifetime values likely reflect a difference in polarity between structures formed at L/P 20:1 and 250:1. Then it is possible to speculate that the three distinguishable lifetime correspond to different level of insertion of the Atto labeled protein in the lipid membrane or to simple absorption, where protein is mostly interacting with solvent.

It can then been speculated that the different lifetimes take account of the different protein local environment, allowing to determine if the labeled protein is surrounded by the solvent, by lipids, or by protein. At low protein concentration (Figure 3.6B), it is evident the presence of protein surrounded by solvent (cyan pixels) that have the same lifetime of Atto-labeled α-La in solution (Figure 3.6D) and it is likely that green pixels indicate an environment in which the labeled protein is buried in a lipidic structure. At high protein concentration (Figure 3.6F), the excess of protein is responsible for the existence of a third environment, in which protein is likely surrounded by protein. Therefore, lifetime measurements allow distinguishing between adsorption and insertion state.

Our results are in line with data presented in literature. It was shown that, in the interaction between globular proteins and negative charged vesicles, there is a minimum protein concentration, depending on the considered protein, which is required to induce membrane destabilization and leakage (*Ruggeri et al., 2013*). Below the minimum concentration, adsorption to lipid bilayer is observed, causing a small membrane reorganization (*Ruggeri et al., 2013*). It is also important to note that previous studies on several α-La conformers have shown that protein adsorbs onto the membrane surface if the lipid bilayer is in the gel phase, while the membrane-bound state is the inserted one if the bilayer is the liquid phase. It is also highlighted how the membrane permeability barrier can be efficiently disrupted only by the inserted state and not by the adsorbed one (*Bañuelos and Muga, 1996a*). Results in Figure 3.4 suggest that it is likely that α-La adsorption to POPC:POPG vesicles occurs at low concentrations (0.8 μM, L/P 250:1), with a following low destabilization of the lipid bilayer

whose morphology is still similar to the initial one. As the interaction process is predominantly ruled by electrostatic and hydrophobic interactions, it is likely that α-La distribution onto the vesicles surface is not uniform (at L/P 250:1, Figure 3.4A and 3.4B), due to both the non-uniform distribution of charges onto the liposome surface and the low protein concentration in the sample. Insertion will probably occur only into the membrane surfaces were protein concentration exceeds the concentration threshold; elsewhere adsorption will be the predominant interaction with a consequent low destabilization of membrane morphology and structure.

Above presented results indicate a fast internalization of protein in liposome structure, leading to hybrid microstructures whose size and morphology depends on L/P in the sample as well as on the amount of protein accumulated on and in the membrane. This should results in a structural modification of protein as well, in different extents. To verify if the observed changes also affect protein structure we report in the following an investigation on α-La secondary structure.

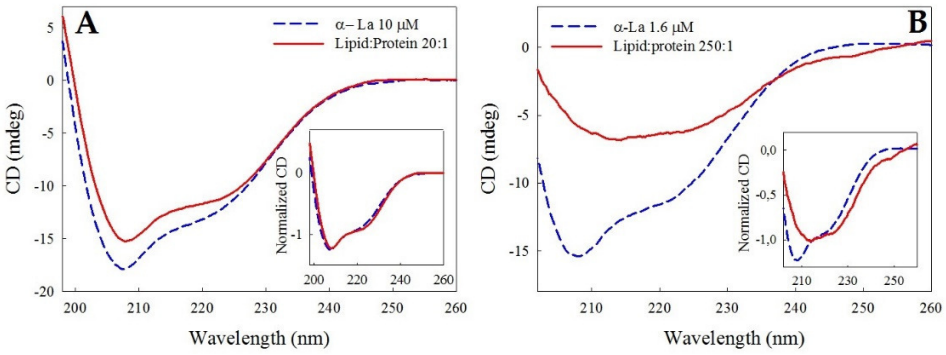

Figure 3.7 Far-UV spectra of α-La at pH 2 (blue dashed line) and of α-La after 24 hours from addition to POPC:POPG giant vesicles (red continuous line) at **(A)** L/P 20:1 and **(B)** L/P 250:1. Inset shows spectra normalized at 215 nm. For each spectrum 20 accumulations have been acquired in the range 194-270 nm, with data interval 0.1 nm, bandwidth 1.0 nm, scan speed 50 nm/min. All spectra have been acquired at room temperature, with a path length of **(A)** 1 mm and **(B)** 5 mm.

In Figure 3.7, far-UV spectra of α-La at pH 2 (blue dashed line) and of α-La after 24 hours from addition to giant vesicles (red continuous line) are shown, for 20:1 and 250:1 samples. The inset in panels A and B show α-La spectra at pH 2 (blue dashed line) and after addition to liposomes (red continuous line), normalized at 215 nm. POPC:POPG CD signal obtained with the same

parameters was subtracted to the acquired spectra. Due to experimental reasons, 250:1 sample CD spectra have been acquired modifying the protein concentration, clearly respecting the L/P 250:1 (see Chapter 2, Section 2.3.1). Control measurements have shown that the observed changes in CD spectrum only depend on the L/P, and not on protein concentration. Data with better S/N ratio are reported.

At pH 2, α-La is in the molten globule state, which has native-like secondary structure but a not well-defined tertiary structure *(Kuwajima, 1996*). The CD spectrum on α-La sample in solution (Figure 3.7, blue dashed line), as expected, reveals the presence of both α-helices and β-sheet structures (*Kelly et al., 2005*); this is a typical result for α-La in the molten globule state, in line with several studies on both Human and Bovine α-Las in different states (apo or holo), in acidic conditions (*Lala and Kaul, 1992; Svensson et al., 1999; Chakraborty et al., 2001; Polverino de Laureto et al., 2001, 2002; Ramboarina and Redfield, 2003; Chenal et al., 2005)*. At L/P 20:1 (Figure 3.7A), slight changes in the spectrum shape can be observed, with an increase of the signal at both 208 nm and 222nm. Larger changes in the spectrum are evident at L/P 250:1 (Figure 3.7B). In addition to a larger reduction of the CD signal, there is an evident change in spectrum shape in the 250:1 sample, indicating the loss of the α-helical structural contributions with a resulting change in the peak at 208 nm. In particular, the insertion of α-La into the lipid bilayer could result in a difference in the α-helices and β-sheet content, with an increase of β-sheet and a decrease of α-helix structures. Observed modification in CD spectra may arise from changes in protein secondary structure occurring in both samples in different extent or from similar modification occurring only in a sample subpopulation. In other words, it is possible to infer that the observed CD spectra are the result of the superimposition of two main components: one due to the modified structure of protein interacting with lipid membrane and one ascribable to α-La still free in solution or interacting with protein. Relative contribution of the two spectra in this hypothesis is likely to depend on L/P. At lower L/P, i.e. at the higher protein concentration used in our experiments (10 μM), it is likely that final sample includes both protein inserted into the lipid bilayer and protein still unbound or interacting with protein: the different states could in principle lead to different CD signals, having different secondary structures. At the equilibrium, the signal coming from the protein that is not inserted into the membrane could prevail on the other, resulting in a small difference between the initial and the final CD spectrum.

At high L/P, i.e. at the lower protein concentration, the evident modification in CD spectrum possibly arises by reduced presence of α-La not interacting with lipids.

α-La structure in its native or molten globule state is known to contain two hydrophobic cores mainly involving residues arranged in the α-helices (*Chrysina et al., 2000*). In particular, the molten globule is characterized by a core with a native-like packing and well defined secondary structure, surrounded by highly mobile peripheral regions (*Wu and Kim, 1998*), being hydrophobic regions more exposed and flexible than in the native state *(Lala and Kaul, 1992; Kuwajima, 1996; Wu and Kim, 1998*). These regions are possibly the key region in the observed membrane-protein interaction as they may quickly interact with giant vesicles, inserting into the lipid bilayer. Since these regions are mainly located in the α-domain, their insertion in the phospholipidic bilayer could be responsible of the reduction of CD signal corresponding to α-helices.

Another possible explanation of modification in CD spectrum may also arise from changes in aromatic and sulfur side chains contribution in the far-UV region *(Krittanai and Johnson, 1997*). In particular, a study carried out on helical peptides showed that aromatic residues result in a positive/negative contribution to CD signal at about 222 nm *(Chakrabartty et al., 1993*). The contribution of aromatic residues to far-UV spectrum has been highlighted also in studies about thermal denaturation of equine lysozyme, in which changes at about 222 nm have been ascribed to a local rearrangement of the tertiary and secondary structures and to the transfer of some tryptophan residues to a more hydrophobic environment *(Morozova et al., 1991*). The observed change then may also be ascribed to a difference in the aromatic residues environment and in their packing.

A similar change in the far-UV spectrum was not observed in previous studies focused on α-La interaction with SUV or LUV *(Bañuelos and Muga, 1995; Agasøster et al., 2003; Chenal et al., 2005*). Far-UV spectra measured upon interaction between several α-La conformers and PC:PG vesicles were found to be similar in shape but higher in signal with respect to those measured in solution, indicating an increase in α-helical content *(Bañuelos and Muga, 1995*). It was also shown that the increase or decrease of the CD signal, depending on vesicle composition, are temperature dependent (*Agasøster et al., 2003*). Far-UV spectra typical of the molten globule state were observed upon protein addition to negative LUV or SUV *(Chenal et al., 2005*). Nevertheless, it has been highlighted the high sensitivity of α-La behavior to subtle changes in

physicochemical conditions ruling the combination of hydrophobic and electrostatic interactions at the basis of the interaction (*Chenal et al., 2005*). Our results are in line with α-La sensitivity to physicochemical properties of the environment, such as pH, vesicles composition, distribution of charge on membrane surface and membrane curvature.

Either modification in secondary structure or in aromatic packing discussed above are consistent with the idea of a protein insertion driven by hydrophobic interactions. In native α-La, aromatic residues form the two aromatic clusters located in the hydrophobic core of the protein (*Chrysina et al., 2000*). Although some of them are located in the molten globule core with a native-like packing (*Wu and Kim, 1998*), it is likely that the insertion of α-La in the lipidic bilayer results in a change in the environment of the aromatic residues located in the flexible regions and in a variation of their structural packing.

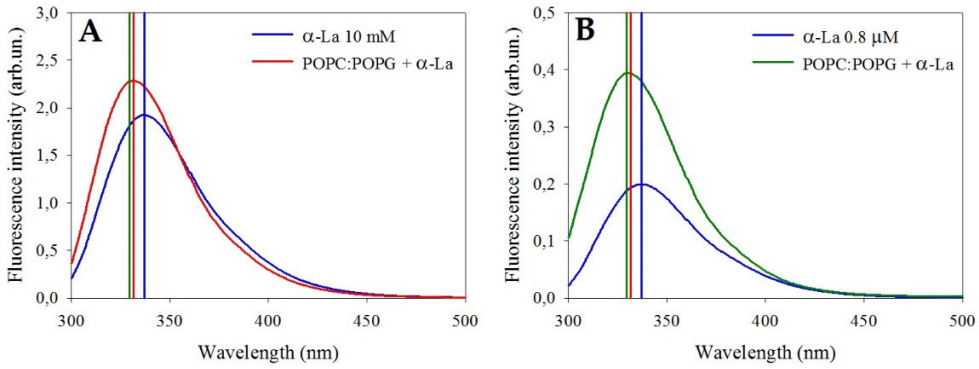

Figure 3.8 Intrinsic fluorescence spectra of α-La before and 24 hours after addition to giant vesicles. **(A)** L/P 20:1: 10 μM α-La at pH 2 (blue line) and after 24 hours from addition to POPC:POPG (red line). **(B)** L/P 250:1: 0.8 μM α-La at pH 2 (blue line) and after 24 hours from addition to POPC:POPG (dark green line). In each panel, straight lines indicate also the three maxima position, with the same color code. Spectra have been acquired in the range 285-500 nm, with λ_{exc} = 290, data interval 0.5 nm, excitation and emission bandwidth 2.5 nm and 5 nm respectively. All spectra have been acquired at room temperature.

To directly probe changes in aromatic environment occurring in the sample, we also analyzed α-La intrinsic fluorescence emission. In Figure 3.8 the intrinsic fluorescence under excitation at 290 nm of the 20:1 sample (red line, Figure 3.8A) and the 250:1 sample (green line, Figure 3.8B) together with the intrinsic fluorescence spectrum of pH 2 molten globule α-La (blue line, Figure 3.8A and 3.8B) are shown. The mayor contribution to α-La intrinsic fluorescence is due

to the four TRP residues located in different sites of the protein (*Brew, 2003*). Changes in intrinsic fluorescence emission spectra reflect variations in the TRP local environment. Moreover, TRP emission is strongly dependent on the polarity of the surrounding environment (*Lakowicz, 2006*). Intrinsic fluorescence of low pH α-La molten globule state has been previously characterized and it resulted red-shifted with respect to the one typical of the native state (*Lala and Kaul, 1992; Svensson et al., 1999; Chenal et al., 2005*), indicating the exposure of TRP residues. In particular, according to Lala et al. (*Lala and Kaul, 1992*), two of the four TRPs are exposed to the solvent.

Data in Figure 3.8 show an increased intensity and a blue-shift of the spectrum both for 20:1 and 250:1 samples (Figure 3.8A and 3.8B, straight lines), in different extents being dependent on L/P. It is well known that a blue-shift of TRP emission spectrum indicates a less polar environment and that both a decrease or increase of TRP emission quantum yield may occur upon conformational changes (*Souillac et al., 2003; Heegaard et al., 2005; Pedersen et al., 2006; Vetri et al., 2007b*). It is evident from Figure 3.8A and 3.8B, that, for both 20:1 and 250:1 samples, intrinsic fluorescence spectra are blue shifted, with a larger blue-shift at ratio 250:1 (dark green straight line). Moreover, the emission intensity shows an increase of a factor 1.15 for 20:1 sample and is nearly doubled for the 250:1 sample. Observed changes are consistent with the idea that molten globule hydrophobic regions insert into the phospholipidic bilayer. The blue shift reveals that tryptophan residues in the new formed structures are buried compared to their solvent exposure typical of the molten globule.

α-La intrinsic fluorescence has been largely used to characterize protein interaction with vesicles at acidic pH (*Bañuelos and Muga, 1995, 1996a; Agasøster et al., 2003; Chenal et al., 2005; Rødland et al., 2005*). Upon protein interaction with LUVs or SUVs at pH 4.5 an increase in fluorescence intensity occurred (*Bañuelos and Muga, 1995, 1996a; Agasøster et al., 2003; Rødland et al., 2005*), indicating the disappearance of protein tertiary interactions that quench the fluorescence in the native state (*Bañuelos and Muga, 1995*). The extent of fluorescence intensity increase was shown to be dependent on vesicle composition (*Rødland et al., 2005*). The intrinsic fluorescence maximum was found both red-shifted and blue-shifted depending on the considered α-La conformer (*Bañuelos and Muga, 1995, 1996a*), as well as on vesicle composition and temperature (*Agasøster et al., 2003*). It was shown that at pH 2, the fluorescence spectrum of DMPC-bound α-La was blue-shifted compared to the one of free

protein, indicating that TRP residues were less accessible in the membrane-bound case (*Cawthern et al., 1996*). Our results (Figure 3.8A and 3.8B) obtained at pH 2 where α-La is completely stabilized in the molten globule state, are in agreement with those obtained by Cawthern et al., being this another clue of the high sensitivity of α-La to subtle changes in sample physicochemical conditions. Again, it is possible to infer that the difference in the extent of spectral variation, in both maximum position and fluorescence intensity is due to the presence of different components of the spectrum. In the 250:1 sample the major component of the spectrum is attributable to protein interacting with membrane whilst, at opposite, in the 20:1 sample the mayor relative contribution can be attributed to protein not interacting with lipids. Intrinsic fluorescence measurements clearly suggest the insertion of α-La into the lipid bilayer, with the consequent formation of structures in which TRPs are buried compared to their solvent exposure in the molten globule state.

The presence of free unbound protein can be revealed by means of Raster Image Correlation Spectroscopy (RICS) analysis of fluorescence confocal images. Preliminary measurements show that when α-La is added to giant vesicles at L/P 20:1, an amount of free α-La is still present in the sample after the interaction with the lipid bilayer. When protein is added at low concentration, no diffusing unbound protein is observed. The presence of unbound protein in the samples, depending on its concentration, is still under investigation.

In order to deeply investigate the mechanisms at the basis of the observed phenomenon and whether changes in morphology are linked to membrane structural reorganization at the molecular level, a combination of both spectroscopy and microscopy methods has been used to analyze Laurdan dye emission. In particular, Laurdan dye is used to monitor variations in membrane phase properties occurring upon α-La addition to the sample. The averaged ergodic analysis of changes provided by spectroscopy measurements can be coupled with spatial information by means of two photon microscopy. Both in spectroscopy and microscopy experiments, the quantification of Laurdan spectrum changes is achieved by the Generalized Polarization (GP) values defined as described in the methods.

Laurdan dye is largely used in studies related to lipid bilayers fluidity (*Parasassi et al., 1990, 1997; Bagatolli and Gratton, 1999, 2000; Harris et al., 2002; Sanchez et al., 2010; Vetri et al., 2011; Owen et al., 2012; Sanchez et al., 2012; Golfetto et al., 2013; Amaro et al., 2017; Brewer et al., 2017*). Analysis of Laurdan fluorescence signal allows characterizing membrane structure

and investigating the variations following environmental changes, because of the sensitivity of its fluorescence emission spectrum to water penetration into the bilayer surface, which is related to lipid packing and membrane fluidity. Laurdan spectral properties allow determining the phospholipid phase state, distinguishing between a gel phase characterized by an emission spectrum centered on about 440 nm and a liquid crystalline phase characterized by an emission spectrum centered on about 490 nm (*Parasassi et al., 1998; Sanchez et al., 2007*). A change in the emission spectrum shape reflects a change in the phospholipid phase state. Laurdan GP has been introduced by Parasassi et al. *(Parasassi et al., 1990*) to quantify the variations in Laurdan fluorescence emission (see Chapter 2, Section 2.2.1). Theoretically the values for the GP function go from -1.0 to +1.0; however, experimentally they range from 0.6 to -0.3 both for pure lipids and for mixtures. Lower GP values (from 0.3 to -0.3) are ascribed to liquid phase while higher values (above 0.5) to membrane in the gel phase (*Sanchez et al., 2007*).

Changes in Laurdan fluorescence emission have been used to investigate the effects on LUV membranes caused by the addition of bovine α-La complexed with oleic acid (BLAOA), at different pHs (*Wen et al., 2013*). A shift of the spectrum toward lower wavelengths was observed after the addition of BLAOA to the vesicles, indicating that the lipid bilayer becomes more densely packed with lower solvent accessibility to Laurdan probe. Interestingly, it was highlighted that, at acidic pH, both BLAOA and bovine α-La have the same effect on membranes (*Wen et al., 2013*). Laurdan dye was also applied to monitor changes in GUV microdomains following sphingomyelinase (SMase) addition to DOPC/C16SM/cholesterol vesicles. By means of Laurdan GP analysis, it was shown that the initial coexistence of liquid-order (high GP value) and liquid-disordered (low GP value) regions within the liposome rapidly disappears upon SMase addition, with a resulting quite uniform Laurdan GP values distribution (*Taniguchi et al., 2006*). We used Laurdan GP to investigate the effect of α-synuclein addition to GVs, highlighting an increase in membrane rigidity for anionic membranes leading to liposomes burst (*Van Maarschalkerweerd et al., 2014*), and a decrease in membrane rigidity together with the formation of stable microdomains with different fluidity for zwitterionic membranes containing cholesterol (*Van Maarschalkerweerd et al., 2015*). Moreover, Laurdan GP has been used also to investigate the effects of interaction between proteins and live cells (*Vetri et al., 2011*).

Figure 3.9 shows Laurdan GP variation in cuvette experiments after α-La addition to POPC:POPG GVs at L/P 20:1 and 250:1. GP variation is calculated with respect to the value before protein addition. We report changes in a time scale comparable with the one shown in Figure 3.1A – 3.1F. We also report GP variations measured for Laurdan dye initially dispersed in 0.1 M NaCl, pH 2 solution, when 10 µM α-La is added using the same experimental protocol. This measurement is an important control indicating that Laurdan dye also interacts with protein in the same time scale inducing GP growth.

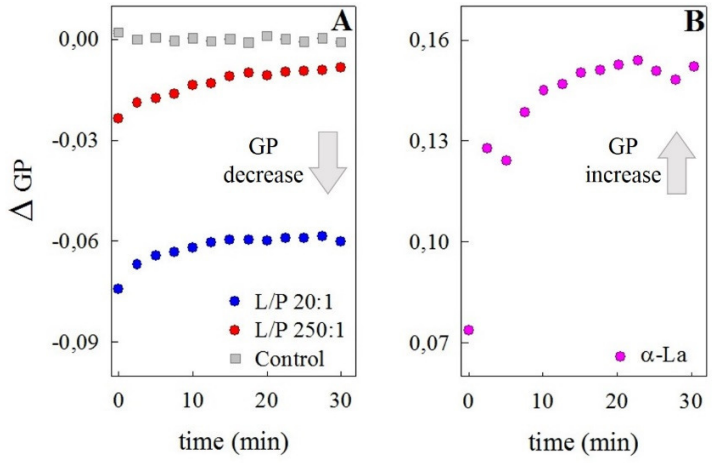

Figure 3.9 Laurdan GP variation as a function of time. **(A)** Laurdan GP variations after addition of α-La to POPC:POPG giant vesicles at L/P 20:1 (blue circles) and L/P 250:1 (red circles). GP variation after adding 0.1 M NaCl pH 2 is also showed as control measurement (grey squares). GP variation is calculated with respect to the value before protein addition. **(B)** Laurdan GP variation after adding 10 µM α-La to Laurdan in 0.1 M NaCl, pH 2.

As evident from Figure 3.9A, upon protein addition to vesicles, a sudden GP reduction is observed instantaneously (within experimental temporal resolution) and in the following 10 minutes the value of GP increases as a function of time toward a GP index equilibrium value. Furthermore, in addition to the changes in spectral shape taken in account by GP reduction, the measured Laurdan fluorescence intensity increases, being larger at increasing protein concentration (data not shown). After modifications occurring in the first minutes of the interaction process, GP value results to be slightly reduced at high L/P. The time evolution of

measured GP variations is the same when protein is added at both low (20:1) and high (250:1) L/P. However, the extent of overall GP variation clearly increases when protein concentration is raised (Figure 3.9A). In Figure 3.9B, changes in GP value monitored when 10 μM α-La is added to free Laurdan dye in aqueous solution (0.1 M NaCl, pH 2) are shown. When protein is added, the almost vanishing free Laurdan emission spectrum changes: an increase in fluorescence intensity (3 times the initial value) and a blue shift are observed, indicating changes in the environment of the dye. Interestingly, GP index growth obtained in the absence of lipid vesicles parallels GP growth in the presence of lipids toward a final value lower than the one typical of Laurdan in liposomes (0.55). The obtained GP value for liposomes is typical of the gel-phase (*Sanchez et al., 2007*).

Data reported in Figure 3.9 indicate that the observed changes in GP may result from both changes in lipid packing and α-La-Laurdan interaction. The variation in GP index when α-La is added to free Laurdan dye is about four times larger than the one observed when protein is added to stained liposomes, this being reasonable as Laurdan dye is initially in a completely unfavorable environment. The GP reduction observed for Laurdan in lipid membranes and reported in Figure 3.9A is likely to reflect change in membrane fluidity, indicating an initial change in lipid organization to a more disordered phase accessible to solvent, occurring immediately after protein addition to the sample. The following growth may be ascribed to further changes in membrane structure toward a more ordered phase, similar to the initial one. However, data in Figure 3.9B suggest that a direct interaction between Laurdan and α-La occurs, leading to the observed GP growth in the first 10 minutes. We note that similar changes were not observed in analogous experiments (*Van Maarschalkerweerd et al., 2014, 2015*). It is possible to infer that GP changes in Figure 3.9A are due to a redistribution of the dye on both protein and vesicles. Data in Figure 3.1 and 3.9 indicate that, within few minutes after its addition to GV samples, α-La accumulates at the membrane surface inducing modification in lipid organization, possibly penetrating the bilayer and inducing significant modification on liposome structures.

In order to obtain detailed spatial insights on the observed phenomenon, α-La-membrane interaction process was further investigated also by means of two-photon microscopy measurements of Laurdan fluorescence emission. In Figure 3.10, the comparison between representative measurements on Laurdan stained POPC:POPG liposomes at acidic pH before

and 24 hours after the addition of α-La at L/P 20:1 and 250:1 is shown. Data acquired after 24 hours from protein addition are representative of micrometric structures present in the sample at reached equilibrium. 256x256 pixels intensity images (Figure 3.10A – 3.10C) are used to simply show the morphology. GP maps at pixel resolution (Figure 3.10D – 3.10F) were obtained by image analysis of the 256x256 images. In the GP maps, the GP value in each pixel of the image is reported, following a color scale from blue (GP = -1) to red (GP = +1). For each image, it is possible to build the GP histogram where the GP values measured in each pixel of the image are taken in account. From the histogram, the average GP value and the standard deviation of all the pixels in the GP image can be obtained. The histograms obtained from the analysis of data in panel B (L/P 20:1) and in panel C (L/P 250:1) are reported in Figure 3.10G in red and blue color, the histogram obtained for untreated sample is reported in green as a reference.

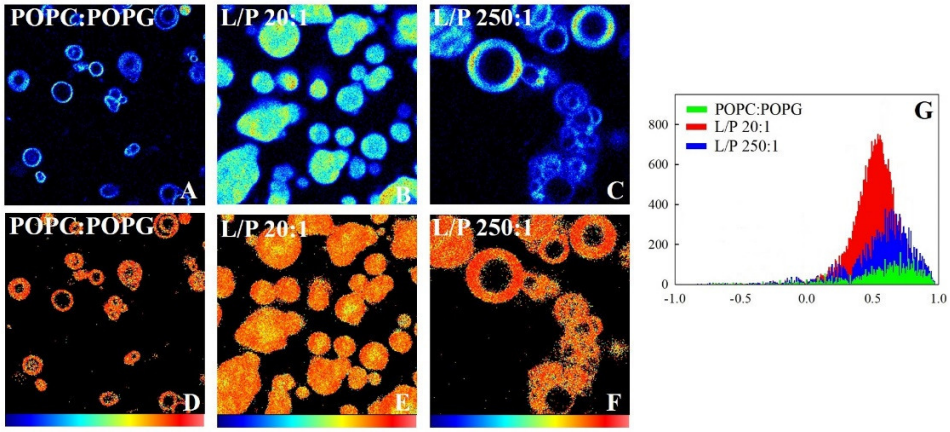

Figure 3.10 GP analysis of two-photon microscopy representative images of POPC:POPG giant vesicles before and after 24 hours from α-La addition. Images have been acquired collecting Laurdan Fluorescence in the range 430-450 nm and 485-505 nm, with λ_{exc} = 780 nm. **(A, B, C)** 256x256 pixels intensity images of giant vesicles **(A)** before and after 24 hours from protein addition at **(B)** L/P 20:1 (10 µM α-La) and **(C)** L/P 250:1 (0.8 µM α-La). Images size is **(A)** 70.29 µm x 70.29 µm and **(B, C)** 30.72 µm x 30.72 µm. **(D, E, F)** 256x256 pixels GP maps, indicating GP value in each pixel, corresponding to the intensity images: **(D)** before, **(E)** at L/P 20:1 and **(F)** at L/P 250:1. Color bar indicates the value of GP in each pixel. GP values range from -1 (blue) to +1 (red). **(G)** Histograms of GP values corresponding to GP maps, indicating the distribution of GP values in the pixels.

Two-photon microscopy images in Figure 3.10A – 3.10C show the clear change in morphology when α-La is added to liposomes at L/P 20:1 and L/P 250:l. In particular, larger morphology changes in vesicles are observed in samples with higher protein content. In the 20:1 sample, a

homogeneous distribution of roundish structures is observed. In the 250:1 sample, structures with more heterogeneous morphology are found: some of them have the same morphology of liposomes before protein addition, other are clustered and "curly". This kind of structures were not found in the initial sample (Figure 3.10A). As can be seen in Figure 3.10, in line with spectroscopy measurement, both 20:1 and 250:1 samples show an increase in fluorescence intensity, being the one in 20:1 sample (Figure 3.10B) definitively higher than the one measured in 250:1 sample (Figure 3.10C).

GP maps in Figure 3.10D – 3.10F, show that despite of differences in shape, size or fluorescence intensity, in all the samples the GP distribution is uniform, with a slight spatial inhomogeneity in 20:1 samples. The mean value of GP for each map is around 0.55 for initial liposomes, 0.50 for 20:1 sample and 0.54 for 250:1 sample, all of these values being compatible with the lipid bilayers in the gel phase in the whole liposomes. As expected, the decrease in the average GP value is more evident at ratio 20:1, due to the presence of a greater amount of α-La interacting with lipids. After α-La addition, the width of the histogram remains the same, with a little shift of the average GP toward small values, more evident at L/P 20:1 (Figure 3.10G). Overall, results are in good agreement with cuvette measurements. If cuvette measurements provide information on average sample changes, microscopy measurements result in local and detailed information. In addition to information obtained by means of cuvette experiments, two-photon microscopy measurements provide information on the spatial distribution of Laurdan GP. In particular, at high protein concentration, it is evident from Figure 3.10E the inhomogeneity in spatial GP distribution, which likely reflects an inhomogeneity in protein distribution in the final structures. Due to the interaction between Laurdan and α-La (Figure 3.9B), the areas with a lower GP value (yellow pixels) reflect increased fluidity in the membrane.

3.2 Conclusions

In this Chapter, the interaction between α-La and phospholipidic bilayer has been investigated. After addition of α-La molten globule to POPC:POPG giant vesicles, protein locates on accessible liposome surfaces and causes a quick destabilization of lipid bilayer, modifying vesicles morphology. The extent of destabilization is dependent on protein concentration. Larger morphology changes are observed in samples with higher protein content. The change in

morphology is likely due to a fast initial adsorption followed by protein insertion into the membrane. Upon α-La addition to giant vesicles, the combination of electrostatic interactions with the polar heads of lipids and hydrophobic interactions with the lipid chains results in a quick adsorption of α-La to lipid bilayer. Above a critical surface density, the insertion into the lipid bilayer occurs, driven mainly by hydrophobic interactions. Upon interaction, a homogeneous distribution of roundish structures is observed at high protein concentration, whereas structures with more heterogeneous morphology are found at low protein concentration. Colocalization experiments indicate that final structures are composed of both lipids and protein. Simultaneously, changes in membrane fluidity occur. Laurdan GP analysis, performed with both spectroscopy and microscopy techniques, reveals that, upon interaction, final GP value is slightly lower than the initial one, indicating a different lipid organization toward a more disordered lipid phase. Overall, due to an interaction between Laurdan and α-La, GP variations are ascribable to a redistribution of the dye on both protein and vesicles. In addition, microscopy measurements highlight an inhomogeneity in GP spatial distribution, which is related to a heterogeneous protein distribution on liposome surface. In final structures, depending protein concentration, α-La is found to experience different local environments, as showed by FLIM measurements. Importantly, it is possible to distinguish between adsorption and insertion state. The interaction between α-La and giant vesicles results in a change of protein secondary and tertiary structure. Changes in far-UV spectra indicate an increase of β-sheet and a decrease of α-helix structures as well as a change in aromatic residues packing. Results are consistent with the idea of a protein insertion driven mainly by hydrophobic interactions.

Chapter 4

Multiple pathways in α-lactalbumin amyloid formation

Amyloid fibrils are ordered aggregates with a highly organized H-bond pattern, representing the most stable state that proteins can adopt (*Baldwin et al., 2011*). Protein aggregation is a fundamental topic in recent biomedical and biotechnological research, since several human diseases like Parkinson's and Alzheimer's disease or type-II diabetes are related to amyloid fibrils and their deposition in human organs and tissues (*Stefani, 2004; Uversky and Fink, 2004; Ross and Poirier, 2005; Chiti and Dobson, 2006, 2017; Merlini et al., 2011; Knowles et al., 2014; Hartl, 2017; Ke et al., 2017*). Moreover, it is nowadays accepted the interconnectivity between amyloid formation and membrane disruption (*Butterfield and Lashuel, 2010*) and it has been highlighted that membrane can be destabilized by both pathogenic proteins and proteins not related to diseases (*Stefani, 2004; Butterfield and Lashuel, 2010; Vetri et al., 2011*).

In this work, focused on the molecular mechanisms underlying the interaction between proteins and membrane, α-La has been used as model protein. In order to investigate the interaction of model membranes with protein aggregates, this Chapter is focused on the experimental study of thermally induced amyloid fibril formation of α-La at pH 2, when the protein is in the molten globule state (*Kuwajima, 1996*). As for the multitechnique approach used in Chapter 3 to investigate the interaction between α-La and giant vesicles, a combination of spectroscopy and microscopy techniques has been used to analyze the mechanisms underlying α-La aggregation. The supramolecular assembly of α-La has been observed as a function of time by means of elastic light scattering and *in situ* Thioflavin T (ThT) fluorescence measurements in different

conditions. This allows to investigate the mechanisms underlying the aggregation process, also revealing the amyloid nature of formed supramolecular structures. With the aim of probing the secondary structure and morphology, final aggregates were characterized by FTIR absorption spectroscopy and by confocal microscopy measurements. In order to induce α-La aggregation, sample has been incubated in different conditions in presence of stirring. The characterization of the aggregation process as a function of the stirring speed allows to further investigate α-La fibrillation and to highlight the mechanisms at the basis of amyloid formation.

4.1 Results and discussion

Effect of the temperature on α-La aggregation. Figure 4.1 shows α-La aggregation process as a function of the temperature (range 33°C – 70°C) at constant stirring speed of 540 rpm and α-La concentration of 3.75 mg/ml. Temporal evolution of Rayleigh scattering signal and Thioflavin T (ThT) fluorescence emission intensity, normalized to the value at the plateau, are presented in Figure 4.1A and 4.1B, respectively. ThT kinetics present an almost immediate growth of the signal without a significant lag time before reaching a final plateau. Simultaneous measurements of the Rayleigh scattering signals show an analogous trend as the ones for ThT and the two intensity values linearly correlate during the entire duration of the experiments, independently of the temperature of incubation (Figure 4.1C). These data show that, in the conditions here investigated, the self-assembly process likely leads to the sole formation of amyloid-like species, without any significant formation of amorphous aggregates. Indeed the latter would have produced a deviation from linearity in Figure 4.1C.

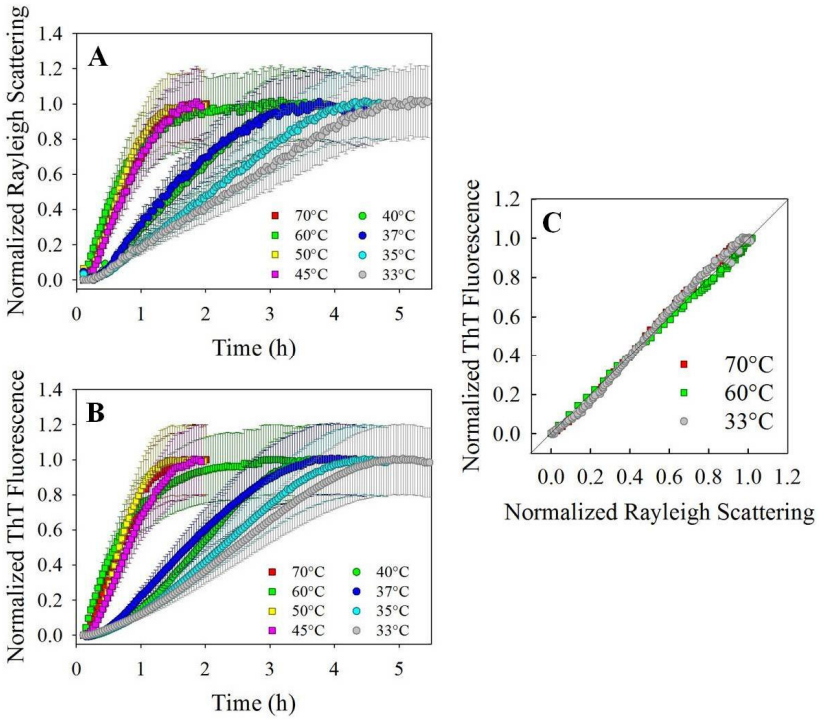

Figure 4.1 (A) Normalized Rayleigh Scattering and **(B)** Normalized ThT fluorescence emission as a function of time during the fibrillation of 3.75 mg/ml α-La sample, at different temperatures ranging from 33°C to 70°C, at stirring speed 540 rpm. **(A)** Rayleigh scattering is measured at the excitation wavelength λ_{exc}= 440 nm. **(B)** ThT fluorescence is measured at 480 nm, with λ_{exc}= 440 nm. The data in the two panels are obtained in a single experiment and are normalized to the plateau value. **(C)** Normalized ThT fluorescence intensity (λ_{exc}= 440 nm, λ_{em}= 480 nm) as a function of the normalized Rayleigh scattering peak intensity (λ_{exc}= 440 nm, λ_{em}= 440 nm). The solid line is a guide for eyes.

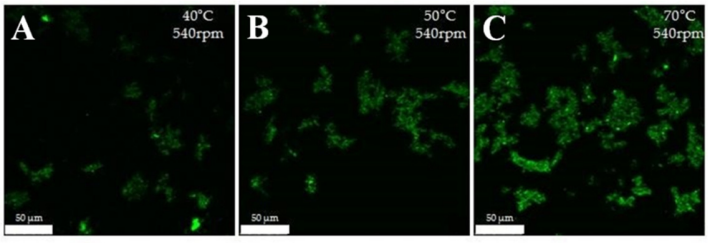

Figure 4.2. Confocal microscopy images representative of the aggregates obtained after **(A)** 4 hours of incubation at 40°C, and 2 hours of incubation at **(B)** 50°C and **(C)** 70°C. Images have been acquired with a 1024 x 1024 pixel resolution. Excitation wavelength was set at 458 nm and emission detected in the range 478-600 nm. Images show that an increase of temperature results in an increase in the number of aggregates. Scale bar is 50 µm.

Confocal fluorescence microscopy measurements confirm the presence of ThT-positive aggregates species. In Figure 4.2, representative images of aggregates obtained from α-La samples after incubation at 540 rpm at different temperatures (40°C, 50°C and 70°C) are shown. Measurements reveal that the aggregates in the sample interact with the dye and that the size of supramolecular aggregates is highly heterogeneous for the investigated samples. Clusters of highly fluorescent aggregates are evident, whose number increases at increasing temperature, without any significant difference in the morphology.

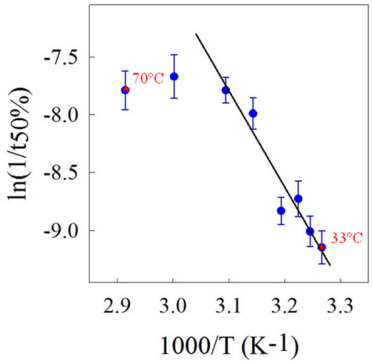

Figure 4.3 Arrhenius plot relative to data in Figure 4.1B. Solid line indicates the linear fit of the data in the range 33°C – 50°C. Rate constants were estimated as the inverse of the time to reach 50% of the kinetics.

Notwithstanding the similarity in terms of kinetics profile and final microscopic morphology, analysis of the energy barrier related to the process reveals the presence of two distinct temperature regimes. Figure 4.3 shows the Arrhenius plot for the process. We use $1/t_{50\%}$ (see Chapter 2, Paragraph 2.3.2) as a heuristic estimation of the rate constants. This choice allows us to not hypothesize any molecular model to fit the data and extrapolate the rate constants. Figure 4.3 clearly presents a region of linearity in the range 33°C - 50°C, while for T>50°C we observe an almost constant value for the aggregation rate. The linear region indicates activation energy of 70 KJ/mol. The non-linearity can be attributed to several factors, such as an intrinsically temperature-dependent contribution to the activation energy or a competition between different pathways leading to a different rate-limiting step as temperature changes (*Wang and Roberts, 2013*). We have previously observed a similar trend as the one in Figure 4.3 in the case of the aggregation process of a flexible form of Concanavalin A (*Vetri et al., 2013*). In that case we highlighted the existence of different interconnected mechanisms ruling the process and being

selectively activated by modulating the environmental conditions. Indeed, deviations from Arrhenius behavior are related to differences in the heat capacity between the native state and the transient states within the process (*Pedersen et al., 2006*). Such variability can be interpreted as changes in the protein exposed surface area accompanying the kinetic transition. Differences in the exposed areas determine different aggregation pathways (*Hulett, 1964; Pedersen et al., 2006*).

Effect of α-La concentration on the aggregation process. Data presented in the previous section suggest the presence of different aggregation pathways that can be activated by the temperature. With this idea in mind, we analyze the process as a function of the protein concentration at 70°C (within the region deviating from linearity) and 33°C (within the Arrhenius range).

At 70°C the kinetics profile resemble the ones show in Figure 4.1A and 4.1B and the α-La concentration affects both the rate of the process as well as the ThT final fluorescence value (FFV, see Chapter 2, Paragraph 2.3.2)

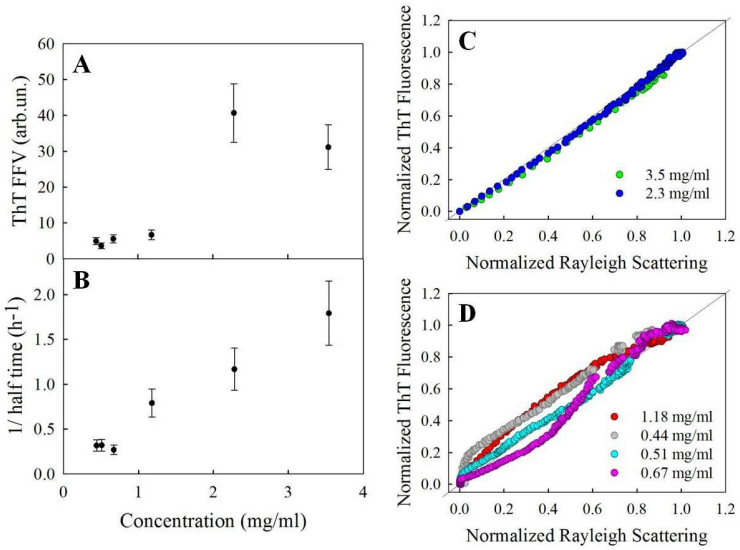

Figure 4.4 (A) ThT fluorescence final value (FFV) and **(B)** reciprocal of the time required to reach 50% of the ThT as a function of concentration, during the fibrillation of α-La sample at different concentrations ranging from 0.44 mg/ml to 3.54 mg/ml, incubated at 70°C, at stirring speed 540 rpm. **(C, D)** Normalized ThT fluorescence intensity (λ_{exc}= 440 nm, λ_{em}= 480 nm) as a function of the normalized Rayleigh scattering peak intensity (λ_{exc}= 440 nm, λ_{em}= 440 nm) for the **(C)** high concentration and **(D)** low concentration α-La samples. The solid line is a guide for eyes.

Figure 4.4A shows indeed that FFV does not significantly change for concentrations below 1.5 mg/ml, while an 10-fold increase is detected at 2.3 and 3.5 mg/m. $1/t_{50\%}$ as a function of the α-La concentration is reported in Figure 4.4B and indicates similar value for concentration ≤ 1 mg/ml, while above 1 mg/ml, $1/t_{50\%}$ linearly increases at increasing concentration. Correlation between ThT and Rayleigh signals is only obtained for concentration ≥ 2.3 mg/ml (Figure 4.4C). Below this concentration significant deviations from linearity are observed (Figure 4.4D). This can be due to the different sensitivity of the two signals towards the conformational changes and formation of early aggregates. Indeed, ThT can also increase its quantum yield in presence of substantial conformational changes of the protein that make available binding site for the dye (*LeVine III, 1997*). This will determine an increase in the ThT fluorescence value without significantly affecting the scattering signal. This is the case for the samples at 1.18, 0.44 and 0.51 mg/ml. In the very early stage of the kinetics (< 10 min) a slightly more pronounced increase in the ThT compared to scattering is indeed observed (Figure 4.4D). Importantly, formation of amyloid ThT-positive aggregates too small to be revealed by scattering could in principle contribute to the observed effect. On the contrary, for the sample at 0.67 mg/ml, a rapid increase in the scattering signal is detected, while only a slight increase in ThT fluorescence is observed. This stems for the formation of ThT-negative amorphous aggregates in the early phases of the process. After such early phases, different mechanisms can take place, resulting in different rate of increase of ThT and scattering signal. From the data in Figure 4.4C and 4.4D a clear trend can not be extrapolated. However, our data show that the processes at concentrations ≤ 1.18 mg/ml are governed by different aggregation pathways, in which the formation of amorphous aggregates and substantial conformational changes can have a significant role. At concentrations ≥ 2.3 mg/ml, the process likely proceeds through conformational changes which occur in parallel with supramolecular aggregation, determining the correlation between ThT and scattering signal.

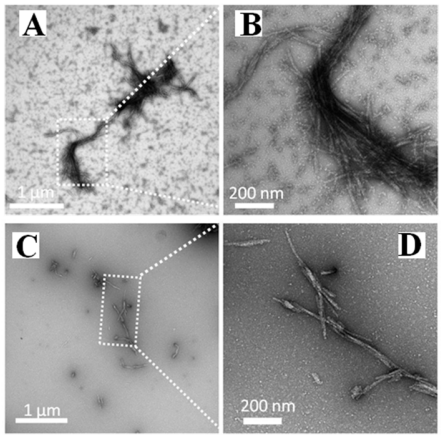

Figure 4.5 Transmission electron microscopy (TEM) images of the α-La samples at **(A, B)** 3.75 mg/ml and **(C, D)** 0.67 mg/ml after incubation at 70°C. Scale bar is **(A, C)** 1 µm and **(B, D)** 200 nm.

To evaluate differences in aggregates morphology at nanometric scale, we imaged final aggregates by means of transmission electron microscopy (TEM). Representative images shown in Figure 4.5 allow us to compare aggregates obtained from α-La samples at 3.75 mg/ml and 0.67 mg/ml. In both cases we detect the presence of amyloid-like fibrils. While at low concentration isolated single filaments represent the main population, a massive clustering of fibrils is detected at the high concentration. According to previous studies, the presence of massive clustering of the fibrils is indicative of the occurrence of surface-driven secondary nucleation pathways (*Ferrone, 1999*). Via such mechanisms, the surface of already formed fibrils can catalyze the conformational changes and self-assembly of nearby protein molecules onto the fibril surface. This activates a self-propagating mechanism leading to the observed macroscopic clustering. Such mechanism is highly dependent on the initial concentration of protein. At very low concentration these processes are unlikely (*Ferrone, 1999*), and the formation of single, well distinct, fibrils should be expected, as verified by the TEM analysis.
The existence of different coexisting mechanisms ruling α-La fibril formation is evident also analyzing the aggregation process at 33°C.

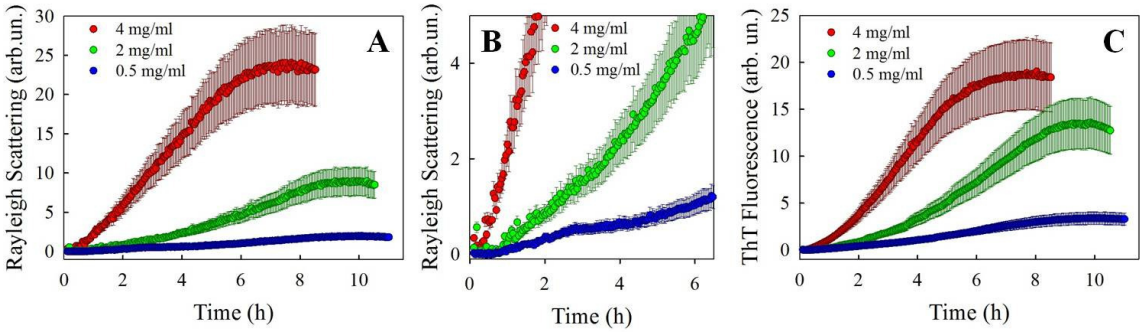

Figure 4.6 (A) Rayleigh Scattering and **(C)** ThT fluorescence emission as a function of time during isothermal incubation at 33°C for α-La samples at different concentrations ranging from 0.5 mg/ml to 4 mg/ml, at stirring speed 540 rpm. **(A)** Rayleigh scattering is measured at the excitation wavelength λ_{exc}= 440 nm. **(C)** ThT fluorescence intensity is measured at 480 nm, with λ_{exc}= 440 nm. The data in the two panels were obtained in a single experiment. **(B)** Rayleigh Scattering peak intensity as a function of time during the first 6 hours.

Figure 4.6 shows Rayleigh scattering peak intensity measured at 440 nm (Figure 4.6A) and ThT fluorescence emission intensity measured at 480 nm as a function of time (Figure 4.6C), for three α-La samples incubated at 33°C, with concentration ranging from 0.5 mg/ml to 4 mg/ml. Scattering signal as well as ThT fluorescence emission increase with increasing protein concentration. Figure 4.6B shows Rayleigh scattering during the first 6 hours, with a different scale on Rayleigh scattering axis. The profiles of Rayleigh Scattering peak intensity obtained at low concentrations clearly reveal the coexistence of different mechanisms in α-La supramolecular assembly. In the early stages a slightly more pronounced increase in the scattering compared to the ThT is observed, suggesting that at low temperature the formation of ThT-negative aggregate (amorphous aggregates) is initially favored before a significant occurrence of amyloid-like species is observed. This is clearly highlighted by Figure 4.7A and 4.7B, showing that different mechanisms take place during α-La supramolecular assembly, depending on protein concentration.

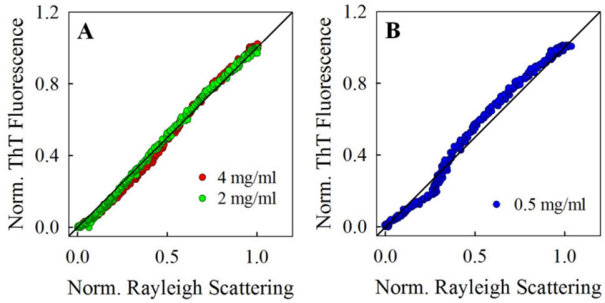

Figure 4.7 Normalized ThT fluorescence intensity (λ_{exc}= 440 nm, λ_{em}= 480 nm) as a function of the normalized Rayleigh scattering peak intensity (λ_{exc}= 440 nm, λ_{em}= 440 nm) for the **(A)** high concentration and **(B)** low concentration α-La samples. The solid line is a guide for eyes.

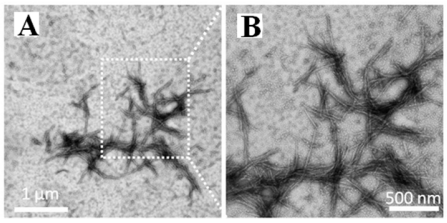

Figure 4.8 Transmission electron microscopy (TEM) images of the α-La samples at 3.75 mg/ml after incubation at 33°C. Scale bar is **(A)** 1µm and **(B)** 500 nm.

As observed for the aggregation process induced at 70°C (Figure 4.4C and 4.4E), different aggregation pathways clearly occur at low concentration (Figure 4.7B), leading to the formation of amorphous aggregates in the early phases of the assembly. At protein concentrations ≥ 2 mg/ml (Figure 4.7A) correlation between ThT and scattering signal is obtained during each phase of the process. In Figure 4.8 representative TEM images of α-La sample at 3.75 mg/ml after incubation at 33°C are shown. It is evident the presence of clusters of amyloid-like fibrils, which indicate that surface-driven secondary nucleation pathways occur (*Ferrone, 1999*).

Stirring reveals a pronounced spatial heterogeneity. Data in the previous section point towards a series of interconnected mechanisms taking place during the α-La aggregation process dependent of the physico-chemical conditions in which the reaction is induced. Our data indicate a main role of secondary nucleation pathways in determining both the kinetics progression and

final morphology of the aggregates at nm-level. To further investigate this, we performed a study as a function of the stirring speed. We hypothesize that if surface-driven mechanisms determine the course of the aggregation, stirring will greatly affect it *(Cohen et al., 2013; Lee et al., 2007; Serio et al., 2000*), altering also the spatial homogeneity of the process (*Lee et al., 2007; Serio et al., 2000*). Figure 4.9 shows the thermally-induced (T=70°C) aggregation kinetics of a sample at 3.75 mg/ml of α-La, at different stirring speed (60 rpm, 180 rpm, 360 rpm, 540 rpm, 800 rpm). Figure 4.9A and 4.9B show, as a function of time, Rayleigh scattering peak intensity measured at 440 nm and ThT fluorescence intensity measured at 480 nm, respectively.

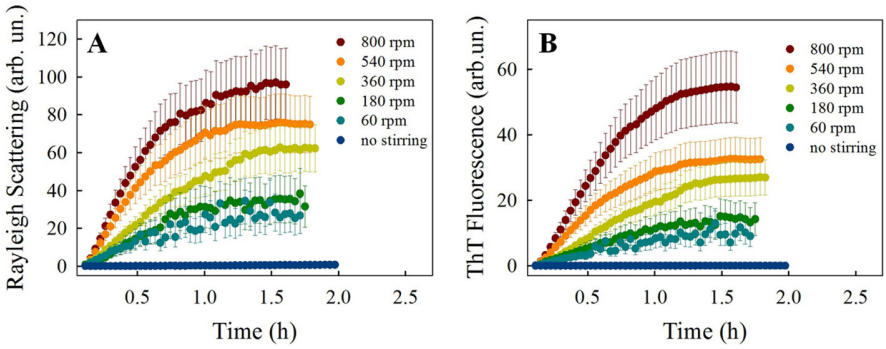

Figure 4.9 (A) Rayleigh Scattering and **(B)** ThT fluorescence emission as a function of time during isothermal incubation at 70°C for 3.75 mg/ml α-La sample at different stirring speed, ranging from 0 rpm to 800 rpm. **(A)** Rayleigh scattering is measured at the excitation wavelength λ_{exc}= 440 nm. **(B)** ThT fluorescence intensity is measured at 480 nm, with λ_{exc}= 440 nm. The data in the two panels were obtained in a single experiment.

In quiescent conditions no aggregation is observed, while at increasing stirring speed we observe an increasing size of the species in solution that proceeds in parallel with a ThT fluorescence increase, as also verified by the linear correlation of the two signals (not shown). This is in line with what we have previously observed and suggests a process that involve a simultaneous change of conformation of the protein molecules and a self-assembly into species of higher molecular weight.

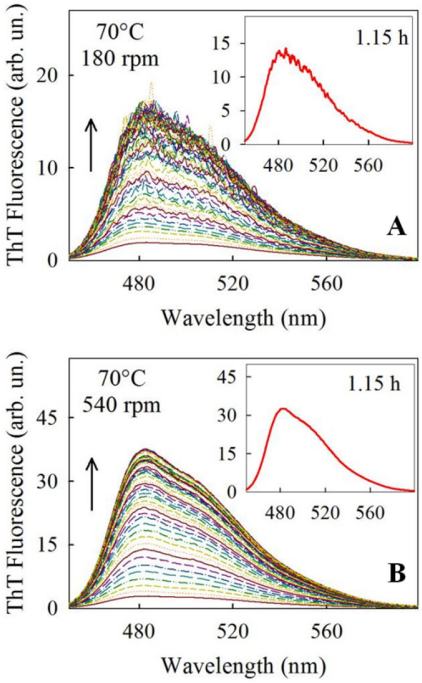

Figure 4.10 ThT fluorescence spectra for 3.75 mg/ml α-La sample, during isothermal incubation at 70°C, at stirring speed **(A)** 180 rpm and **(B)** 540 rpm. Inset shows ThT fluorescence spectra after 1,15 h.

Further insights can be obtained by the analysis of the full fluorescence spectra. Figure 4.10A shows the temporal evolution of the ThT fluorescence spectra during the aggregation process at 180 rpm, at 70°C. Spectral distortions during the aggregation kinetics can be detected at this stirring speed as well as at 60 rpm (data not shown), while they are absent at higher stirring speeds (Figure 4.10B). Spectral distortion during aggregation process has been previously reported for insulin at the beginning of the growth phase of fibrils in a low protein concentration regime (< 1mg/ml). This has been attributed to the early aggregates species occurring in solution and diffusing within the whole volume of the sample (*Librizzi et al., 2007; Foderà et al., 2009*). Such diffusion in/out of the scattering volume generates in turn the observed spectral distortions. This has pointed out a highly spatially heterogeneous formation of the early aggregates within the volume, probably triggering secondary nucleation events and giving rise to the abrupt growth of both ThT and scattering signals (*Librizzi et al., 2007; Foderà et al., 2009*). Interestingly, for processes where only primary nucleation is observed, intensity fluctuations were not revealed *(Vetri et al., 2007b*), proving an intimate connection between spatial

heterogeneity and secondary nucleation mechanisms. Indeed, the growth of aggregates because of the secondary pathways is spatially localized in the sample, and depends on the formation of early aggregates, which can be considered a stochastic event. ThT fluorescence spectra showed in Figure 4.10 suggest, therefore, that α-La aggregation process is characterized by a spatial heterogeneity, which is modulated by stirring. At high stirring speeds, early aggregates quickly move in/out the observation volume, so that aggregates on average appear to be homogeneously distributed. On the contrary, at low stirring speeds, aggregates slowly move in/out the observation volume, underlying the sample spatial heterogeneity. When the excitation beam interacts with large ThT-positive aggregates, sudden increases of scattering and ThT emission intensity are observed. This would determine the observed spectral distortions. Moreover, we cannot in principle exclude that stirring can also affect the stability of the formed supramolecular structures. In particular, fragmentation of larger aggregates is likely to be more effective in presence of pronounced stirring (*Cohen et al., 2013*). Therefore, at higher stirring speeds, we can have two simultaneous effects: aggregates are fragmented, i.e. reduced in size, and, due the high flow in solutions, they quickly move in/out the observation volume. These two concomitant effects lead to a complete absence of distortions. Importantly, spectral distortions are nearly absent at low temperature. Indeed, at constant stirring speed, spectral distortions observed in ThT fluorescence emission spectra, which are evident from about 15 minutes after incubation at 70°C, take place at longer times with decreasing temperatures and are almost absent at 40°C, as shown in Figure 4.11. This also suggests that different aggregation pathways occur during α-La fibrillation, depending on temperature.

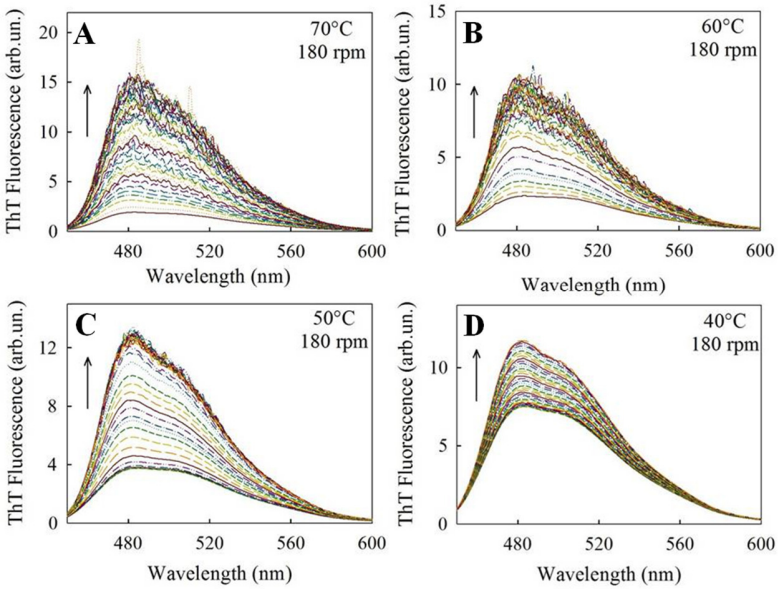

Figure 4.11 ThT fluorescence emission spectra for 3.75 mg/ml α-La samples, during incubation at 180 rpm at temperature **(A)** 70°C, **(B)** 60°C, **(C)** 50°C, **(D)** 40°C.

Data above reported suggest that the obtained kinetics are typical of a nucleated process, which include primary and secondary pathways (*Cohen et al., 2012*). As evident from Figure 4.9A and 4.9B, in absence of agitation there is no significant increase in Rayleigh scattering peak intensity or ThT fluorescence intensity over the whole observation time. On the contrary, in presence of stirring the aggregation process rapidly occurs and aggregates of amyloid-like origin are quickly formed, as indicated by the data shown in Figure 4.9B. The temporal features of the process are independent of the stirring speed. Specifically, amyloid aggregates form in 1.5 - 2 h and the normalization of the curve shows that the profiles overlap (Figure 4.12).

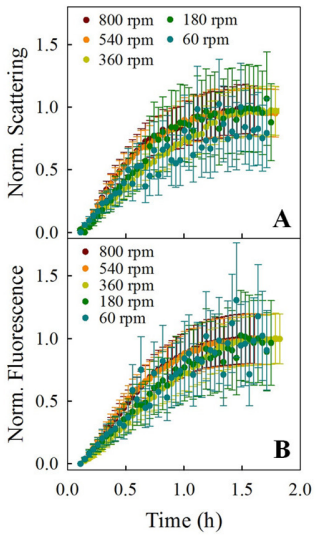

Figure 4.12 (A) Normalized Rayleigh Scattering and **(B)** Normalized ThT Fluorescence emission show the kinetics showed in Figure 4.9A and 4.9B, with stirring speed ranging from 60 rpm to 800 rpm, scaled for the plateau value.

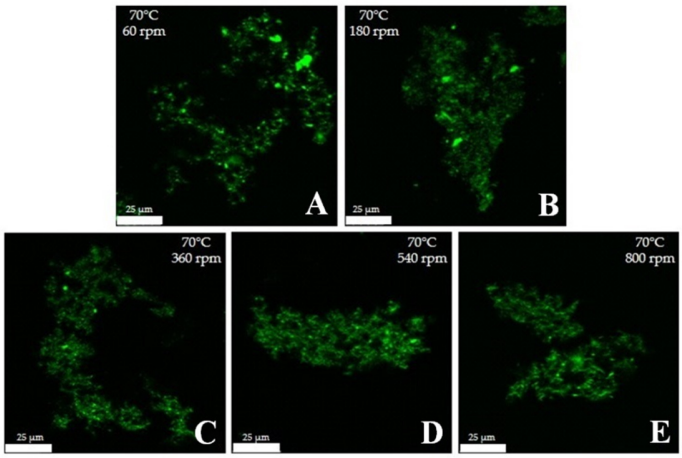

Figure 4.13 Morphology of aggregate states. Confocal microscopy images representative of aggregates obtained from 3.75 mg/ml α-La samples, after incubation at 70°C at different stirring speed, show that the aggregates have similar morphology. Images obtained at **(A)** 60 rpm, **(B)** 180 rpm **(C)** 360 rpm, **(D)** 540 rpm, **(E)** 800 rpm. For all images, the excitation wavelength was set at 458 nm and the emission detected in the range 478-600 nm. All images have been acquired with a 1024 x 1024 pixel resolution. Scale bar is 25 µm.

Similarly, micrometric morphologies do not depend on the stirring speed. In Figure 4.13, representative images of aggregates obtained from α-La samples after incubation at 70°C, at different stirring speed, are shown. Amyloid aggregates in the different samples are characterized by a similar morphology. It is possible to infer that the highly fluorescent clusters evident in Figure 4.13 are organized in a network of elongated aggregated materials resembling small fibrils. Moreover, it is possible to identify areas in which ThT fluorescence emission is more intense, particularly for the aggregates obtained al low stirring speed. This could also explain the abrupt growth of ThT fluorescence emission showed in Figure 4.10, present at low stirring speed and totally absent at high stirring speed. In the latter case, ThT fluorescence emission appears to be more homogeneously distributed. Overall, within the experimental resolution, confocal fluorescence microscopy measurements show no significant difference in aggregate morphology. Although at low concentration the lack of correlation between ThT fluorescence emission and scattering peak intensity clearly underlines the existence of different mechanism ruling the aggregation, also in this case final aggregates resemble clusters organized in a network of amyloid fibrils (data not shown).

In order to highlight differences in the secondary structure of amyloid aggregates obtained at different stirring speed and different temperatures, FTIR measurements have been performed.

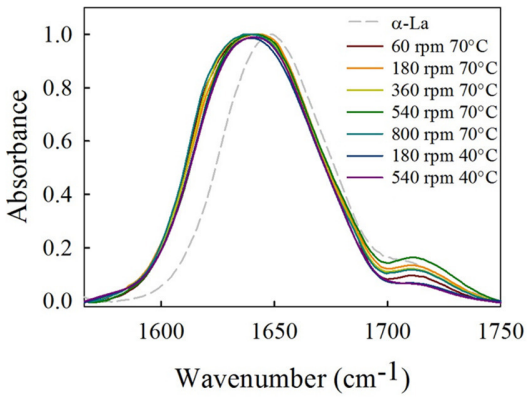

Figure 4.14 Normalized FTIR absorption spectra (Amide I') of α-La samples at pH 2, before incubation (gray dashed line) and after incubation at 70°C and 40°C, at different stirring speeds (colored lines).

In Figure 4.14, normalized FTIR absorption spectra of α-La aggregates formed at different stirring speed and at two different temperature (40°C and 70°C) are shown (colored lines). The

spectrum of molten globule α-La is also reported (gray dashed line). All spectra show a small peak at around 1712 cm^{-1}, due the exposure of Glu and Asp residues to an acidic environment (*Barth, 2000, 2007*). As previously observed, in the molten globule state the protein is deprived of the native tertiary structure but retains the native-like secondary structure (*Kuwajima, 1996*). α-La secondary structure, composed by a large α-helical domain and a small β-sheet domain (*Brew, 2003*), is responsible for the main peak centered at about 1650 cm^{-1}, attributed to α-helical content (*Militello et al., 2004*). In the spectrum of the aggregate state it is evident the growth of a peak at about 1620 cm^{-1}, typically attributed to intermolecular β-sheet structures found in amyloid structure (*Yan et al., 2006; Andersen et al., 2010*) and completely absent in protein spectrum before the aggregation process. Overall, FTIR measurements performed on α-La aggregates obtained at different experimental conditions do not show evident differences in secondary structure. Slight differences between spectra in Figure 4.14 are most likely ascribable to sample heterogeneity, typical of nucleated processes.

Under the used environmental conditions, i.e. acidic pH, α-La is in the molten globule state (*Kuwajima, 1996*), partially denatured but characterized by a high stability. Intrinsic fluorescence measurements show that stirring alone does not cause additional conformational changes, at least not at the considered stirring speeds and for time intervals comparable with those of aggregation kinetics (Figure 4.15).

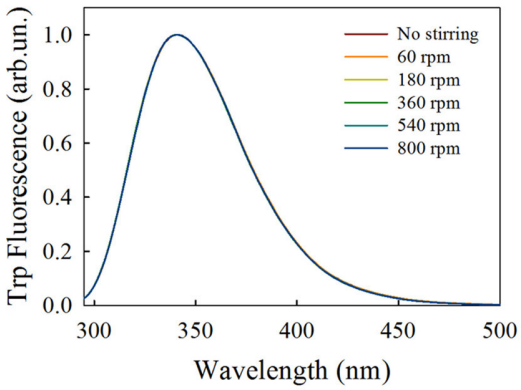

Figure 4.15 Intrinsic fluorescence spectra of identical α-La samples (0.4 mg/ml), incubated at room temperature, after 36 minutes at different stirring speeds. Spectra are normalized for the intensity maximum value.

This was also recently observed for other food proteins (*Rahaman et al., 2015, 2016*). Therefore, under the chosen experimental conditions, sample agitation does not cause an enhanced partial unfolding of the protein, as observed or supposed in studies on β-lactoglobulin (*Hill et al., 2006*), lysozyme (*Ashton et al., 2009*) or Aβ peptide (*Dunstan et al., 2009*), but only a speeding up of the aggregation process. This can be either due to a local increase in the protein concentration favoring nucleation or to the enhancing of secondary nucleation processes trough the fragmentation of already formed fibrils or the bringing back in solution of aggregates formed at the sample interfaces. Kinetics displayed in Figure 4.9 clearly show that at constant temperature and constant concentration, the fibrillation process rate does not depend on the stirring speed value.

The characterization of α-La aggregation process performed in this Chapter allows inferring that protein supramolecular assembly is a nucleated process ruled by different aggregation pathways. Nevertheless, α-La aggregates obtained at different concentrations, temperatures and stirring speeds are the same in both morphology and secondary structure. In order to deeply investigate the mechanisms underlying interaction between proteins and membranes, both protein in the native state and protein aggregates formed at pH 2 have been added to giant vesicles at neutral pH. In Figure 4.16, two-photon microscopy representative images of 200 μM POPC:POPG liposomes at pH 7.4 acquired as a function of time after addition of 10 μM native α-La are shown.

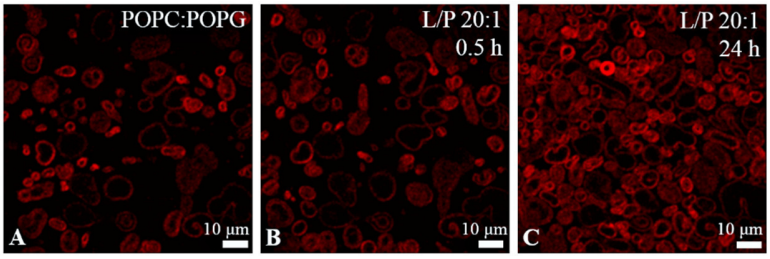

Figure 4.16. Laurdan stained POPC:POPG giant vesicles at neutral pH **(A)** before and after **(B)** 0.5 hours and **(C)** 24 hours from α-La addition at L/P 20:1. Protein concentration is 10 μM. Two-photon microscopy images have been acquired in the range 430 – 450 nm, with a 256x256 pixel resolution. Scale bar is 10 μm.

As evident from Figure 4.16A, the initial sample is made of liposomes that are highly heterogeneous in shape and size. Figure 4.16B shows that no changes in vesicle morphology occur upon protein addition in a time scale comparable with the one in Figure 3.1A – 3.1F. Liposome morphology is the same as the initial one also 24 hours after α-La addition (Figure 4.16C). The obtained result is deeply different from the one described in Chapter 3, obtained when the interaction between α-La and vesicles occurs at acidic pH. As previously observed, α-La hydrophobic regions are mainly located in protein α-helix structures (*Chrysina et al., 2000*) and these regions in the native state are buried compared to their solvent exposure typical of the molten globule state *(Lala and Kaul, 1992; Kuwajima, 1996; Wu and Kim, 1998*). This allows to conclude that structures exposing hydrophobic residues are more likely to interact with giant vesicles compared to more compact structures. This is in line with recent results, showing that α-La interaction with DOPC giant vesicles is dependent on pH, which determines both protein and membrane global charge as well as protein conformation (*Borro et al., 2017*). Therefore, it is reasonable to infer that protein insertion into the lipid bilayer, resulting in the change of vesicle morphology and in membrane disruption, is mainly driven by hydrophobic interactions. The interaction between model membranes and α-La amyloid aggregates has been also investigated.

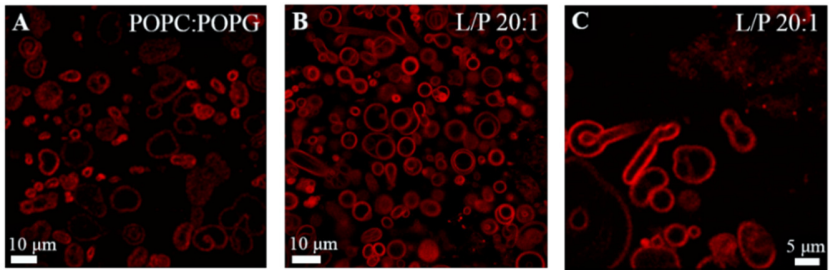

Figure 4.17 Laurdan stained POPC:POPG giant vesicles at neutral pH **(A)** before and **(B, C)** after 24 hours from the addition of α-La aggregates obtained at 33°C, at L/P 20:1. Lipid and protein concentrations are 200 μM and 10 μM, respectively. Two-photon microscopy images have been acquired in the range 430 – 450 nm. Images have a **(A, C)** 256x256 and **(B)** 1024x1024 pixel resolution. Scale bar is **(A, B)** 10 μm and **(C)** 5 μm.

Figure 4.17 shows two-photon microscopy representative images of Laurdan stained POPC:POPG giant vesicles at neutral pH before and after addition of α-La aggregates obtained

at 33°C, at pH 2. As shown in Figure 4.17B and 4.17C, upon aggregates addition both liposomes and aggregates can be distinguished, indicating that α-La aggregates interact with Laurdan dye. The interaction between α-La and Laurdan dye has been observed and described in Chapter 3. Images show that the addition of aggregates does not cause a change in vesicles morphology, highlighting the important role of hydrophobic forces in the process of interaction between α-La and vesicles.

4.2 Conclusions

In this Chapter, an experimental study on thermally- and stirring-induced amyloid formation of α-La is presented. Under the experimental conditions used, protein aggregation is ruled by different aggregation pathways that can be activated by the temperature. In particular, data reveal a highly stochastic nature of α-La supramolecular assembly, indicating that α-La fibrillation is a nucleated process taking place through a balance of primary and secondary nucleation pathways, ruled by the temperature. Depending on the concentration, protein is also found to form amorphous aggregate during the process. Although sample agitation induces or critically accelerates the formation of amyloid structures, the rate of the process and the microscopic morphology of final aggregates do not depend on the stirring speed value, keeping constant the temperature and the protein concentration. An increase of stirring speed results in the increase of the number of aggregates in solution as well as in the decrease of the sample spatial heterogeneity. At neutral pH, no changes in vesicle morphology are observed upon addition of α-La in the native or aggregate state to model membranes. This highlights the key role of hydrophobic regions in the interaction process between α-La and membranes.

Chapter 5

Protein diffusion across cell membrane: the Image Mean Square Displacement (iMSD) analysis

In this work the interaction between α-La and giant vesicles has been investigated by a multitechnique approach made of spectroscopy and microscopy techniques. In this Chapter, a new developed technique of image analysis is described, that provides the kind of motion of a protein diffusing in the cell membrane. The image Mean Square Displacement (iMSD) analysis is presented using the diffusion of Epidermal Growth Factor Receptor across cell membrane as model system and Total Internal Reflection Fluorescence (TIRF) Microscopy as tool to investigate events occurring at the cell membrane. Image correlation analysis has evolved to become a valuable method of analysis of the diffusional motion of molecules in every points of a live cell. The iMSD method, based on the concepts of Fluorescence Correlation Spectroscopy, provides proteins diffusion law, requiring a spatial averaging over a small region of the cell. In this Chapter the algorithms used for iMSD analysis are described and the visualization of the obtained data is presented under the form of spatial maps that characterize the molecular motion in each region of the cell membrane.

5.1 Results and discussion

The theory of iMSD analysis has been reported in Chapter 2. Briefly, the analysis is based on the measurement of the variance of a Gaussian describing the broadening of the spatial probability of finding a molecule in a given volume if it was at the center of the volume at time zero (*Di Rienzo et al., 2013*). The intent of the iMSD analysis is to capture the heterogeneous broadening of the correlation function in different parts of the sample and at different times. If the motion is very fast, in order to capture the displacement of the molecule, a large region around the origin must be explored. If the motion is very slow, the molecule (or particle) could not have moved or moved a very small quantity with respect to our sampling of the space around the molecule. For example, assume that a molecule has a diffusion coefficient of 100 $\mu m^2/s$: in 10^{-2} s, which is about the fastest frame time that can be acquired with a EMCCD camera, the molecule will have moved within a Gaussian distribution with a variance of about 4 μm^2. Assuming that the camera pixel (of the image projected on the real camera pixel) is about 100 nm, we will need a region of exploration of about 80 pixel-square to capture the broadening of the Gaussian to a factor of 2 in variance. At the other extreme, if the molecule has a diffusion coefficient of 0.001 $\mu m^2/s$, then the change of the variance of the Gaussian distribution after 1 s will be only a fraction of a pixel ($10^{-5}\mu m$), so that we will need to collect data for a much longer delay times to see a sizeable increase of the variance. This concept is illustrated in Figure 5.1.

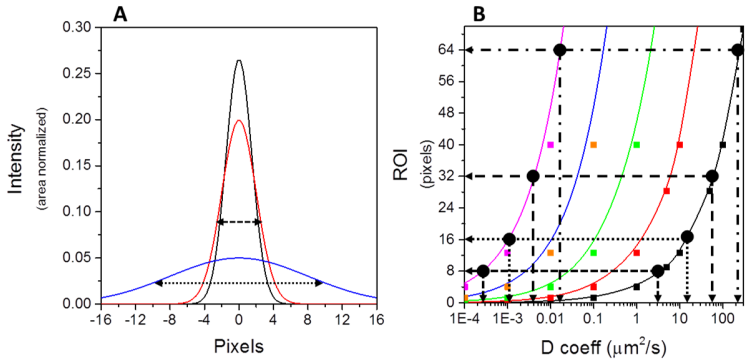

Figure 5.1 (A) Simulation of a Gaussian distribution with a width of 3 pixels (black curve). The blue curve represents the spreading as a function of time of the original Gaussian function (black curve) by diffusion of a molecule with large diffusion coefficient. The dotted double arrow line represents FWHM for a fast diffusion (around 16 pixels wide). The red curve represents the spreading of the original Gaussian function (black curve) by diffusion of a molecule with slow diffusion coefficient. The dashed double arrow line represents FWHM for a slow diffusion (around 4 pixels wide). The spreading is almost unperceivable for the slow diffusion, but the amplitude significantly decreases. **(B)** Plot for the ROI (in pixels) needed to observe a change of a factor of 2 in the FWHM as a function of diffusion coefficient, in a camera-based image (pixel size 100 nm). From top to bottom, dashed/dotted lines indicate the measurable range in the diffusion coefficient (from 400 $\mu m^2/s$ to $3x10^{-4}$ $\mu m^2/s$) for a ROI (from 64 to 8 pixels) used in the iMSD analysis. From right to left (black to purple curves) the delay is increasing from 0.01 s black single frame, 0.1s red, 1s green 10s blue, 100s purple (delay after 10000 frames).

The iMSD sprites. From the graphs of Figure 5.1, we can see that for a diffusion coefficient of 1 $\mu m^2/s$, the change of the Gaussian variance by a factor of 2 will occur in about 1 s or 100 frames (green line in Figure 5.1). Instead for a diffusion coefficient of 0.001 $\mu m^2/s$ it will require about 10000 frames for the Gaussian to broaden by about a factor of 2. For this reason it is convenient to present the STICS correlation function averaged in a log time axis. A sprite is a small image obtained calculating a series of correlation functions for a given ROI (typically 32x32 pixels or 16x16 pixels) using a log time axis with 32 time points equally spaced in a logarithmic time scale. The size of a sprite in terms of file size in bytes is, for example, 32x32x32*(sizeoffloat32)=131072 bytes. Assume that a typical image was acquired in the format 256x256 pixels and that we calculate each iMSD sprite by moving the ROI of 32x32 pixels in such a way as to superimpose each ROI by at one half of the ROI. In each direction we will have (2*256/32)-1 sprites for a total of 15x15=225 sprites. If the frame size is 512x512 we will have 961 sprites, which is typical of our measurements (Figure 5.2).

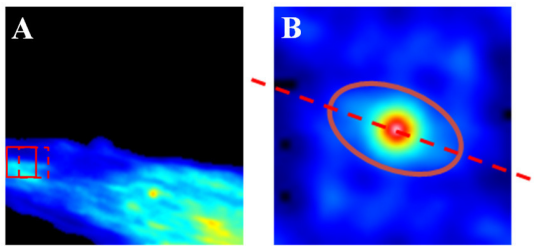

Figure 5.2 (A) Part of an image of size 256x256 is shown (pixel size is 0.139 μm). The red solid square indicates an ROI of 16x16 pixels (2.22 μm square) and the red dashed square indicate the movement by 8 pixels in the x direction, where the next sprite will be calculated. The sprites are calculated at each ROI and there is superposition between adjacent sprites. **(B)** Example of one spatial correlation function at one sprite fitted with a 2D Gaussian function tilted. The red ellipse indicates the contour at half the amplitude.

Calculation time. The issue of the calculation time for each sprite is now discussed. The computation of each sprite must be in the order of 10 ms to give a reasonable waiting time for the 200 to 1000 calculations to complete. To calculate one sprite we use an ultrafast 3D FFT routine (C. Gohlke. "Pair Correlation Function Analysis of Fluorescence Fluctuations in Big Image Time Series using Python". Big Data Image Processing & Analysis (BigDIPA) Course, 19 September 2017, University of California, Irvine). A typical calculation involves a 3D FFT of size 32x32x32768 and it takes about 20 ms (also taking into account the log averaging operation) for a total computational time of about 4-5 s for a 256x256 image stack and 16-20 s for a 512x512 image stack. This is a reasonable amount of time to wait for this calculation to be completed. The sprites are computed only once and then they are stored together with the original image stack. For a file of 256x256x32768 the total sprite file is approximately 28.8 MB starting with about 8 GB of the original image stack, which is a very substantial decrease in file size. In the SimFCS program (available at www.lfd.uci.edu), the sprite files are stored in the same directory and with the name of the original image stack but with information added to the file name to indicated the size of the ROI and if the time was calculated in a log or linear scale. A further reduction of the data size takes place by fitting each of the planes of the correlation function using a 2D Gaussian with 7 parameters: the amplitude, zero offset, 2 central positions, 2 variances along 2 lab axis and the orientation of the 2D Gaussian (Figure 5.2B). This reduces each plane of the sprite (32x32) to 7 parameters per each of the 32 time delays (Figure 5.2A). The resulting file is about 200 KB and it is stored again in the same directory and with the same

name but the end part of the name is changed. There are options in SimFCS to perform the fit of the correlation function with less parameters, but all parameters are stored in a vector of 8 values anyway.

Law of diffusion. Once the fit parameters are calculated, it is possible to use these parameters to find the "law of diffusion". For example, the inverse of the Gaussian amplitude and the 2D Gaussian variance can be used to fit 3 models for diffusion at each ROI, linear or pure diffusion, confined diffusion and a mixture of confined diffusion and long range diffusion, corresponding to the models reported in Figure 2.6 (see Chapter 2, Section 2.2). The models can be ranked according to the correlation parameter or the chi-square of the fit as it will be shown in the following section. The parameters of the fit are then stored in a fit-file together with other information about the data set and the images, for each of the parameters as it varies at every ROI. All images and maps can be saved in an Excel file for permanent storage and easy display.

Methods for data visualization. Visualization of data obtained in small regions of a cell is usually done under the form of maps, with the purpose of maintaining the spatial location of the original fluorescence image so that features of the original image can be associated with the property measured. We have used this visualization strategy for all data obtained by the iMSD technique. However, for example diffusion coefficients are tensors which require more than one value to be displayed. Other quantities can be visualized using only one value and some of the maps do not refer to a specific physical quantity, like the map of the chi-square or the map of the best model. Visualization using maps requires the color palette to be specified and the correspondence between color and value to be given. In this work, for each map we provide a histogram of all values found in the map and we use the same color scale for all images. The color scale is reported for one histogram. The visualization methods provided by our software are intended to be the first step for a more detailed analysis. For example, the map of the ${\sigma_0}^2$ above a given threshold can be associated to clusters. The map (like all the maps in the software) can be exported to be analyzed in other programs, for example in ImageJ, to obtain the number, size, shape, area and other parameters of the clusters.

iMSD laws of diffusion. For the illustration of the iMSD method we here analyze a time stack of 8192 frames, acquired with an EMCCD camera at a rate of 50 frames/sec using a TIRF microscope, of a cell expressing the EGFR receptor. The actual record is much longer but we analyze only a small fraction since the cell was slowly moving. However, the movement during

the first 80 s was less than one pixel. EGFR receptor moves slowly across the cell membrane, so that we use a small ROI of exploration (16x16 pixels, 2.22 µm square), with a total of 961 sprite. All pixels of intensity less than 1000 were disregarded for this analysis, giving 264 sprites.

Linear model for diffusion. Data were first analyzed using the linear model for diffusion (Figure 5.3). The EGFR receptor has a relatively small diffusion coefficient. Most of the values in the histogram are in the 0.01-0.1 $\mu m^2/s$ range which is typical for transmembrane receptors. In the histogram of the σ_0^2 parameter most of the occurrences are larger than the value of the intercept expected for the sole effect of the PSF. The PSF is about 0.3 µm, so that the square should be 0.09 μm^2. This finding indicates extensive clustering of the receptor.

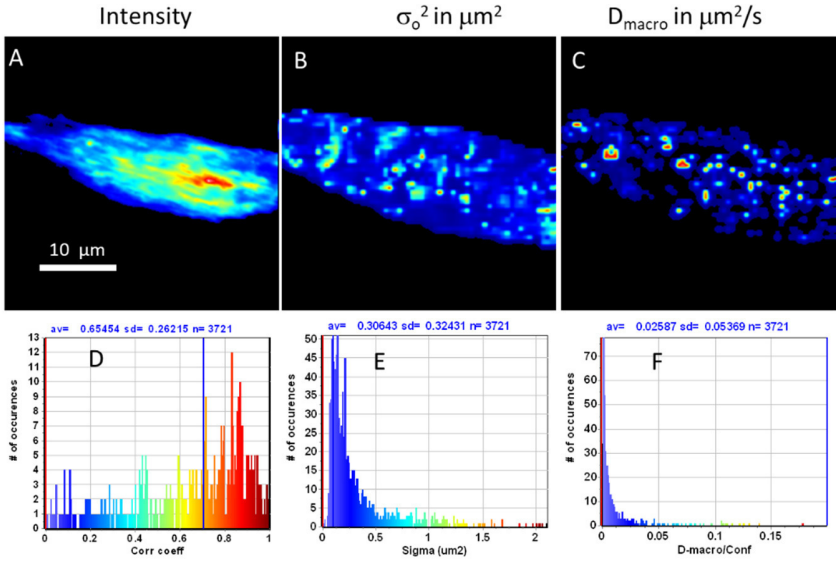

Figure 5.3 iMSD analysis for linear model of diffusion. **(A)** Intensity image. **(B)** Map of the intercept parameter σ_0^2. **(C)** Map of the D_{macro} parameter. **(D)** Histogram of the correlation coefficient. A threshold value of 0.7 is used to accept all the "reasonable" fits. **(E)** Histogram of the σ_0^2 parameter The blue vertical line indicates the value expected if the intercept is due to the PSF. **(F)** Histogram of the D_{macro} parameter. The color code in the histograms is the same color code used for the maps.

Confined model for diffusion. Figure 5.4 shows iMSD analysis performed using the confined model. The correlation coefficient histogram indicates that most of the fits are "reasonable" (Figure 5.4E). We use a threshold value of 0.7 to accept all fits above that value. The histogram of the σ_0^2 parameter indicates again extensive clustering of the receptor. The histogram of the

confinement parameter L, which is prevalent below 1 µm, is in the range expected for a transmembrane receptor. The D_{micro} parameter is also very small in the same range of the D_{macro} found using the linear model. This result could indicate that in many sprites the fit is not reflecting the real model. For this reason, a criterion to compare the different models is needed.

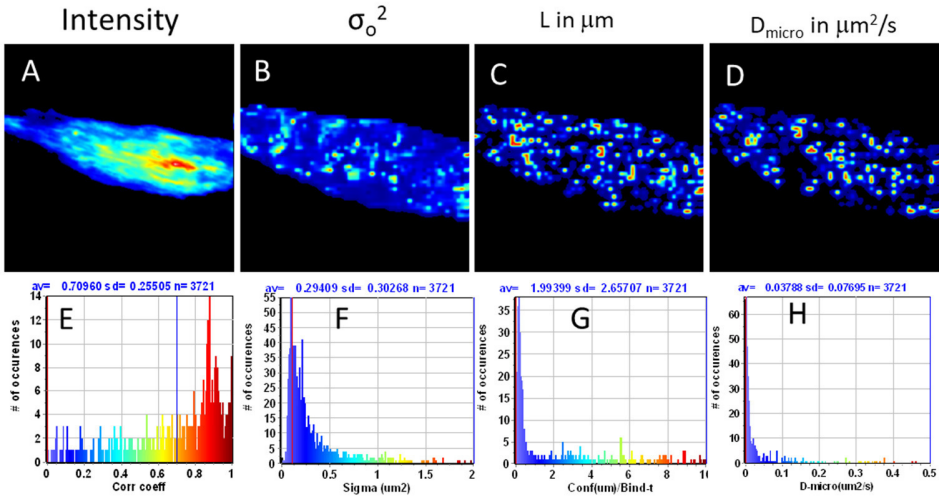

Figure 5.4 iMSD analysis for confined model of diffusion. **(A)** Intensity image. **(B)** Map of the intercept parameter σ_0^2. **(C)** Map of the confinement size L. **(D)** Map of the initial slope, also called D_{micro}. **(E)** Histogram of the correlation coefficient of the confined model fit. Only sprites with values above the blue line in the histogram are selected. **(F)** Histogram of the intercept parameter σ_0^2. The red vertical line indicates the value expected if the intercept is due to the PSF. **(G)** Histogram of the confinement length L. **(H)** Histogram of the initial slope, also called D_{micro}. The color code in the histograms is the same color code used for the maps.

The "all models" for diffusion. In the "all models", the three models for diffusion (linear, confined and partially confined model) are tested in sequence. The correlation coefficient for the fit is calculated at each sprite. Then the models are ranked according to the correlation coefficient, and the model with the highest correlation coefficient is then recorded in a table (Figure 5.5). The ranking method shows that most of the sprites are best fitted by the linear model and that forcing the fit to provide the parameters for the confined model, as was done for in the previous subsection, could lead to erroneous interpretations. For example, in the few sprites where the confined model fit the best, the D_{micro} parameter is much higher than the D_{micro} found in Figure 5.4H, as it should be expected (Figure 5.5J).

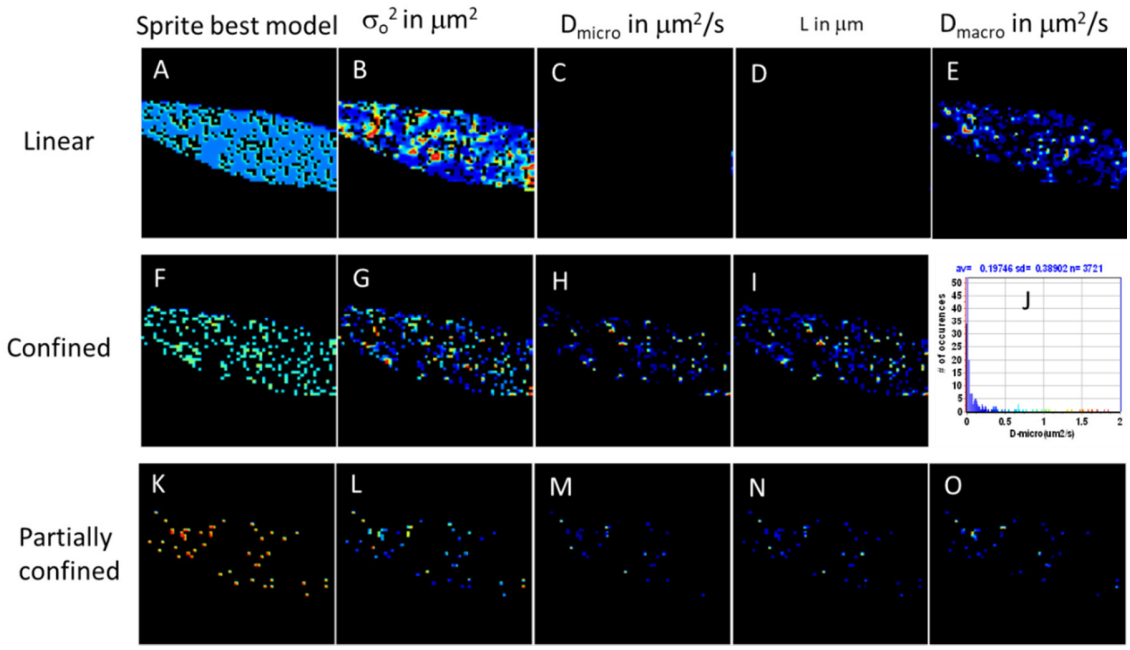

Figure 5.5 Comparison and ranking of models for diffusion at each sprite. The first column, labeled "Sprite best model", shows where in the cell one of the 3 models ranks the best. The linear model has a greater prevalence with the confined model found in fewer sprites and the partially confined model found only in some sprites, as indicated in the map. For each model, the map of the parameters is shown. The maps are complementary because if the best ranking is found in one model it cannot be found for another model in the same sprite. The models have different type and number of parameters. Panel J show the histogram of D_{micro} only for the sprites with best fit for the confined model. Comparing this panel with panel H of Figure 5.4, it is possible to observe that the histogram of D_{micro} is now different, indicating that forcing a model for the fit can give erroneous results.

Biological processes studied by image correlation analysis. We show that iMSD analysis, based on a spatial average, provides the law of diffusion of molecules in ROIs of about 2 µm side. We schematically show in Figure 5.1 that the ROI has a minimum size in order to observe the broadening of the correlation function or in the case of very slow diffusion the correlation must be calculated at very long time delays. In order to better define the law of diffusion we need to compare the fits of the correlation function using different models. This is done in our software for the law of diffusion. The ranking of the model can be shown at each sprite and the chi-square of the fits can be compared.

Computational power and size of the data set. The ideal data set should have good spatial resolution and the time stack should have at least 10,000 frames. The average file size for a single measurement is of several GB. Clearly, the computer must be able to maintain in core

memory the data needed for the computation. We have been using laptops with a minimum of 8GB of core memory and at least 4 processors to use independent threads for the computation. Since the iMSD algorithms are based on fast Fourier transforms in 1D or 3D, the speed of computation is very high but we have to use double or quadrupole precision to compute FFT's with one of the axis on the order of 32,000 elements or larger sizes. The sprite method here discussed allows very large compression of the original stack. After the first computation of the correlation function the size of the data set is reduced by more than a factor of 100 and subsequent calculations of the fit of the correlation function using few parameters can reduce the data set size another factor of 100. This enormous compression without losing information makes the calculation fast and affordable to be further analyzed for different physical models.

5.2 Conclusions

In this Chapter, a further development of Image Mean Square Displacement (iMSD) approach to image correlation spectroscopy is presented, describing the algorithms as well as the software for data visualization. The iMSD analysis provides the law of diffusion of molecules in live cells. The spatial resolution is limited by the size of the selected ROI, since the part of the ROI contributing to the overall results cannot be determined. The size of the ROI is in part dictated by the rate of diffusion. Specifically, faster diffusions need to be observed in a large ROI for a given frame rate. For slow diffusion, data need to be collected for a long time to observe a broadening of the correlation function. The algorithms used for iMSD analysis have been published and a program is also available that implements the calculation and visualization shown.

Conclusions

This work is focused on the investigation of the mechanisms at the basis of the interaction between proteins and cell membranes. The ability of proteins of interacting with membranes is at the basis of cellular function and dysfunction. The analysis of this phenomenon is intrinsically complicated as deals with multibody transitions where molecules of different nature interact and may be able to form new hybrid structures, having critically different properties with respect to separated entities. The study has been carried out using giant vesicles and α-La as model system. In *Chapter 3*, we have shown the formation of new hybrid lipid-protein structures from α-La interaction with model liposomes, investigated by means of spectroscopy and microscopy methods. Hydrophobic forces appear to be the driving forces of adsorption and insertion of the protein in the membrane, which occur in different extents depending on lipid:protein ratio in the sample. After addition of α-La molten globule to POPC:POPG giant vesicles, protein accumulates on accessible liposome surfaces and causes a quick destabilization of lipid bilayer, modifying vesicles morphology. The process ends with the formation of structures made of both lipids and protein, with a morphology that depends on the lipid:protein ratio used. A homogeneous distribution of roundish structures is observed at high protein concentration, whereas structures with more heterogeneous morphology are found at low protein concentration. The process likely consists of two main steps: an initial protein adsorption to the vesicle surface, driven by a combination of electrostatic and hydrophobic interactions, followed by the protein insertion into the lipid bilayer, occurring above a critical surface density and driven mainly by hydrophobic interactions. Laurdan GP analysis, performed with both spectroscopy and microscopy techniques, reveals a change in membrane fluidity towards a more disordered lipid phase, which can be related to membrane softening caused by the reorganization of the lipids around protein, leading to water penetration into the bilayer. We also note that control experiments revealed an interaction of α-La with Laurdan dye in the absence of lipid

membrane, resulting in a GP index increase. To our knowledge, this effect was not reported before and has to be taken in account, constituting a fundamental warning in similar experiments both when using spectroscopy and microscopy techniques. Indeed, the overall GP variations are ascribable to a redistribution of the dye on both protein and vesicles. Microscopy experiments also indicate that protein distribution is not always uniform on liposomes and that depending on protein concentration, α-La experiences different local environments as evident from FLIM measurements. Importantly, these experiments allow distinguishing between protein adsorption and insertion on/in the membrane. The insertion of α-La into the lipid bilayer results in a change of protein secondary and tertiary structure, as revealed by variations in protein far-UV spectrum and by intrinsic fluorescence measurements. Results are consistent with the idea of a protein insertion driven mainly by hydrophobic interactions.

In *Chapter 4*, α-La aggregation process has been characterized. The thermally-induced amyloid fibril formation of α-La is a complex process ruled by different pathways of aggregation. Starting from the molten globule state, the supramolecular assembly ends with the formation of amyloid structures having the same morphology independently of the used experimental conditions. Depending on α-La concentration, amorphous aggregates are also formed during protein assembly. Data reveal that the process is highly stochastic, and ruled by an interconnection of primary and secondary nucleation mechanisms. The interaction between model membranes and α-La has been investigated at neutral pH. Upon protein addition, no changes in vesicle morphology are observed when the protein is in the compact native state or in the aggregate state. This reveals a dominant role of exposed hydrophobic regions, which are able to quickly interact with liposomes and cause membrane destabilization, as observed at acidic pH when the protein has a partially disordered conformation.

In *Chapter 5*, the iMSD analysis is presented. The technique allows obtaining information on the law of diffusion of proteins across the membrane, starting directly from fluorescence images, characterizing the motion in different regions of the cell membrane. The algorithms and the software for data visualization have been presented. The iMSD analysis provides spatial maps of the protein diffusion law, characterizing the motion in the different region of the cell. The technique is limited in spatial resolution by the size of the ROI used.

The comprehension of the interaction between molten globule α-La and model membranes is essential to understand the anti-tumoral properties associated to the protein, which require its

transport into the cell nucleus across a complex membranes system (*Agasøster et al., 2003; Svensson et al., 1999, 2000*), and also to elucidate the mechanisms of achievement of its biological function (*Barbana and Pérez, 2011*).

Furthermore, in order to understand the key steps in the pathogenic mechanisms of several diseases, such as Parkinson's and Alzheimer's diseases, the investigation of the interaction between lipid bilayers and partially disordered α-La can shed light on the mechanisms ruling the interaction between cell membranes and several disordered proteins, such as α-synuclein (*Andreasen et al., 2015*) and Aβ-peptide (*Wood et al., 2003*).

Bibliography

Adachi, M., So, M., Sakurai, K., Kardos, J., and Goto, Y. (2015). *Supersaturation-limited and unlimited phase transitions compete to produce the pathway complexity in amyloid fibrillation*. J. Biol. Chem. *290*, 18134–18145.

Agasøster, A. V., Halskau, Ø., Fuglebakk, E., Frøystein, N.Å., Muga, A., Holmsen, H., and Martinez, A. (2003). *The interaction of peripheral proteins and membranes studied with α-lactalbumin and phospholipid bilayers of various compositions*. J. Biol. Chem. *278*, 21790–21797.

Amaro, M., Reina, F., Hof, M., Eggeling, C., and Sezgin, E. (2017). *Laurdan and Di-4-ANEPPDHQ probe different properties of the membrane*. J. Phys. D. Appl. Phys. *50*, 134004.

Andersen, C.B., Hicks, M.R., Vetri, V., Vandahl, B., Rahbek-Nielsen, H., Thøgersen, H., Thøgersen, I.B., Enghild, J.J., Serpell, L.C., Rischel, C., et al. (2010). *Glucagon fibril polymorphism reflects differences in protofilament backbone structure*. J. Mol. Biol. *397*, 932–946.

Andreasen, M., Lorenzen, N., and Otzen, D. (2015). *Interactions between misfolded protein oligomers and membranes: A central topic in neurodegenerative diseases?* Biochim. Biophys. Acta *1848*, 1897–1907.

Ashton, L., Dusting, J., Imomoh, E., Balabani, S., and Blanch, E.W. (2009). *Shear-induced unfolding of lysozyme monitored in situ*. Biophys. J. *96*, 4231–4236.

Axelrod, D. (1981). *Cell-substrate Contacts Illuminated by Total-Internal Reflection Fluorescence*. J. Cell Biol. *89*, 141–145.

Axelrod, D. (2001). *Total Internal Reflection Fluorescence Microscopy in Cell Biology*. Traffic *2*, 764–774.

Bäcklund, F.G., Pallbo, J., and Solin, N. (2016). *Controlling amyloid fibril formation by partial stirring*. Biopolymers *105*, 249–259.

Bagatolli, L.A., and Gratton, E. (1999). *Two-photon fluorescence microscopy observation of shape changes at the phase transition in phospholipid giant unilamellar vesicles*. Biophys. J. *77*, 2090–2101.

Bagatolli, L.A., and Gratton, E. (2000). *Two Photon Fluorescence Microscopy of Coexisting Lipid Domains in Giant Unilamellar Vesicles of Binary Phospholipid Mixtures*. Biophys. J. *78*, 290–305.

Balandrán-Quintana, R.R., Valdéz-Covarrubias, M.A., Mendoza-Wilson, A.M., and Sotelo-Mundo, R.R. (2013). *α-Lactalbumin hydrolysate spontaneously produces disk-shaped nanoparticles*. Int. Dairy J. *32*, 133–135.

Baldwin, A.J., Knowles, T.P.J., Tartaglia, G.G., Fitzpatrick, A.W., Devlin, G.L., Shammas, S.L., Waudby, C.A., Mossuto, M.F., Meehan, S., Gras, S.L., et al. (2011). *Metastability of native proteins and the phenomenon of amyloid formation*. J. Am. Chem. Soc. *133*, 14160–14163.

Bañuelos, S., and Muga, A. (1995). *Binding of Molten Globule-like Conformations to Lipid Bilayers*. J. Phys. Chem. Lett. J. Biol. Chem. *270*, 29910–29915.

Bañuelos, S., and Muga, A. (1996a). *Interaction of native and parially folded conformations of α-lactalbumin with lipid bilayers: characterisation of two membrane-bound states.* FEBS Lett. *386*, 21–25.

Bañuelos, S., and Muga, A. (1996b). *Structural requirements for the association of native and partially folded conformations of α-lactalbumin with model membranes*. Biochemistry *35*, 3892–3898.

Barbana, C., and Pérez, M.D. (2011). *Interaction of α-lactalbumin with lipids and possible implications for its emulsifying properties - A review*. Int. Dairy J. *21*, 727–741.

Barth, A. (2000). *The infrared absorption of amino acid side chains*. Prog Biophys Mol Biol *74*, 141–173.

Barth, A. (2007). *Infrared spectroscopy of proteins*. Biochim. Biophys. Acta *1767*, 1073–1101.

Battisti, A., Digman, M.A., Gratton, E., Storti, B., Beltram, F., and Bizzarri, R. (2012). *Intracellular pH measurements made simple by fluorescent protein probes and the phasor approach to fluorescence lifetime imaging*. Chem. Commun. *48*, 5127–5129.

Bekard, I.B., and Dunstan, D.E. (2009). *Shear-Induced deformation of bovine insulin in couette flow*. J. Phys. Chem. B *113*, 8453–8457.

Berliner, L.J., and Koga, K. (1987). *α-Lactalbumin Binding to Membranes: Evidence for a Partially Buried Protein*. Biochemistry *26*, 3006–3009.

Biancalana, M., and Koide, S. (2010). *Molecular mechanism of Thioflavin-T binding to amyloid fibrils*. Biochim. Biophys. Acta *1804*, 1405–1412.

Borro, B.C., Parolini, L., Cicuta, P., Foderà, V., and Di Michele, L. (2017). *Interaction with prefibrillar species and amyloid-like fibrils changes the stiffness of lipid bilayers*. Phys. Chem. Chem. Phys. *19*, 27930–27934.

Brew, K. (2003). *α-Lactalbumin*. In Advance Dairy Chemistry, Volume 1: Proteins, P.P. Fox, and P.L.H. McSweeney, eds. (Kluver Academic/Plenum Publishers), pp. 387–419.

Brewer, J., Thoke, H.S., Stock, R.P., and Bagatolli, L.A. (2017). *Enzymatic studies on planar supported membranes using a widefield fluorescence LAURDAN Generalized Polarization imaging approach*. Biochim. Biophys. Acta *1859*, 888–895.

Brinkmann, C.R., Thiel, S., Larsen, M.K., Petersen, T.E., Jensenius, J.C., and Heegaard, C.W. (2011). *Preparation and comparison of cytotoxic complexes formed between oleic acid and either bovine or human α-lactalbumin*. J. Dairy Sci. *94*, 2159–2170.

Brinkmann, C.R., Thiel, S., and Otzen, D.E. (2013). *Protein-fatty acid complexes: Biochemistry, biophysics and function*. FEBS J. *280*, 1733–1749.

Brown, C.M., Dalal, R.B., Hebert, B., Digman, M.A., Horwitz, A.R., and Gratton, E. (2008). *Raster image correlation spectroscopy (RICS) for measuring fast protein dynamics and concentrations with a commercial laser scanning confocal microscope*. J Microsc. *229*, 78–91.

Bucciantini, M., Rigacci, S., and Stefani, M. (2014). *Amyloid Aggregation: Role of Biological Membranes and the Aggregate–Membrane System*. J. Phys. Chem. Lett. *5*, 517–527.

Buell, A.K., Galvagnion, C., Gaspar, R., Sparr, E., Vendruscolo, M., Knowles, T.P.J., Linse, S., and Dobson, C.M. (2014). *Solution conditions determine the relative importance of nucleation and growth processes in α-synuclein aggregation*. Proc. Natl. Acad. Sci. *111*, 7671–7676.

Burn, P. (1988). *Amphitropic proteins: a new class of membrane proteins*. Trends Biochem. Sci. *13*, 79–83.

Buschmann, V., Weston, K.D., and Sauer, M. (2003). *Spectroscopic study and evaluation of red-absorbing fluorescent dyes*. Bioconjugate Chem. *14*, 195–204.

Butterfield, S.M., and Lashuel, H.A. (2010). *Amyloidogenic protein-membrane interactions: Mechanistic insight from model systems*. Angew. Chemie - Int. Ed. *49*, 5628–5654.

Cannon, D., and Donald, A.M. (2013). *Control of liquid crystallinity of amyloid-forming systems*. Soft Matter *9*, 2852.

Cawthern, K.M., Permyakov, E., and Berliner, L.J. (1996). *Membrane-bound states of a-lactalbumin: Implications for the protein stability and conformation*. Protein Sci. *5*, 1394–1405.

Cevc, G. (1990). *Membrane electrostatics*. Biochim. Biophys. Acta *1031*, 311–382.

Chakrabartty, A., Kortemme, T., Padmanabhan, S., and Baldwin, R.L. (1993). *Aromatic Side-Chain Contribution to Far-Ultraviolet Circular Dichroism of Helical Peptides and Its Effect on Measurement of Helix Propensities*. Biochemistry *32*, 5560–5565.

Chakraborty, S., Ittah, V., Bai, P., Luo, L., Haas, E., and Peng, Z. (2001). *Structure and Dynamics of the α-Lactalbumin Molten Globule: Fluorescence Studies Using Proteins Containing a Single Tryptophan Residue*. Biochemistry *40*, 7228–7238.

Chenal, A., Vernier, G., Savarin, P., Bushmarina, N.A., Gèze, A., Guillain, F., Gillet, D., and Forge, V. (2005). *Conformational states and thermodynamics of α-lactalbumin bound to membranes: A case study of the effects of pH, calcium, lipid membrane curvature and charge*. J. Mol. Biol. *349*, 890–905.

Chiti, F., and Dobson, C.M. (2006). *Protein Misfolding, Functional Amyloid, and Human Disease*. Annu. Rev. Biochem. *75*, 333–366.

Chiti, F., and Dobson, C.M. (2009). *Amyloid formation by globular proteins under native conditions*. Nat. Chem. Biol. *5*, 15–22.

Chiti, F., and Dobson, C.M. (2017). *Protein Misfolding, Amyloid Formation, and Human Disease: A Summary of Progress Over the Last Decade*. Annu. Rev. Biochem. *86*, 35.1-35.42.

Chrysina, E.D., Brew, K., and Acharya, K.R. (2000). *Crystal structures of Apo- and holo-bovine a-lactalbumin at 2.2-Å resolution reveal an effect of calcium on inter-lobe interactions*. J. Biol. Chem. *275*, 37021–37029.

Cohen, S.I.A., Vendruscolo, M., Dobson, C.M., and Knowles, T.P.J. (2012). *From macroscopic measurements to microscopic mechanisms of protein aggregation*. J. Mol. Biol. *421*, 160–171.

Cohen, S.I.A., Linse, S., Luheshi, L.M., Hellstrand, E., White, D.A., Rajah, L., Otzen, D.E., Vendruscolo, M., Dobson, C.M., and Knowles, T.P.J. (2013). *Proliferation of amyloid-β42 aggregates occurs through a secondary nucleation mechanism*. Proc. Natl . Acad. Sci. *110*, 9758–9763.

Dangreau, H., Joniau, M., De Cuyper, M., and Hanssens, I. (1982). *An Intramolecular Excimer Forming Probe Used To Study the Interaction of α-Lactalbumin With Model Membranes*. Biochemistry *21*, 3594–3598.

Digman, M.A., and Gratton, E. (2009). *Analysis of diffusion and binding in cells using the RICS approach*. Microsc Res Tech *72*, 323–332.

Digman, M.A., Brown, C.M., Sengupta, P., Wiseman, P.W., Horwitz, A.R., and Gratton, E. (2005a). *Measuring Fast Dynamics in Solutions and Cells with a Laser Scanning Microscope*. Biophys. J. *89*, 1317–1327.

Digman, M.A., Sengupta, P., Wiseman, P.W., Brown, C.M., Horwitz, A.R., and Gratton, E. (2005b). *Fluctuation Correlation Spectroscopy with a Laser-Scanning Microscope: Exploiting the Hidden Time Structure*. Biophys. J. *88*, L33–L36.

Digman, M.A., Caiolfa, V.R., Zamai, M., and Gratton, E. (2008). *The Phasor Approach to Fluorescence Lifetime Imaging Analysis*. Biophys. J. *94*, L14–L16.

Dobson, C.M. (2003). *Protein folding and misfolding*. Nature *426*, 884–890.

Dunstan, D.E., Hamilton-Brown, P., Asimakis, P., Ducker, W., and Bertolini, J. (2009). *Shear flow promotes amyloid-β fibrilization*. Protein Eng. Des. Sel. *22*, 741–746.

Eichner, T., and Radford, S.E. (2011). *A Diversity of Assembly Mechanisms of a Generic Amyloid Fold*. Mol. Cell *43*, 8–18.

Fändrich, M., and Dobson, C.M. (2002). *The behaviour of polyamino acids reveals an inverse side chain effect in amyloid structure formation*. EMBO J. *21*, 5682–5690.

Fändrich, M., Fletcher, M.A., and Dobson, C.M. (2001). *Amyloid fibrils from muscle myoglobin*. Nature *410*, 165–166.

Fändrich, M., Meinhardt, J., and Grigorieff, N. (2009). *Structural polymorphism of Alzheimer Aβ and other amyloid fibrils*. Prion *3*, 89–93.

Ferrone, F. (1999). *Analysis of Protein Aggregation Kinetics*. Methods Enzymol. *309*, 256–274.

Fink, A.L. (1995). *Compact Intermediate States in Protein Folding*. Annu. Rev. Biophys. Biomol. Struct. *24*, 495–522.

Fish, K.N. (2009). *Total internal reflection fluorescence (TIRF) microscopy*. Curr. Protoc. Cytom. 1–13.

Foderà, V., Librizzi, F., Groenning, M., Van De Weert, M., and Leone, M. (2008). *Secondary nucleation and accessible surface in insulin amyloid fibril formation*. J. Phys. Chem. B *112*, 3853–3858.

Foderà, V., Cataldo, S., Librizzi, F., Pignataro, B., Spiccia, P., and Leone, M. (2009). *Self-organization pathways and spatial heterogeneity in insulin amyloid fibril formation*. J. Phys. Chem. B *113*, 10830–10837.

Foderà, V., Pagliara, S., Otto, O., Keyser, U.F., and Donald, A.M. (2012). *Microfluidics reveals a flow-induced large-scale polymorphism of protein aggregates.* J. Phys. Chem. Lett. *3*, 2803–2807.

Forsyth, C., Burns, I.S., Mulheran, P.A., and Sefcik, J. (2016). *Scaling of Glycine Nucleation Kinetics with Shear Rate and Glass-Liquid Interfacial Area*. Cryst. Growth Des. *16*, 136–144.

Gast, K., Zirwer, D., Müller-Frohne, M., and Damaschun, G. (1998). *Compactness of the kinetic molten globule of bovine α-lactalbumin: A dynamic light scattering study*. Protein Sci. *7*, 2004–2011.

Gaus, K., Zech, T., and Harder, T. (2006). *Visualizing membrane microdomains by Laurdan 2-photon microscopy (review)*. Mol. Membr. Biol. *23*, 41–48.

Giehm, L., and Otzen, D.E. (2010). *Strategies to increase the reproducibility of protein fibrillization in plate reader assays.* Anal. Biochem. *400*, 270–281.

Gillam, J.E., and MacPhee, C.E. (2013). *Modelling amyloid fibril formation kinetics: mechanisms of nucleation and growth*. J. Phys. Condens. Matter *25*, 373101.

Goers, J., Permyakov, S.E., Permyakov, E. a., Uversky, V.N., and Fink, A.L. (2002). *Conformational prerequisites for α-lactalbumin fibrillation*. Biochemistry *41*, 12546–12551.

Golfetto, O., Hinde, E., and Gratton, E. (2013). *Laurdan fluorescence lifetime discriminates cholesterol content from changes in fluidity in living cell membranes*. Biophys. J. *104*, 1238–1247.

Gosal, W.S., Morten, I.J., Hewitt, E.W., Smith, D.A., Thomson, N.H., and Radford, S.E. (2005). *Competing pathways determine fibril morphology in the self-assembly of β2-microglobulin into amyloid*. J. Mol. Biol. *351*, 850–864.

Graveland-Bikker, J.F., Ipsen, R., Otte, J., and de Kruif, C.G. (2004). *Influence of calcium on the self-assembly of partially hydrolyzed a-lactalbumin*. Langmuir *20*, 6841–6846.

Graveland-Bikker, J.F., Fritz, G., Glatter, O., and De Kruif, C.G. (2006a). *Growth and structure of a-lactalbumin nanotubes*. J. Appl. Crystallogr. *39*, 180–184.

Graveland-Bikker, J.F., Schaap, I.A.T., Schmidt, C.F., and De Kruif, C.G. (2006b). *Structural and mechanical study of a self-assembling protein nanotube*. Nano Lett. *6*, 616–621.

Graveland-Bikker, J.F., Koning, R.I., Koerten, H.K., Geels, R.B.J., Heeren, R.M.A., and de Kruif, C.G. (2009). *Structural characterization of α-lactalbumin nanotubes*. Soft Matter *5*, 2020–2026.

Groenning, M., Olsen, L., van de Weert, M., Flink, J.M., Frokjaer, S., and Jørgensen, F.S. (2007). *Study on the binding of Thioflavin T to β-sheet-rich and non-β-sheet cavities*. J. Struct. Biol. *158*, 358–369.

Hall, D., Kardos, J., Edskes, H., Carver, J.A., and Goto, Y. (2015). *A Multi-Pathway Perspective on Protein Aggregation: Implications for Control of the Rate and Extent of Amyloid Formation*. FEBS Lett. *589*, 672–679.

Harris, F.M., Best, K.B., and Bell, J.D. (2002). *Use of laurdan fluorescence intensity and polarization to distinguish between changes in membrane fluidity and phospholipid order*. Biochim. Biophys. Acta *1565*, 123–128.

Hartl, F.U. (2017). *Protein misfolding diseases*. Annu. Rev. Biochem. *86*, 28.1-28.6.

Hebda, J.A., and Miranker, A.D. (2009). *The Interplay of Catalysis and Toxicity by Amyloid Intermediates on Lipid Bilayers: Insights from Type II Diabetes*. Annu. Rev. Biophys. *38*, 125–152.

Hebert, B., Costantino, S., and Wiseman, P.W. (2005). *Spatiotemporal image correlation spectroscopy (STICS) theory, verification, and application to protein velocity mapping in living CHO cells*. Biophys. J. *88*, 3601–3614.

Heegaard, N.H.H., Jørgensen, T.J.D., Rozlosnik, N., Corlin, D.B., Pedersen, J.S., Tempesta, A.G., Roepstorff, P., Bauer, R., and Nissen, M.H. (2005). *Unfolding, aggregation, and seeded amyloid formation of lysine-58-cleaved β2-microglobulin*. Biochemistry *44*, 4397–4407.

Hill, E.K., Krebs, B., Goodall, D.G., Howlett, G.J., and Dunstan, D.E. (2006). *Shear Flow Induces Amyloid Fibril Formation*. Biomacromolecules *7*, 10–13.

Hill, S.E., Miti, T., Richmond, T., and Muschol, M. (2011). *Spatial extent of charge repulsion regulates assembly pathways for lysozyme amyloid fibrils*. PLoS One *6(4),* e18171.

Hiraoka, Y., Segawa, T., Kuwajima, K., Sugai, S., and Murai, N. (1980). *α-Lactalbumin: a Calcium Metalloprotein*. Biochem. Biophys. Res. Commun. *95*, 1098–1104.

Hughes, L.D., Rawle, R.J., and Boxer, S.G. (2014). *Choose your label wisely: Water-soluble fluorophores often interact with lipid bilayers*. PLoS One *9(2),* e87649.

Hughson, F.M., Wright, P.E., and Baldwin, R.L. (1990). *Structural characterization of a partly folded apomyoglobin intermediate*. Science *249*, 1544–1548.

Hulett, J.R. (1964). *Deviations from the Arrhenius equation*. Q. Rev. Chem. Soc. *18*, 227–242.

Hurshman, A.R., White, J.T., Powers, E.T., and Kelly, J.W. (2004). *Transthyretin aggregation under partially denaturing conditions is a downhill polymerization*. Biochemistry *43*, 7365–7381.

Ipsen, R., and Otte, J. (2007). *Self-assembly of partially hydrolysed α-lactalbumin*. Biotechnol. Adv. *25*, 602–605.

Jahn, T.R., and Radford, S.E. (2005). *The Yin and Yang of protein folding*. FEBS J. *272*, 5962–5970.

Johnson, J.E., and Cornell, R.B. (1999). *Amphitropic proteins: Regulation by reversible membrane interactions*. Mol. Membr. Biol. *16*, 217–235.

Al Kayal, T., Nappini, S., Russo, E., Berti, D., Bucciantini, M., Stefani, M., and Baglioni, P. (2012). *Lysozyme interaction with negatively charged lipid bilayers: protein aggregation and membrane fusion*. Soft Matter, 8, 4524-4534

Ke, P.C., Sani, M.-A., Ding, F., Kakinen, A., Javed, I., Separovic, F., Davis, T.P., and Mezzenga, R. (2017). *Implications of peptide assemblies in amyloid diseases*. Chem. Soc. Rev. 46, 6492-6531

Kelly, S.M., and Price, N.C. (2000). *The use of circular dichroism in the investigation of protein structure and function*. Curr. Protein Pept. Sci. *1*, 349–384.

Kelly, S.M., Jess, T.J., and Price, N.C. (2005). *How to study proteins by circular dichroism*. Biochim. Biophys. Acta *1751*, 119–139.

Khurana, R., Coleman, C., Ionescu-Zanetti, C., Carter, S.A., Krishna, V., Grover, R.K., Roy, R., and Singh, S. (2005). *Mechanism of thioflavin T binding to amyloid fibrils*. J. Struct. Biol. *151*, 229–238.

Knowles, T.P.J., Vendruscolo, M., and Dobson, C.M. (2014). *The amyloid state and its association with protein misfolding diseases.* Nat. Rev. Mol. Cell Biol. *15*, 384–396.

Kodali, R., Williams, A.D., Chemuru, S., and Wetzel, R. (2010). *Aβ(1–40) forms five distinct amyloid structures whose β-sheet contents and fibril stabilities are correlated*. J. Mol. Biol. *401*, 503–517.

Köhler, C., Gogvadze, V., Håkansson, A., Svanborg, C., Orrenius, S., and Zhivotovsky, B. (2001). *A folding variant of human α-lactalbumin induces mitochondrial permeability transition in isolated mitochondria*. Eur.J.Biochem. *268*, 186–191.

Krebs, M.R.H., Bromley, E.H.C., and Donald, A.M. (2005). *The binding of thioflavin-T to amyloid fibrils: Localisation and implications*. J. Struct. Biol. *149*, 30–37.

Krittanai, C., and Johnson, W.C. (1997). *Correcting the circular dichroism spectra of peptides for contributions of absorbing side chains*. Anal. Biochem. *253*, 57–64.

Kronman, M.J., Sinha, S.K., and Brew, K. (1981). *Characteristics of the binding of calcium ion and other divalent metal ions to bovine α-lactalbumin*. J. Biol. Chem. *256*, 8582–8587.

Kuwajima, K. (1996). *The molten globule state of a-lactalbumin*. FASEB J. *10*, 102–109.

Lakowicz, J.R. (2006). *Principles of fluorescence spectroscopy* (Springer).

Lala, A.K., and Kaul, P. (1992). *Increased Exposure of Hydrophobic Surface in Molten Globule State of α-Lactalbumin*. J. Biol. Chem. *267*, 19914–19918.

Lala, A.K., Kaul, P., and Ratnam, P.B. (1995). *Membrane-protein interaction and the molten globule state: Interaction of a-lactalbumin with membranes*. J. Protein Chem. *14*, 601–609.

Lee, C.F. (2009). *Self-assembly of protein amyloids: A competition between amorphous and ordered aggregation*. Phys. Rev. E *80*, 1–5.

Lee, C.-C., Nayak, A., Sethuraman, A., Belfort, G., and McRae, G.J. (2007). *A Three-Stage Kinetic Model of Amyloid Fibrillation*. Biophys. J. *92*, 3448–3458.

LeVine III, H. (1993). *Thioflavine T interaction with synthetic Alzheimer's disease β-amyloid peptides: Detection of amyloid aggregation in solution*. Protein Sci. *2*, 404–410.

LeVine III, H. (1997). *Stopped-flow kinetics reveal multiple phases of Thioflavin T binding to Alzheimer β(1-40) amyloid fibrils*. Arch. Biochem. Biophys. *342*, 306–316.

LeVine III, H. (1999). *Quantification of β-sheet amyloid fibril structures with Thioflavin T*. Methods Enzymol. *309*, 274–284.

Librizzi, F., and Rischel, C. (2005). *The kinetic behavior of insulin fibrillation is determined by heterogeneous nucleation pathways*. Protein Sci. *14*, 3129–3134.

Librizzi, F., Foderà, V., Vetri, V., Lo Presti, C., and Leone, M. (2007). *Effects of confinement on insulin amyloid fibrils formation*. Eur. Biophys. J. *36*, 711–715.

Loksztejn, A., and Dzwolak, W. (2010). *Vortex-Induced Formation of Insulin Amyloid Superstructures Probed by Time-Lapse Atomic Force Microscopy and Circular Dichroism Spectroscopy*. J. Mol. Biol. *395*, 643–655.

Lomakin, A., Teplow, D.B., Kirschner, D.A., and Benedek, G.B. (1997). *Kinetic theory of fibrillogenesis of amyloid β-protein*. Proc. Natl. Acad. Sci. *94*, 7942–7947.

Ma, N., Digman, M.A., Malacrida, L., and Gratton, E. (2016). *Measurements of absolute concentrations of NADH in cells using the phasor FLIM method*. Biomed. Opt. Express *7*, 2441.

Van Maarschalkerweerd, A., Vetri, V., Langkilde, A.E., Foderà, V., and Vestergaard, B. (2014). *Protein/Lipid Coaggregates Are Formed during α-Synuclein-induced disruption of libid bilayers.* Biomacromolecules *15*, 3643–3654.

Van Maarschalkerweerd, A., Vetri, V., and Vestergaard, B. (2015). *Cholesterol facilitates interactions between α-synuclein oligomers and charge-neutral membranes*. FEBS Lett. *589*, 2661–2667.

Maskevich, A.A., Stsiapura, V.I., Kuzmitsky, V.A., Kuznetsova, I.M., Povarova, O.I., Uversky, V.N., and Turoverov, K.K. (2007). *Spectral properties of thioflavin T in solvents with different dielectric properties and in a fibril-incorporated form*. J. Proteome Res. *6*, 1392–1401.

Merlini, G., Seldin, D.C., and Gertz, M.A. (2011). *Amyloidosis: Pathogenesis and new therapeutic options*. J. Clin. Oncol. *29*, 1924–1933.

Michalet, X. (2010). *Mean square displacement analysis of single-particle trajectories with localization error: Brownian motion in an isotropic medium*. Phys. Rev. E *82*, 1–13.

Milanesi, L., Sheynis, T., Xue, W.-F., Orlova, E. V., Hellewell, A.L., Jelinek, R., Hewitt, E.W., Radford, S.E., and Saibil, H.R. (2012). *Direct three-dimensional visualization of membrane disruption by amyloid fibrils*. Proc. Natl. Acad. Sci. *109*, 20455–20460.

Militello, V., Casarino, C., Emanuele, A., Giostra, A., Pullara, F., and Leone, M. (2004). *Aggregation kinetics of bovine serum albumin studied by FTIR spectroscopy and light scattering*. Biophys. Chem. *107*, 175–187.

Morozova, L., Haezebrouck, P., and Van Cauwelaert, F. (1991). *Stability of equine lysozyme. I. Thermal unfolding behaviour*. Biophys. Chem. *41*, 185–191.

Munishkina, L.A., and Fink, A.L. (2007). *Fluorescence as a method to reveal structures and membrane-interactions of amyloidogenic proteins*. Biochim. Biophys. Acta *1768*, 1862–1885.

Naiki, H., Higuchi, K., Hosokawa, M., and Takeda, T. (1989). *Fluorometric determination of amyloid fibrils in vitro using the fluorescent dye, thioflavin T*. Anal. Biochem. *177*, 244–249.

Nielsen, L., Khurana, R., Coats, A., Frokjaer, S., Brange, J., Vyas, S., Uversky, V.N., and Fink, A.L. (2001). *Effect of Environmental Factors on the Kinetics of Insulin Fibril Formation*. Biochemistry *40*, 6036–6046.

Otte, J., Ipsen, R., Bauer, R., Bjerrum, M.J., and Waninge, R. (2005). *Formation of amyloid-like fibrils upon limited proteolysis of bovine a-lactalbumin*. Int. Dairy J. *15*, 219–229.

Ow, S.-Y., and Dunstan, D.E. (2013). *The effect of concentration, temperature and stirring on hen egg white lysozyme amyloid formation*. Soft Matter *9*, 9692–9701.

Owen, D.M., Magenau, A., Majumdar, A., and Gaus, K. (2010). *Imaging membrane lipid order in whole, living vertebrate organisms*. Biophys. J. *99*, L7–L9.

Owen, D.M., Rentero, C., Magenau, A., Abu-Siniyeh, A., and Gaus, K. (2012). *Quantitative imaging of membrane lipid order in cells and organisms*. Nat. Protoc. *7*, 24–35.

Pallitto, M.M., and Murphy, R.M. (2001). *A Mathematical Model of the Kinetics of β-Amyloid Fibril Growth from the Denatured State*. Biophys. J. *81*, 1805–1822.

Parasassi, T., De Stasio, G., D'Ubaldo, A., and Gratton, E. (1990). *Phase fluctuation in phospholipid membranes reaveled by Laurdan fluorecence*. Biophys. J *57*, 1179–1186.

Parasassi, T., Gratton, E., Yu, W.M., Wilson, P., and Levi, M. (1997). *Two-photon fluorescence microscopy of laurdan generalized polarization domains in model and natural membranes*. Biophys. J. *72*, 2413–2429.

Parasassi, T., Krasnowska, E.K., Bagatolli, L., and Gratton, E. (1998). *Laurdan and Prodan as polarity-sensitive fluorescent membrane probes*. J. Fluoresc. *8*, 365–373.

Pedersen, J.S., Dikov, D., Flink, J.L., Hjuler, H.A., Christiansen, G., and Otzen, D.E. (2006). *The changing face of glucagon fibrillation: Structural polymorphism and conformational imprinting*. J. Mol. Biol. *355*, 501–523.

Pelton, J.T., and McLean, L.R. (2000). *Spectroscopic Methods for Analysis of Protein Secondary Structure*. Anal. Biochem. *277*, 167–176.

Permyakov, E.A., and Berliner, L.J. (2000). *α -Lactalbumin : structure and function*. FEBS Lett. *473*, 269–274.

Permyakov, E.A., Morozova, L.A., and Burstein, E.A. (1985). *Cation binding effects on the pH, thermal and urea denaturation transitions in α-lactalbumin*. Biophys. Chem. *21*, 21–31.

Petkova, A.T., Leapman, R.D., Guo, Z., Yau, W., Mattson, M.P., and Tiycko, R. (2005). *Self-Propagating , Molecular-Level Polymorphism in Alzheimer's β-Amyloid Fibrils*. Science. *307*, 262–266.

Pfeil, W., Bychkova, V.E., and Ptitsyn, O.B. (1986). *Physical nature of the phase transition in globular proteins. Calorimetric study of human α-lactalbumin*. FEBS Lett. *198*, 287–291.

Piccirilli, F., Schirò, G., Vetri, V., Lupi, S., Perucchi, A., and Militello, V. (2015). *Decoding vibrational states of Concanavalin A amyloid fibrils*. Biophys. Chem. *199*, 17–24.

Pike, A.C., Brew, K., and Acharya, K.R. (1996). *Crystal structures of guinea-pig, goat and bovine α-lactalbumin highlight the enhanced conformational flexibility of regions that are significant for its action in lactose synthase.* Structure *4*, 691–703.

Plotegher, N., Stringari, C., Jahid, S., Veronesi, M., Girotto, S., Gratton, E., and Bubacco, L. (2015). *NADH fluorescence lifetime is an endogenous reporter of α-synuclein aggregation in live cells*. FASEB J. *29*.

Polverino de Laureto, P., Vinante, D., Scaramella, E., Frare, E., and Fontana, A. (2001). *Stepwise proteolytic removal of the β subdomain in α-lactalbumin: The protein remains folded and can form the molten globule in acid solution*. Eur. J. Biochem. *268*, 4324–4333.

Polverino de Laureto, P., Frare, E., Gottardo, R., and Fontana, A. (2002). *Molten globule of bovine α-lactalbumin at neutral pH induced by heat, trifluoroethanol, and oleic acid: A comparative analysis by circular dichroism spectroscopy and limited proteolysis*. Proteins Struct. Funct. Genet. *49*, 385–397.

Rahaman, T., Vasiljevic, T., and Ramchandran, L. (2015). *Conformational changes of β-lactoglobulin induced by shear, heat , and pH — Effects on antigenicity*. J. Dairy Sci. *98*, 4255–4265.

Rahaman, T., Vasiljevic, T., and Ramchandran, L. (2016). *Shear, heat and pH induced conformational changes of wheat gluten - Impact on antigenicity*. Food Chem. *196*, 180–188.

Ramboarina, S., and Redfield, C. (2003). *Structural Characterisation of the Human α-Lactalbumin Molten Globule at High Temperature*. J. Mol. Biol. *330*, 1177–1188.

Di Rienzo, C., Gratton, E., Beltram, F., and Cardarelli, F. (2013). *Fast spatiotemporal correlation spectroscopy to determine protein lateral diffusion laws in live cell membranes*. Proc. Natl. Acad. Sci. *110*, 12307–12312.

Di Rienzo, C., Cardarelli, F., Di Luca, M., Beltram, F., and Gratton, E. (2016). *Diffusion Tensor Analysis by Two-Dimensional Pair Correlation of Fluorescence Fluctuations in Cells*. Biophys. J. *111*, 841–851.

Rødland, I., Halskau, Ø., Martínez, A., and Holmsen, H. (2005). *α-Lactalbumin binding and membrane integrity - effect of charge and degree of unsaturation of glycerophospholipids*. Biochim. Biophys. Acta *1717*, 11–20.

Ross, C.A., and Poirier, M.A. (2005). *What is the role of protein aggregation in neurodegeneration?* Nat. Rev. Mol. Cell Biol. *6*, 891–898.

Ruggeri, F., Zhang, F., Lind, T., Bruce, E.D., Lau, B.L.T., and Cárdenas, M. (2013). *Non-specific interactions between soluble proteins and lipids induce irreversible changes in the properties of lipid bilayers*. Soft Matter *9*, 4219–4226.

Sameni, S., Syed, A., Marsh, J.L., and Digman, M.A. (2016). *The phasor-FLIM fingerprints reveal shifts from OXPHOS to enhanced glycolysis in Huntington Disease*. Sci. Rep. *6*, 34755.

Sanchez, S.A., Tricerri, M.A., Gunther, G., and Gratton, E. (2007). *Laurdan Generalized Polarization: from cuvette to microscope*. Mod. Res. Educ. Top. Microsc. *2*, 1007–1014.

Sanchez, S.A., Tricerri, M.A., Ossato, G., and Gratton, E. (2010). *Lipid packing determines protein-membrane interactions: challenges for apolipoprotein A-I and High Density Lipoproteins*. Biochim. Biophys. Acta *1798*, 1399–1408.

Sanchez, S.A., Tricerri, M.A., and Gratton, E. (2012). *Laurdan generalized polarization fluctuations measures membrane packing micro-heterogeneity in vivo*. Proc. Natl . Acad. Sci. *109*, 7314–7319.

Schneider, F., Ruhlandt, D., Gregor, I., Enderlein, J., and Chizhik, A.I. (2017). *Quantum Yield Measurements of Fluorophores in Lipid Bilayers Using a Plasmonic Nanocavity*. J. Phys. Chem. Lett. *8*, 1472–1475.

Serio, T.R., Cashikar, A.G., Kowal, A.S., Sawicki, G.J., Moslehi, J.J., Serpell, L., Arnsdorf, M.F., and Lindquist, S.L. (2000). *Nucleated Conformational Conversion and the Replication of Conformational Information by a Prion Determinant*. Science *289*, 1317–1321.

Smith, M.I., Foderà, V., Sharp, J.S., Roberts, C.J., and Donald, A.M. (2012). *Factors affecting the formation of insulin amyloid spherulites*. Colloids Surfaces B Biointerfaces *89*, 216–222.

Souillac, P.O., Uversky, V.N., and Fink, A.L. (2003). *Structural transformations of oligomeric intermediates in the fibrillation of the immunoglobulin light chain LEN*. Biochemistry *42*, 8094–8104.

Stefani, M. (2004). *Protein misfolding and aggregation: New examples in medicine and biology of the dark side of the protein world*. Biochim. Biophys. Acta *1739*, 5–25.

Stefani, M. (2010). *Biochemical and biophysical features of both oligomer/fibril and cell membrane in amyloid cytotoxicity*. FEBS J. *277*, 4602–4613.

Stranks, S.D., Ecroyd, H., Van Sluyter, S., Waters, E.J., Carver, J.A., and Von Smekal, L. (2009). *Model for amorphous aggregation processes*. Phys. Rev. E *80*.

Straub, J.E., and Thirumalai, D. (2014). *Membrane-protein interactions are key to understanding amyloid formation*. J. Phys. Chem. Lett. *5*, 633–635.

Stringari, C., Cinquin, A., Cinquin, O., Digman, M.A., Donovan, P.J., and Gratton, E. (2011). *Phasor approach to fluorescence lifetime microscopy distinguishes different metabolic states of germ cells in a live tissue*. Proc. Natl . Acad. Sci. *108*, 13582–13587.

Stringari, C., Nourse, J.L., Flanagan, L.A., and Gratton, E. (2012). *Phasor Fluorescence Lifetime Microscopy of Free and Protein-Bound NADH Reveals Neural Stem Cell Differentiation Potential.* PLoS One *7 (11),* e48014.

Stsiapura, V.I., Maskevich, A.A., Kuzmitsky, V.A., Uversky, V.N., Kuznetsova, I.M., and Turoverov, K.K. (2008). *Thioflavin T as a molecular rotor: Fluorescent properties of thioflavin T in solvents with different viscosity*. J. Phys. Chem. B *112*, 15893–15902.

Svensson, M., Sabharwal, H., Håkansson, A., Mossberg, A.K., Lipniunas, P., Leffler, H., Svanborg, C., and Linse, S. (1999). *Molecular characterization of a-lactalbumin folding variants that induce apoptosis in tumor cells*. J. Biol. Chem. *274*, 6388–6396.

Svensson, M., Håkansson, A., Mossberg, A.-K., Linse, S., and Svanborg, C. (2000). *Conversion of α-lactalbumin to a protein inducing apoptosis*. Proc. Natl . Acad. Sci. *97*, 4221–4226.

Svensson, M., Fast, J., Mossberg, A.-K., Düringer, C., Gustafsson, L., Hallgren, O., Brooks, C.L., Berliner, L., Linse, S., and Svanborg, C. (2003). *Alpha-lactalbumin unfolding is not sufficient to cause apoptosis, but is required for the conversion to HAMLET (human alpha-lactalbumin made lethal to tumor cells)*. Protein Sci. *12*, 2794–2804.

Taniguchi, Y., Ohba, T., Miyata, H., and Ohki, K. (2006). *Rapid phase change of lipid microdomains in giant vesicles induced by conversion of sphingomyelin to ceramide.* Biochim. Biophys. Acta *1758*, 145–153.

Teoh, C.L., Bekard, I.B., Asimakis, P., Griffin, M.D.W., Ryan, T.M., Dunstan, D.E., and Howlett, G.J. (2011). *Shear Flow Induced Changes in Apolipoprotein C-II Conformation and Amyloid Fibril Formation*. Biochemistry *50*, 4046–4057.

Tycko, R. (2015). *Amyloid Polymorphism: Structural Basis and Neurobiological Relevance*. Neuron *86*, 632–645.

Uversky, V.N., and Fink, A.L. (2004). *Conformational constraints for amyloid fibrillation: The importance of being unfolded*. Biochim. Biophys. Acta *1698*, 131–153.

Vetri, V., Librizzi, F., Militello, V., and Leone, M. (2007a). *Effects of succinylation on thermal induced amyloid formation in Concanavalin A*. Eur. Biophys. J. *36*, 733–741.

Vetri, V., Canale, C., Relini, A., Librizzi, F., Militello, V., Gliozzi, A., and Leone, M. (2007b). *Amyloid fibrils formation and amorphous aggregation in concanavalin A*. Biophys. Chem. *125*, 184–190.

Vetri, V., Ossato, G., Militello, V., Digman, M.A., Leone, M., and Gratton, E. (2011). *Fluctuation methods to study protein aggregation in live cells: Concanavalin A oligomers formation*. Biophys. J. *100*, 774–783.

Vetri, V., Leone, M., Morozova-Roche, L.A., Vestergaard, B., and Foderà, V. (2013). *Unlocked Concanavalin A Forms Amyloid-like Fibrils from Coagulation of Long-lived "Crinkled" Intermediates*. PLoS One *8*, e68912.

Voropai, E.S., Samtsov, M.P., Kaplevskii, K.N., Maskevich, A.A., Stepuro, V.I., Povarova, O.I., Kuznetsova, I.M., Turoverov, K.K., Fink, A.L., and Uverskii, V.N. (2003). *Spectral Properties of Thioflavin T and Its Complexes With Amyloid Fibrils*. J. Appl. Spectrosc. *70*, 868–874.

Wang, W., and Roberts, C.J. (2013). *Non-Arrhenius Protein Aggregation*. AAPS J. *15*, 840–851.

Weber, G., and Farris, F.J. (1979). *Synthesis and Spectral Properties of a Hydrophobic Fluorescent Probe: 6-Propionyl-2-(dimethylamino)naphthalene*. Biochemistry *18*, 3075–3078.

Wei, G., Su, Z., Reynolds, N.P., Arosio, P., Hamley, I.W., Gazit, E., and Mezzenga, R. (2017). *Self-assembling peptide and protein amyloids: from structure to tailored function in nanotechnology*. Chem. Soc. Rev. *46*, 4661–4708.

Wen, H., Glomm, W.R., Halskau, Ø., (2013). *Cytotoxicity of bovine a-lactalbumin: Oleic acid complexes correlates with the disruption of lipid membranes*. Biochim. Biophys. Acta *1828*, 2691–2699.

Wood, W.G., Eckert, G.P., Igbavboa, U., and Müller, W.E. (2003). *Amyloid beta-protein interactions with membranes and cholesterol: Causes or casualties of Alzheimer's disease*. Biochim. Biophys. Acta *1610*, 281–290.

Wu, L.C., and Kim, P.S. (1998). *A specific hydrophobic core in the α-lactalbumin molten globule*. J. Mol. Biol. *280*, 175–182.

Xue, W.-F., Homans S.W., Radford S.E. (2008). *Systematic analysis of nucleation-dependent polymerization revewls new insight into the mechanism of amyloid self-assembly*. Proc. Natl. Acad. Sci. U. S. A. *105,* 8926–8931.

Yan, Y.-B., Zhang, J., He, H.-W., and Zhou, H.-M. (2006). *Oligomerization and aggregation of bovine pancreatic ribonuclease A: characteristic events observed by FTIR spectroscopy*. Biophys. J. *90*, 2525–2533.

Yoshimura, Y., Lin, Y., Yagi, H., Lee, Y.-H., Kitayama, H., Sakurai, K., So, M., Ogi, H., Naiki, H., and Goto, Y. (2012). *Distinguishing crystal-like amyloid fibrils and glass-like amorphous aggregates from their kinetics of formation*. Proc. Natl. Acad. Sci. U. S. A. *109*, 14446–14451.

Zhu, M., Li, J., and Fink, A.L. (2003). *The association of a-synuclein with membranes affects bilayer structure, stability, and fibril formation*. J. Biol. Chem. *278*, 40186–40197.

Acknowledgements

I sincerely thank my supervisor Prof. Maurizio Leone for the opportunity he gave me to experience scientific research and for his supervision and guidance throughout my research activity. I want to express my gratitude to my co-tutor Prof. Valeria Vetri for the continuous support and encouragement she provided me during these three pleasant and sometimes challenging years, allowing me gradually to develop autonomy in the scientific research. I wish to extend my special thanks to Prof. Valeria Militello.

I would like to express my sincere gratitude to Prof. Enrico Gratton for the unique opportunity he gave me to spend seven months of my PhD in his lab, for making me feel so welcome and part of the LFD during my stay in Irvine, and for all the interesting discussions. I want also to thank Prof. Michelle Digman for the precious help and scientific suggestions. Thank you also to all the people I have had the pleasure to work with within the LFD at UCI, for providing such a stimulating and interdisciplinary environment.

I wish also to thank Prof. Vito Foderà from the Department of Pharmacy, University of Copenhagen, for following my research activity and for the useful scientific discussions.

I thank Marcello Mirabello for his technical assistance.

I want also to thank all the people with whom I had the pleasure of sharing the long days in the lab here in Palermo, which have contributed to the achievement of this important goal.

Last but not the least, I wish to thank my family and friends for continuously supporting me during these years.